DNA AND CELL BIOLOGY
Volume 32, Number 8, 2013

Pp. 467–479
DOI: 10.1089/dna.2012.1950

Nucleofection of Expression Vectors Induces a Robust Interferon Response and Inhibition of Cell Proliferation

Sandra Huerfano, Boris Ryabchenko, and Jitka Forstová

The interferon (IFN) response, induced as a side effect after transfection of nucleic acids into mammalian cells, is known but inadequately described. We followed the IFN response, the fate of cells, and the possible mechanisms leading to this response in NIH3T3 mouse fibroblasts after DNA nucleofection. The gateway destination vector, phGf, and its derivatives encoding toxic and non-toxic variants of the minor structural proteins of polyomaviruses, VP2 and VP3, were used. DNA vector sequences induced in cells the production of high levels of IFN and the upregulation of the IFN-inducible genes, *Mx-1*, *STAT1*, *IRF1*, and *IRF7*. The IFN response was not restricted to phGf-derived plasmids. In nucleofected cells, upregulation of the modified γ-histone 2A.X indicating DNA damage and inhibition of cell proliferation were also observed. Although 3T3 cells expressed the Toll-like receptor-9 (TLR9) and vectors used for nucleofection contained unmethylated CpGs, signaling leading to IFN induction was found to be TLR9 independent. However, the early activation of nuclear factor-kappa B suggested the participation of this transcription factor in IFN induction. Surprisingly, in contrast to nucleofection, transfection using a cationic polymer induced only a poor IFN response. Together, the results point to a strong side effect of nucleofection.

Introduction

Transfection of mammalian cells with bacterial, viral, or synthetic nucleic acids has been acknowledged to induce type I interferon (IFN) responses. However, there has been little attention paid to these responses appearing as a side effect of cell transfection during studies of cellular responses. IFN induces tremendous effects on many cellular processes by activating different signaling cascades, such as Janus kinases-signal transducer and activator of transcription (JAK/STAT), mitogen-activated protein kinase (MAPK), or phosphatidylinositol 3-kinases/serine/threonine kinase Akt (PI3K/Akt) (reviewed in Pestka *et al.*, 2004; Platanias, 2005; Stetson and Medzhitov, 2006). These pathways are involved, among other vital cellular processes, in the regulation of cell growth, proliferation, and apoptosis. In addition, IFN dramatically affects protein synthesis through activation of the protein kinase R (PKR). Activation of PKR results in the formation of an inactive complex of GDP-eIF2 (Guanosine diphosphate-eukaryotic initiation factor 2) that blocks translation (reviewed in García *et al.*, 2006; Pitha and Kunzi, 2007; Pindel and Sadler, 2011).

For a long time, the only known mechanism used for immune cells to recognize nucleic acids was the sensing of unmethylated CpG motifs (cytosine next to guanine) by the endosomal membrane receptor, Toll-like receptor-9 (TLR9) (Krieg *et al.*, 1995; Hemmi *et al.*, 2000; Dalpke *et al.*, 2006). Sensing of DNA by this receptor induces the production of type I IFN and other cytokines. Interestingly, it was also reported that non-immune cells are able to produce type I IFN in response to bacterial DNA and CpG motifs in a TLR9-dependent manner (Li *et al.*, 2004; Platz *et al.*, 2004; Di *et al.*, 2009). Also, overexpression of TLR9 in non-immune cells reconstitutes CpG DNA responses (Bauer *et al.*, 2001; Takeshita *et al.*, 2001; Assaf *et al.*, 2009). Recently, however, several cytoplasmic sensors that can recognize DNA by different mechanisms (CpG motif/TLR9 independent) have been reported for immune and non-immune cells: DNA-dependent activator of IFN-regulatory factor (DAI) (Takaoka *et al.*, 2007), DEAH box polypeptide 9 (DHX9), DEAH box polypeptide 36 (DHX36) (Kim *et al.*, 2010), DDX41 (Helicase) (Zhang *et al.*, 2011b), absence in melanoma 2 (AIM2) (Hornung *et al.*, 2009), IFN inducible protein 16 (IFI16) (Unterholzner *et al.*, 2010), leucine-rich repeat containing protein (LRRF1P1l protein) (Yang *et al.*, 2010), and the Ku70 protein (Zhang *et al.*, 2011a). It is speculated that these sensors may recognize DNA in a sequence-independent manner. Nevertheless, the nature of the interaction between DNA and the cytoplasmic sensors is still unknown. With the exception of the AIM2 receptor, which induces caspase-1-dependent maturation of the pro-inflammatory cytokines, interleukin (IL)-1β and IL-18 (Hornung *et al.*, 2009), the sensing of DNA

by cytoplasmic sensors induces type I IFN production. The pathways of induction of the IFN response have been uncovered. In broad terms, six important signal molecules downstream of the receptors have been described as modulators of the response: the transcription factors, nuclear factor-kappa B (NF-κB) and IFN regulatory factor (IRF) 1, 3, 7, further, the protein kinase TANK-binding kinase 1 (TBK1), and the transmembrane ER resident protein, stimulator of IFN genes (STING) (Ishikawa *et al.*, 2009 and reviewed in Keating *et al.*, 2011; Sharma and Fitzgerald, 2011). Some of these proteins participate redundantly in different sensor signaling pathways of IFN induction.

The strength, and therefore, the outcome of the IFN response may depend on DNA properties (e.g., CpG content and methylation state), DNA delivery mechanism and cell type, as has been described in the context of immune system cells or even for other cells. In detail, murine dendritic cells produced inflammatory cytokines when stimulated with DNA containing CpG motifs from *Escherichia coli* or with naked plasmid DNA, but not when stimulated with calf thymus DNA (poor in CpG motifs). In addition, it was also found that the amount of secreted cytokines increased when the DNA was complexed with the cationic lipid-lipofectin (Yoshinaga *et al.*, 2006). It was also demonstrated that peritoneal macrophages from mice launched strong immunoresponses to DNA/cationic liposome complexes in a CpG-dependent and independent manner (Yasuda *et al.*, 2005). In a study using non-immune cells, it has been shown that among the transfection methods such as electroporation, lipofection by Fugene, or transfection by the cation polymer ExGen, the last one induced the highest levels of IFNβ. In addition, the authors of this study found that the IFN response was induced in a cell type-dependent manner (Rautsi *et al.*, 2007). From the above studies, we can conclude that there may be specific ways of how the DNA is sensed, and an important part of this process may be dependent on the DNA entry into the cells and its transport toward the nucleus. For example, DNA transfected by lipofection or by cations engages the cellular endocytic pathways to reach the nucleus (Legendre and Szoka, 1992; Yasuda *et al.*, 2005), while electroporation induces transient pores in the plasma membrane for DNA entry into the cells (Vasilkoski *et al.*, 2006). Another recently developed method, nucleofection, combines electrical parameters with cell type-adapted solutions of unknown composition for delivery of DNA "straight into the cell nucleus" (Gresch *et al.*, 2004). The influence of this particular method of transfection on IFN responses is currently unknown.

This study was preceded by a microarray analysis of mouse fibroblast cells transfected by nucleofection with mammalian expression vectors for transient expression of highly cytotoxic VP2 or VP3 structural proteins of the Mouse polyomavirus (MPyV). The study disclosed remarkable concomitant IFN and DNA damage response (DDR) and upregulation of the endosomal membrane receptor, TLR9, in cells transfected with a control empty plasmid. Here, we analyzed those responses, evaluated the role of TLR9 ligands (unmethylated CpG motifs) in the establishment of the IFN response and investigated the role of IRF3, and NF-κB transcription factors in the signaling for the IFN induction. As a model, we used the phGf gateway destination vector from Addgene and three of its derivatives carrying genes for *VP2* or *VP3* of MPyV and non-cytotoxic VP2 of the Merkel cell polyomavirus (MCPyV). For comparison, we used other vectors, pEGFP-N1 (Clontech) and two of its derivatives carrying the MPyV *VP2* or *VP3* genes and pcDNA3.1 (Invitrogen).

Materials and Methods

Cell lines, DNA, and transfections

Mouse fibroblasts NIH3T3 and mouse embryonic fibroblasts (MEF) were grown at 37°C in a humidified incubator with a 5% CO_2 atmosphere, using DMEM (Dulbecco's modified Eagle's medium; Sigma-Aldrich) supplemented with 10% fetal bovine serum and 4 mM L-glutamine. Plasmid DNA was prepared using the EndoFree Maxi Kit (Qiagen), diluted in TE and stored at −20°C. Plasmid concentration and purity was determined by nanodrop. Transfections were performed by electroporation within a nucleofector™ device (program U-30 for 3T3 or A-23 for MEF), using Amaxa reagents (Amaxa Biosystems) or by cationic polymer by using TurboFect™ (Thermo Scientific) according to the manufacturer's instructions. Briefly, cells were seeded 24 h prior to nucleofection and 4×10^6 cells were transfected with 6 μg of plasmid DNA (~1.0–1.5×10^{12} DNA molecules), except in the case of transfection with the small plasmid, phGfΔGΔR, when only 4 μg of DNA were used (1.2×10^{12} DNA molecules). For turbofection, 1×10^6 cells were seeded in 60-mm plates 24 h prior to transfection and then were transfected by 6 μg of DNA.

DNA constructs

The plasmids phGf, a Gateway® plasmid (# 22516), and their derivates ph2p (# 22521) and ph3p (# 22520) coding for variants of the MPyV minor proteins VP2 and VP3 were obtained from Addgene (Buck *et al.*, 2006; Tolstov *et al.*, 2009). We did modify the plasmids by deletion of the ORF coding for the EGF protein. Briefly, plasmids were double digested with *Stu*I and *Cla*I, the overhangs were filled in by the Klenow fragment of DNA polymerase I and the plasmid DNA was circularized by ligation. The modified products were named phGfΔG, ph2pΔG, and ph3pΔG, respectively. In addition, for a control, we further modified the phGfΔG plasmid by deletion of region 2 (between lambda attachment sites [*att* sites]; Fig. 1A), which becomes substituted during gateway cloning. The resulting plasmid was named phGfΔGΔR. In detail, the phGfΔG plasmid was double digested with Nhe I and Nar I, the overhangs were filled in by the Klenow fragment of DNA polymerase I and the plasmid DNA was circularized by ligation. The phGf derivative plasmid ph2m (# 22518) carrying gene for the VP2 structural protein of the MCPyV was also obtained from Addgene (Tolstov *et al.*, 2009). The vector pEGFP-N1 was obtained from Clontech. Its derivates, VP2-EGFP-N1 (carrying MPyV *VP2* gene) or VP3-EGFP-N1 (carrying MPyV *VP3* gene), had been previously prepared in our lab (Huerfano *et al.*, 2010). The plasmid pcDNA3.1 was obtained from Invitrogen.

CpG analysis

Sequences of the gateway plasmids used in the study were analyzed by using the EMBOSS, CpGPlot program (web-based program) available at EMBL-EBI (www.ebi.ac.uk). For

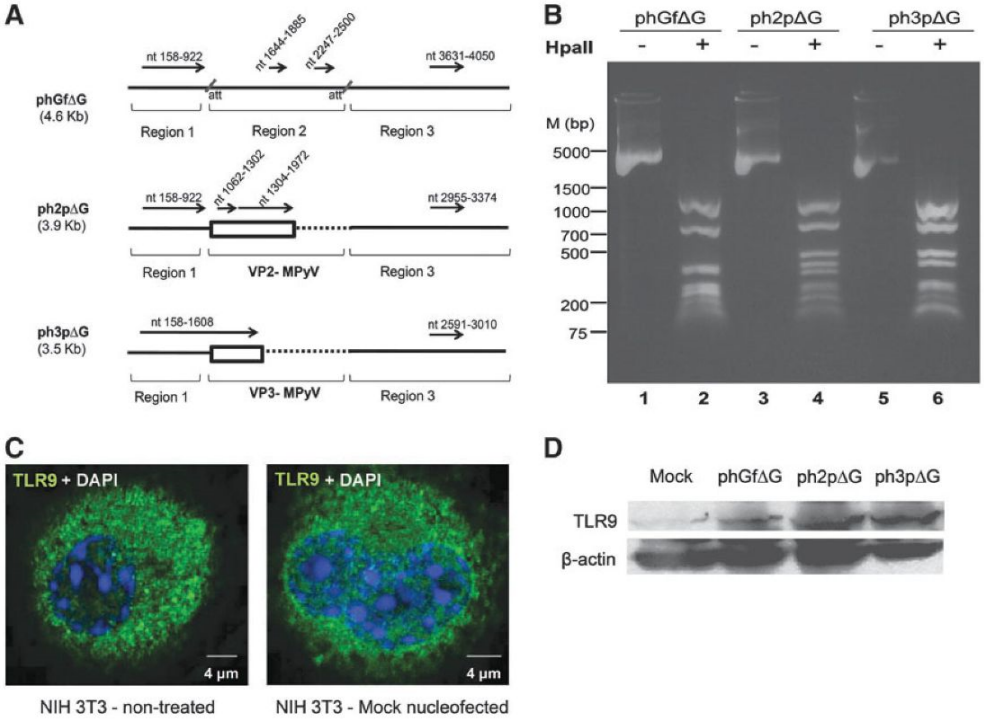

FIG. 1. Unmethylated CpG motifs in the plasmids and presence of the Toll-like receptor-9 (TLR9) in the NIH3T3 cell line. **(A)** Analysis of the presence and distribution of CpG dinucleotides was performed by means of EMBOSSES CpGPlot. The CpG motifs of plasmid DNA are presented by black arrows, the position of the motifs within the plasmid are indicated on the top of the arrows in nucleotide (nt) numbers. The boxes in bold represent the sequences of *VP2* and *VP3* of Mouse polyomavirus (MPyV). Sequences of the phGfΔG plasmid were arbitrarily divided into three regions. Dotted lines in the expression vectors, ph2pΔ and ph3pΔG, indicate sequences deleted by cloning. **(B)** The methylation state of phGfΔG plasmid (lanes 1, 2), ph2pΔG plasmid (lanes 3, 4), or ph3pΔG plasmid (lanes 5, 6) was tested by *Hpa* II digestion. *Hpa*II digested (lanes 2–4) and control non-digested (lanes 1, 3, 5) plasmids were resolved by 0.8% agarose electrophoresis. **(C)** Confocal section of NIH3T3 cells (untreated or mock-transfected cells) stained with antibody against the TLR9 receptor (green) and by DAPI. **(D)** Levels of the TLR9 protein in cells nucleofected with phGfΔG, ph2pΔG, or ph3pΔG plasmids and in mock-transfected cells (4 h post-transfection) were analyzed in Western blots using anti-TLR9 antibody. Antibody against β-actin was used as loading control.

the analysis, we used standard parameters (Window length 100, Obs/Exp CpG ratio 0.6, Min C+G 50%, and Min Length 200).

Plasmid DNA digestion and methylation

DNA was subjected to cleavage by restriction enzyme, *Hpa*II (Thermo Scientific). Restriction digestion was confirmed by 0.8% agarose gel electrophoresis stained by Gel red nucleic acid stain™ (Biotium). In addition, when required, DNA was methylated using the CpG methyltransferase M.SssI (New England Biolabs), according to manufacturer's instructions.

Quantitative real-time polymerase chain reaction

Total RNA was extracted using the High Pure RNA Isolation Kit (Roche) according to the manufacturer's protocol. The RNA concentration was measured by a spectrophotometer, and the integrity was evaluated using an Agilent 2100 bioanalyzer (Agilent); reverse transcription was carried out with the iScriptcDNA Synthesis kit (Bio-Rad Laboratories) according to a producer's manual. cDNAs were amplified by polymerase chain reaction (PCR) using primers sets:

STAT1, 5′-GGAGGTGAACCTGACTTCCA-3′ and 5′-TCTGGTGCTTCCTTTGGTCT-3′; Mx-1, 5′-GGTCGGCTTCTGGTTTTGTA-3′ and 5′-GAACAGGTCCACTTCCTCCA-3′; IRF1, 5′-CCTGGGTCAGGACTTGGATA-3′ and 5′-TTCGGCTATCTTCCCTTCCT-3′; IRF7, 5′-GAAGACCCTGATCCTGGTGA-3′ and 5′-CCAGGTCCATGAGGAAGTGT-3′; and IFNβ, 5′-CCCTATGGAGATGACGGAGA-3′ and 5′-CTGTCTGCTGGTGGAGTTCA-3′.

Quantification of PCR products in real time was performed in a Light Cycler 480 II from Roche using the Light Cycler® 480 SYBR Green I Master kit, according to the manufacturer's protocol. Quantification of target gene expression was performed using Light Cycler 480 II software based on the relative quantification method, determining the concentration of target amplicons normalized to the reference *β-actin* gene.

IFNβ measurement

IFNβ was assessed in sample supernatants using the Verikine™ IFNβ kit, a sandwich enzyme-linked immunosorbent assay (ELISA) from PBL Biomedical Laboratories, according to the manufacturer's recommended protocol. In brief, after transfection, 1.2×10^6 cells were resuspended in 2.5 mL of DMEM supplemented with serum, seeded into 3-cm plates and incubated at 37°C in a humidified incubator with 5% CO_2 atmosphere. Supernatants were collected at indicated times and ELISA was performed. Absorbance was measured by an ELISA reader (450 nm).

Evaluation of cytotoxicity

The release of LDH occurring upon cell lysis was quantified using a CytoTox 96 cytotoxicity assay kit (Promega), according to the manufacturer's instructions. Briefly, cells were transfected and then seeded on 24-well plates, and 2 h post-transfection, the medium was replaced by fresh medium to remove the cells that died due to the electrical pulse. Later, at indicated times, the medium from growing cells were collected to measure LDH. The total numbers of cells was obtained by treatment of cells with Triton X-100. Absorbance was measured by an ELISA reader (490 nm).

Proliferation assay

After transfection, the cells were resuspended in complete medium, seeded on 96-well tissue culture plates (confluence of ~20%) and incubated at 37°C in a humidified incubator with 5% CO_2 atmosphere. After 2 h, the medium was replaced by fresh medium and the cells were further incubated and, at selected times, we tested the ability of cells to cleave the tetrazolium salt to formazan as an indicator of an active metabolism in cells. Briefly, proliferation reagent, WST-1 (Roche) was suspended in medium without red phenol (ratio 1/10) and 100 μL of the suspension was added to cells. Cells were further incubated at 37 °C for 3 h and then the absorbance was measured by an ELISA reader (450 nm).

Western blot analysis

Cells were harvested at the indicated time points and washed with phosphate-buffered saline (PBS), then they were resuspended in ice-cold cell lysis buffer (10 mM Tris/HCl, pH 7.4, 1 mM EDTA, 150 mM NaCl, 1% Nonidet P-40, 1% sodium deoxycholate, and 0.1% SDS) supplemented with a protease inhibitor cocktail (Complete Mini EDTA free [Roche]). Cell lysis was carried out by incubating the cells for 20 min on ice. Cell debris was removed by centrifugation. The concentration of proteins was determined using a standard Bradford protein assay. Cellular proteins (50 μg) were applied to SDS/PAGE, blotted onto polyvinylidene difluoride membranes, immunostained with antibodies, and developed using an enhanced chemiluminiscence reagent (Pierce).

Immunofluorescence analysis

Cells were grown on coverslips and, at indicated times postnucleofection, cells were fixed, with 4% paraformaldehyde for 15 min and permeabilized with 0.5% Triton X-100 in PBS for 5 min. After washing in PBS, cells were incubated with 0.25% bovine serum albumin and 0.25% porcine skin gelatin in PBS for 30 min. Immunostaining with primary and secondary antibodies was carried out for 1 h and 30 min, respectively, with extensive washing with PBS after each incubation. Coverslips were mounted on droplets of glycerol with 4′, 6′-diamidino-2-phenylindole (DAPI). Images were obtained by using a Leica TCS SP2 confocal microscope.

Antibodies

The antibodies used were mouse monoclonal anti-phospho-Histone H2A.X (Ser 139) (Millipore); mouse monoclonal anti β-actin (Sigma-Aldrich); rabbit polyclonal anti-TLR9 (Abcam); rabbit polyclonal anti-IRF3 (Abcam); rabbit monoclonal anti-phospho IRF3 (Ser 396) (Cell Signaling Technology); rabbit polyclonal anti-NF-κB p65 (Santa Cruz); goat anti-mouse and goat anti-rabbit conjugated with peroxidase (Pierce); and goat anti-rabbit IgG conjugated with Alexa fluor 488 (Molecular Probes).

Results

Analysis of CpG distribution and methylation state of the plasmids

We have previously found that introduction of plasmid DNA by nucleofection into mouse fibroblasts induces upregulation of the endosomal receptor, TLR9 (our unpublished results). Since TLR9 recognizes unmethylated CpGs, we evaluated the quantity of the CpG motifs in the plasmids and their methylation state. For this study, we used the plasmid, phGf, a gateway-adapted destination plasmid and two of its derivatives, the expression vectors, ph2p and ph3p, that were previously prepared by insertion of the sequences encoding the minor structural proteins VP2 or VP3, of MPyV into phGf (Tolstov *et al.*, 2009). The plasmids include an ORF that codes for the EGFP protein. We removed the EGFP sequences to exclude any cellular responses that could be launched by EGFP expression. The modified products were named phGfΔG (destination vector), ph2pΔG, and ph3pΔG (expression vectors). Table 1 summarizes the features of the plasmids. Before CpG analysis, we arbitrarily divided the sequence of phGfΔG into three regions (Fig. 1A) to facilitate

Table 1. Plasmid Features and Its Expression Products

Name	*Size (bp)*	*Type of plasmid according to gateway system*	*Expression products*
phGf	5608	Destination plasmid	EGFP
ph2p	4932	Expression vectors	EGFP and VP2
ph3p	4568		EGFP and VP3
phGfΔG	4601	Destination plasmid	None
phGfΔGΔR	2855	Destination plasmid without region between *att* sites	None
ph2pΔG	3925	Expression vectors	VP2
ph3pΔG	3561		VP3
pEGFP-N1	4728	Non gateway	EGFP
pEGFP-VP2	5688	Non gateway	EGFP-VP2
pEGFP-VP3	5343	Non gateway	EGFP-VP3
pcDNA3.1	5428	Non gateway	None

the description of the CpG motifs. In expression vectors (ph2pΔG and ph3pΔG), the region 2 (between *att* sites) was lost during cloning by recombination and was replaced by a gene of interest, in this case by the MPyV *VP2* or *VP3* genes (Fig. 1A). We evaluated the presence of CpG motifs in the plasmids by using the cgplot program from the European Molecular Biology Laboratory-European Bioinformatics Institute (EMLB-EBI) commonly used to study vertebrate genomes to find promoters of housekeeping genes (Larsen *et al.*, 1992). The program identifies regions of at least 200 nucleotides with a high content of GC (>50%) and observed/expected ratio of CpG greater than 0.6 (Gardiner-Garden and Frommer, 1987). The results of the analysis are summarized in Figure 1A. We found that the positive strand of PhGfΔG has four predicted islands, one long (~700 bp) located in region 1, two short islands (~200 bp) within region 2, and one medium size island (~ 400 bp) in region 3. The expression plasmids coding for the VP2 and VP3 proteins retained the same long and middle size motifs of regions 1 and 3 as phGfΔG. In addition, the ph2pΔG plasmid has two islands in the VP2 sequence, a long one (669 bp) and a short one (241 bp); the ph3pΔG plasmid DNA has one island in the VP3 sequence that joins the long island of region 1, resulting in a very long island (~1400 bp). For the complement strands of all plasmids used, similar regions were predicted as for the positive ones (Supplementary Table S1; Supplementary Data are available online at www.liebertpub.com/dna).

Next, to follow the methylation state of some of the CpG sequences within the plasmids, we used the restriction enzyme, *Hpa*II, which recognizes only unmethylated CpG within the sequence 5′…C**CG**G…3′ (Fig. 1B). The plasmid phGfΔG contains 23 repetitions of this sequence, while ph2pΔG or ph3pΔG contain 16 and 15, respectively (Supplementary Table S2). Some of the fragments produced by *Hpa*II digestion have very similar length or are too small to be properly resolved by agarose gel electrophoresis. However, we were able to relate at least six bands in digest of each of the three plasmids to the sizes of the expected fragments (Supplementary Table S2). From this experiment, we can conclude that each plasmid contains at least some unmethylated CpG dinucleotides.

Evaluation of the presence of the TLR9 receptor in NIH3T3 fibroblasts

We hypothesized that the IFN response is induced after recognition of unmethylated CpGs by the TLR9 endosomal receptor. Supporting our hypothesis, three studies (Li *et al.*, 2004; Platz *et al.*, 2004; Di *et al.*, 2009) reported responses to CpGs through TLR9 of nonimmune cells. Another two studies reported that both immune and nonimmune cells rapidly upregulate the production of the receptor after exposure to agonists of TLR9 (Bourke *et al.*, 2003; Ewaschuk *et al.*, 2007). Therefore, we followed the expression of the TLR9 in the 3T3 fibroblast cell line. First, we confirmed by indirect immunofluorescence that 3T3 fibroblasts produce TLR9 under standard growing conditions and that the production is not affected by mock nucleofection (Fig. 1C). In addition, we evaluated by western analysis the levels of TLR9 after nucleofection of the cells and found an upregulation of TLR9 after nucleofection with plasmid DNAs but not after mock nucleofection (Fig. 1D). Next, we characterized the type I IFN response rendered by introduction of plasmids into the mouse fibroblasts and evaluated the role of CpG motifs in this response.

Type I IFN response after plasmid DNA nucleofection

We first measured the levels of *IFNβ* mRNA by quantitative real-time-PCR (qRT-PCR) and secretion of IFNβ protein by ELISA (Fig. 2A, B, respectively). We detected high levels of *IFN*β mRNA in cells transfected with phGfΔG and only moderate amounts of I*FNβ* mRNA in cells transfected with either ph2pΔG or ph3pΔG 2 h post-transfection. In agreement with this result, at this time post-transfection, we were able to detect IFNβ only in the growing medium of cells transfected with phGfΔG (the method we used for measuring IFN has a sensitivity of 15 pg/mL). However, later, 5 h post-transfection, a higher production of *IFNβ* mRNA correlated with high levels of IFNβ for all transfected cells. Nevertheless, the production of IFNβ was ~2.5 times lower in cells transfected with either ph2pΔG or ph3pΔG in comparison with cells transfected with phGfΔG. To exclude any possible differences in the uptake of the plasmids, we determined the efficiency of transfection using the original phGf plasmid encoding EGFP as destination vector, or expression vectors (ph2pΔG or ph3pΔG) encoding the minor structural proteins of MPyV. We found that the efficiency of transfection was similar (~25%–34%) for all three plasmids (Supplementary Table S3), indicating that the uptake of plasmids was also similar. All together, the above results show that region 2, which is present only in the phGfΔG vector, may contain sequences that positively affect vector recognition by DNA sensors. The levels of IFN produced in cells transfected with the phGfΔG plasmid were very high, comparable with those described, for example, in Rautsi *et al.* (2007) for potent inducers of IFN - mRNA from mouse muscles cells, or by *in vitro* transcribed RNA of vesicular stomatitis virus glycoprotein.

The remarkably stronger IFN production induced by the phGfΔG vector in comparison with that induced by ph2pΔG or ph3pΔG raised a question of possible differences in subsequent steps of the IFN signaling that might result in a different expression of IFN-inducible genes. To answer this question, we quantified the mRNA levels of IFN-inducible genes, *IRF1*, *IRF7*, and genes activated during the establishment of the antiviral state, including *Mx-1* and *STAT1* (Fig. 2C). We found a remarkable but comparable induction of transcription of *IRF1*, *IRF7*, and *STAT1* in cells transfected with either plasmid 5 h post-transfection. This indicates that in spite of the different levels of IFN produced, all three plasmids induce IFN signaling resulting in establishment of the antiviral state. However, supporting the very high IFNβ induction by the phGfΔG plasmid, markedly stronger *Mx-1* expression was detected in cells transfected with this plasmid.

There is an important fact that should be considered. The destination vector, phGfΔG, induced a strong and very fast IFN response (within 2 h), while IFN response induced by expression vectors, ph2pΔG or ph3pΔG, was weaker and delayed (detected 5 h post-transfection). This makes us speculate about the nature of the IFN induction launched by expression vectors. There are three possibilities to explain

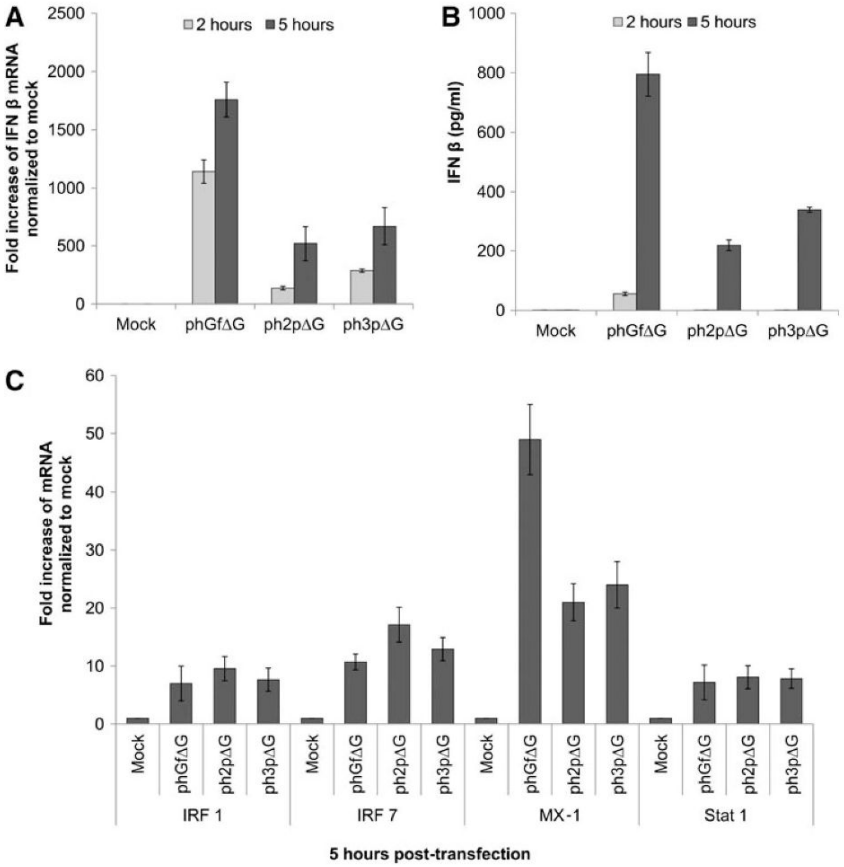

FIG. 2. Interferon (IFN) type I response after nucleofection of mouse NIH3T3 fibroblasts with phGfΔG plasmid or its derivatives. Cells were transfected with phGfΔG, ph2pΔG, or ph3pΔG plasmids at the indicated times post-transfection. Cells were harvested for preparation of mRNAs **(A, C)** and growth medium supernatants for measurement of secreted IFN **(B)**. **(A)** The level of *IFNβ* mRNA was measured by quantitative real-time polymerase chain reaction (qRT-PCR). **(B)** The production of IFNβ was analyzed by enzyme-linked immunosorbent assay (ELISA). **(C)** The levels of mRNA of genes regulated during IFN responses, *IRF 1*, *7*, *MX-1*, and *STAT 1*, were measured by qRT-PCR. For all experiments **(A–C)**, mock-transfected cells were included as a negative control. Data represent the mean values of three independent experiments.

this: (1) either DNA regions remaining in expression vectors from phGfΔG are less efficiently recognized by cells (e.g., due to the influence of different adjacent sequences) and therefore, the IFN response is delayed; (2) the induction is caused by the inserted nucleotide sequence of the minor proteins; and (3) the *VP2* and *VP3* gene products might be responsible for the delayed IFNβ production. To test the role of vector sequences in the IFN responses, we modified the destination vector phGfΔG by deleting the region between the *att* sites (see Fig. 1A), thus, generating the double modified destination vector phGfΔGΔR, which corresponds to phGfΔG vector sequences present in expression vectors ph2pΔG and ph3pΔG. Then, we nucleofected the cells by the double modified plasmid and quantified *IFNβ* mRNA levels. We found that levels of IFN induction are similar to those obtained after delivering the expression vectors by nucleofection (Fig. 3A). To test the contribution of gene or amino acid sequences of VP2 or VP3 to the IFN responses, we used the pEGFP-N1 vector and its derivatives, VP2-EGFP-N1 and VP3-EGFP-N1 carrying EGFP fusion genes for VP2 or VP3 (Huerfano *et al.*, 2010). Features of these plasmids are shown in Table 1. A comparison of the IFN levels produced by transfection of pEGFP-N1 vector versus its derivatives, VP2-EGFP-N1 and VP3-EGFP-N1, is straightforward since the traditional method of cloning via restriction enzyme cleavage preserved all vector sequences after cloning. Efficiencies of transfection by using these plasmids were comparable (33%–39%; Supplementary Table S3), thus allowing us to compare responses induced by them. We measured the levels of IFNβ 5 h post-transfection (Fig. 3B) and found that cells transfected with pEGFP-N1, or with its derivatives, induced comparable amounts of IFNβ, indicating that neither *VP2/VP3* gene sequences nor their products play a significant role in the response. From these experiments, we can conclude that similarly, in the case of ph2pΔG or ph3pΔG plasmids, the IFN response is induced by vector DNA sequences. An additional observation that can be extracted from the above data is that nucleofection of NIH3T3 cells induces an IFN response not only with phGfΔG-derived plasmids but also with the pEGFP-N1 plasmid. As pEGFP-N1 encodes EGFP, we cannot exclude the contribution of the EGFP protein to the response. Therefore, to test the induction of IFN responses by another unrelated plasmid, we investigated the antiviral state establishment (by quantification of *Mx* mRNA) after nucleofection by commonly used pcDNA3.1 (features of the plasmid are shown in Table 1). The results presented in Figure 4A show that nucleofection of the pcDNA3.1 plasmid also induced a remarkable upregulation of *Mx* gene expression. Thus, nucleofection of different plasmid DNAs into NIH3T3 apparently can induce IFN responses.

We were interested whether dsDNA nucleofection induces IFN responses also in other cell lines. Therefore, we

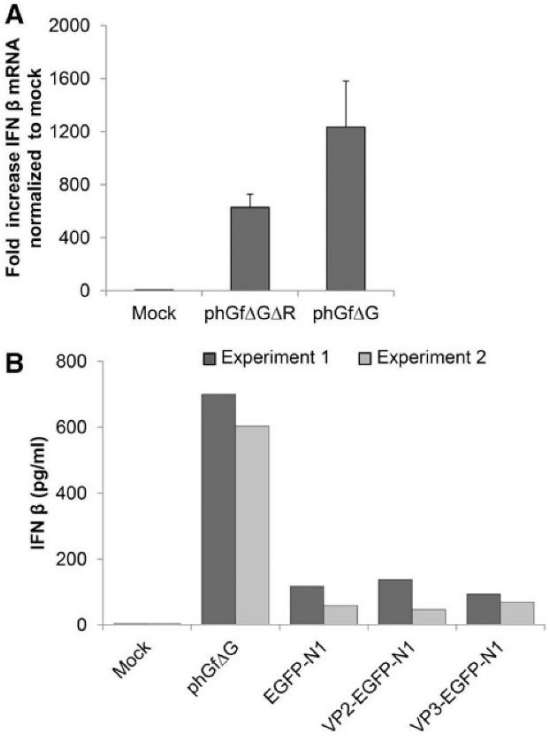

FIG. 3. IFN induction after nucleofection of mouse fibroblasts with plasmid DNAs. **(A)** The double modified destination vector, phGfΔGΔR, was introduced into NIH3T3 cells by nucleofection and the levels of *IFNβ* mRNA at 5 h post-transfection were quantified by qRT-PCR. Data represent the values of three experiments. **(B)** NIH3T3 cells were nucleofected with VP2-EGFP-N1, VP3-EGFP-N1, or EGFP-N1, and at 5 h post-transfection, the supernatants of growing cells were used for detection of IFNβ levels by ELISA. Data represent the values of two independent experiments. For all experiments **(A, B)** mock-transfected cells were used as a negative and cells transfected with phGfΔG plasmid as a positive control.

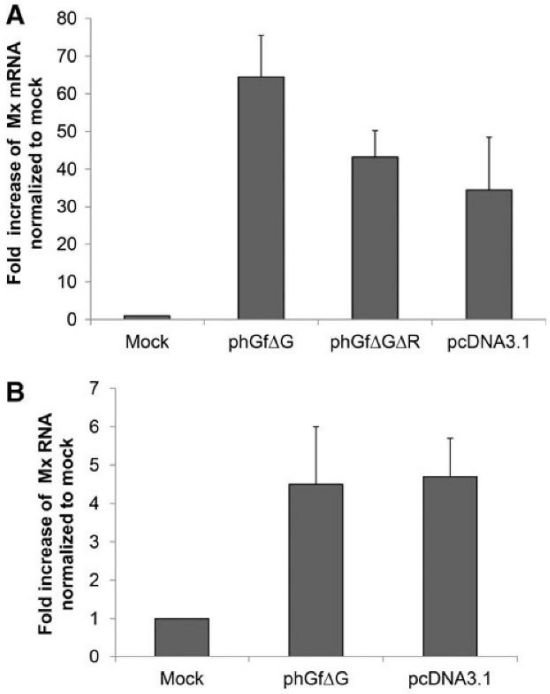

FIG. 4. Establishment of the antiviral state after nucleofection of NIH3T3 or mouse embryonic fibroblast (MEF) cells with plasmid DNAs. Mouse 3T3 fibroblast **(A)** or MEF cells **(B)** were nucleofected with the indicated plasmid and, 5 h post-transfection, the levels of *Mx* mRNA were quantified by qRT-PCR. Mock-transfected cells were used as a negative control.

measured the levels of of *Mx* mRNA in primary MEF cells nucleofected with either pcDNA3.1 or phGfΔG plasmids. Quantitative PCR performed 5 h postnucleofection revealed that both plasmids induced upregulation of *Mx* gene expression (Fig. 4B). However, because of very low transfectability of these cells (only 5% of cells expressed EGFP after transfection with the phGf plasmid), we were not able to compare the IFN response of NIH3T3 and MEF cell lines. Nevertheless, we can conclude that, also MEF cells respond to nucleofection with dsDNA by induction of IFN responses.

DNA signaling and the cell fate

To follow possible DNA damage signaling induced by nucleofection with the gateway plasmids, we evaluated the presence of γ-histone 2A.X. This histone is a modified isoform of histone 2A.X, produced by phosphorylation of the serine in position 139 by ataxia telangiectasia mutated (ATM) or DNA-dependent protein kinase (DNA-P) or by other kinases in response to dsDNA breaks (Li *et al.*, 2005). As soon as 2 h post-transfection, we observed an upregulation of γ-histone 2A.X in cells transfected with phGfΔG (Fig. 5A). The early sensing of DNA damage coincides with the early production of IFNβ (Fig. 2B). Interestingly, cells transfected with the expression vectors ph2pΔG or ph3pΔG exhibited DNA damage later (after 5 h post-transfection) at the time that coincided with the detection of IFNβ.

As we detected γ-histone 2A.X upregulation sensing DNA damage in the cells nucleofected with the phGfΔG plasmid, we were interested in the fate of the transfected cells. As it has been described that prolonged IFNβ treatment induces cell death or inhibition of cell proliferation, we tested both cytotoxicity and the ability of the cells to proliferate. First, we followed cell death by measuring the release of lactate dehydrogenase as an indicator of membrane damage at different times post-transfection. Cells transfected with the phGfΔG plasmid did not undergo significant cell death when compared with the mock transfected control cells (Fig. 5B), indicating that, in spite of high IFN levels, there is no induction of cell death (within 24 h post-transfection). The cells transfected with the expression vectors coding for VP2 and VP3 died after 24 h as expected since the proteins were able to bind and perforate membranes and to induce cell death

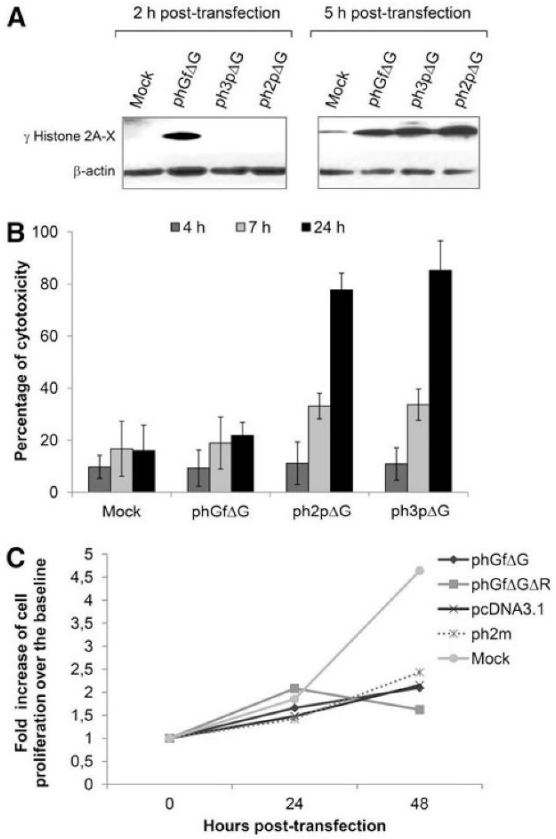

FIG. 5. DNA damage signaling and fate of NIH3T3 cells after nucleofection with plasmid DNAs. Cells were nucleofected by Amaxa with phGfΔG, ph2pΔG, or ph3pΔG plasmids. At the indicated times post-transfection, cells or supernatants were collected. **(A)** Proteins of cell lysates were immunobloted for detection of γ-histone 2A.X. Detection of β-actin was performed as a control for sample loading. **(B)** The medium of the growing cells was collected to evaluate cytotoxicity by measuring LDH. Values are related to that of LDH release obtained by treatment with 9% Triton X-100 (=100%). Data represent the mean values obtained by measuring duplicates of three independent experiments. **(C)** Cell proliferation was followed by measuring bioreduction of tetrazolium salt, using an ELISA reader (450 nm). OD values were aligned to the baseline (0 time, OD value) and the resulting fold increase values were plotted. Three independent experiments were performed, and comparable results were obtained. For better graph clarity, the results of one representative experiment are presented. For all experiments **(A–C)**, mock-transfected cells were used as a negative control.

(Huerfano *et al.*, 2010). Then, we followed the rate of cell division, after 24 and 48 h post-transfection. We could not compare the influence of the phGfΔG plasmid presence on cell proliferation with that of the MPyV VP2- and VP3-expressing vectors, ph2pΔG or ph3pΔG, for high toxicity of VP2 and VP3 proteins. Therefore, apart from phGfΔG, we included two additional plasmids in this experiment for comparison. One of them, the ph2m plasmid, is a derivative of phGf carrying the gene of the VP2 minor structural protein of the MCPyV. Unlike the MPyV structural proteins, VP2 of the MCPyV possess only weak (if any) cytotoxicity when measured up to 24 h postnucleofection (our unpublished results). The second plasmid, phGfΔGΔR, contains only phGfΔG sequences present in the expression vectors. We found that nucleofection of either of the plasmids, caused arrest of cell cycle progression (Fig. 5C). This indicates that nucleofection by the plasmids derived from the phGf gateway plasmid (but not mock nucleofection) induces inhibition of cell proliferation. In addition, we also evaluated the rate of proliferation of NIH3T3 cells after nucleofection with the pcDNA3.1 plasmid (Fig. 5C) and also found that transfection by this plasmid caused arrest of cell cycle progression.

Turbofect cationic transfection instead of nucleofection dramatically decreased IFNβ induction

Transfection of naked DNA or wrapped by a cationic solution is known to induce differential IFN responses (Rautsi *et al.*, 2007). Therefore, we evaluated the induction of IFN when transfecting cells by turbofect (cationic solution) with the phGfΔG destination vector or ph3pΔG and ph2pΔG expression vectors. First, we evaluated the efficiency of transfection as an indicator of DNA uptake using the destination vector, phGf carrying EGFP-coding sequences and expression vectors, ph2pΔG or ph3pΔG for expression of the MPyV *VP2* or *VP3* genes. We found that for all the plasmids, the amounts of cells expressing genes carried by vectors were similar (~15%–18%, see Supplementary Table S3). Efficiency of transfection was lower (approximately one half) when compared to values reached by nucleofection. In agreement with our results, differences in efficiency of transfection by using different methods have been documented (Maurisse *et al.*, 2010; Contreras *et al.*, 2012). Next, we measured the levels of secreted IFNβ by ELISA. Surprisingly, we were not able to detect any IFN, indicating that IFN production by cells (if any) was under the detection limit of our system (15 pg/mL). Therefore, we proceeded by measuring *IFNβ* mRNA levels by RT-PCR at 8 and 24 h post-transfection. Figure 6 shows increased *IFNβ* transcription in cells transfected with all three plasmids when compared with mock-transfected cells. As in the nucleofection experiments, IFN transcription was the highest for cells transfected with the phGfΔG plasmid. However, the levels of IFN induction by all plasmids were dramatically decreased. While induction of IFN by phGfΔG plasmid was increased 1000-fold (in comparison with mock nucleofection), at the time 5 h-post-nucleofection, only approximately sevenfold increase was detected 24 h postturbofection with the same plasmid (in comparison with mock turbofection). From all these results, it can be concluded that the method of DNA delivery into cells is crucial for the strength of the IFN response.

The mechanism of recognition of nucleofected DNA is TLR9 independent and involves NF-κB activation

For evaluation of the contribution of the CpG motifs to the IFN responses, we methylated cytosine residues within the recognition sequence 5′…CG…3′ of the phGfΔG destination plasmid by the methyltransferase M.SssI. Methylation of the plasmid was confirmed by prevention of digestion by *Hpa*II

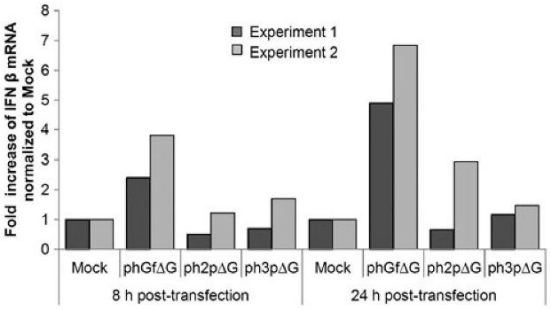

FIG. 6. IFNβ induction in NIH3T3 cells transfected by Turbofect. Cells were transfected with phGfΔG, ph2pΔG, or ph3pΔG plasmids and at the indicated times post-transfection, mRNA was extracted. The levels of IFNβ mRNA were quantified by RT-PCR. Data of two independent experiments are presented. Mock-transfected cells were used as a negative control.

(Fig. 7A). Then, we transfected the cells with the unmethylated or methylated plasmids and, 5 h after nucleofection, measured the production of IFNβ by ELISA (Fig. 7B). We did not find any significant differences in the IFN levels in the cells transfected with methylated or unmethylated DNA. This indicates that there are apparently other features of the plasmid DNA rather than CpG motifs sensed by cells, and that, cytoplasmic DNA sensors (and not the endosomal TLR9 receptor), are responsible for sensing the DNA. To follow the possible pathways involved in IFN induction through DNA sensors, we investigated the role of IRF3, and NF-κB transcription factors in the signaling. IRF3 is ubiquitously expressed and activated by serine phosphorylation at its C-terminus, in the serine/threonine cluster site. Phosphorylation promotes dimerization of the protein. Dimers, translocate to the nucleus to bind specific DNA targets (Lin *et al.*, 1998) Transcription factor, NF-κB, consists of homo- and heterodimers of NFκB1/p50 and RelA/p65 subunits. NF-κB dimers become activated by induced proteasomal degradation of the IkB inhibitor. Active NF-κB transcription factor subunits translocate to the nucleus and induce target gene expression (Baeuerle and Baltimore, 1988). We selected these two transcription factors because they were found to be activated by transfection of double-stranded oligonucleotides into mouse fibroblasts (Ferguson *et al.*, 2012). In addition, IRF3 has been involved in signaling induced by at least four of nine described DNA sensors, while NF-κB has been involved alone or in conjunction with IRF3 in at least three of nine described sensors (Keating *et al.*, 2011). We followed by confocal microscopy the translocation of NF-κB and IRF3 into the cell nucleus after nucleofection of cells with the phGfΔG plasmid. One hour post-transfection NF-κB exhibited marked nuclear localization in a significant subpopulation of cells (Fig. 8A) (~12% of the whole cell population, where efficiency of nucleofection by phGf transfection was 25.5%), while only 4% of such cells were detected in mock-transfected cells. IRF3 was located almost exclusively in the cytoplasm at any of the times examined (40 min, 1, 3, and 5 h post-transfection) (Fig. 8B, shows representative pictures). We noticed that ~2% of both nucleofected and mock-nucleofected cells exhibited a low level of IRF3 in the nucleus (see Fig. 8B picture 3, bottom panel). As IRF3 is known to have an important role in signaling through many DNA sensors, we decided to follow, in addition to nuclear translocation, serine phosphorylation of the protein at 1, 3, and 5 h post-transfection. Although we were not able to detect any phosphorylated IRF3 after 1 h (not shown) or 5 h post-transfection, very low signal of the phosphorylated protein was detected 3 h post-transfection (Fig. 8C, top). Intriguingly, from 3 h post-transfection, abundant levels of a product of low molecular weight recognized by the antibody against phosphorylated IRF3 were observed in plasmid-transfected but not in mock-transfected cells (Fig. 8C, top). The fact that the product was detected also by a polyclonal antibody recognizing IRF3 regardless of its phosporylation (in lysates of cells transfected with plasmid and in mock-transfected cells) (Fig. 8C, bottom) suggests that it might be a degradation product of IRF3. Together, the data suggest a role for NF-κB in IFN induction, while the role of IRF3 is not so clear. If there is a role of IRF3 in IFN induction, the activation seems to be dynamic and tightly regulated by cells. Thus, both nuclear translocation of IRF3 and its phosphorylation were difficult to follow.

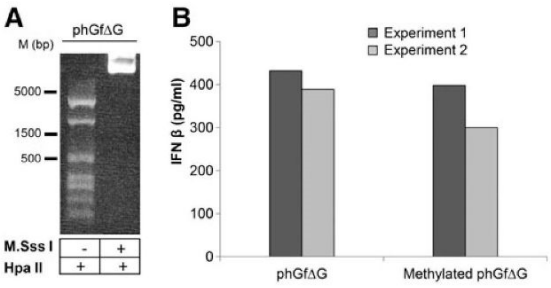

FIG. 7. Production of IFNβ by NIH3T3 cells after nucleofection with methylated or unmethylated phGfΔG plasmid DNA. **(A)** The phGfΔG plasmid was treated with the methyltransferase M. SssI to methylate the CpG motifs. Prevention of the digestion by *Hpa*II indicated the methylation state of the plasmid. Untreated plasmid was used as a positive control of *Hpa*II digestion. **(B)** Cells were transfected either with unmethylated or methylated plasmid, and the levels of IFNβ production were assayed by ELISA. The data represent the values of two independent experiments.

Discussion

Transfection of cells by plasmid vectors is a widely used method to obtain efficient expression of desired genes for studying cellular responses to their expression or the behavior of their products. However, the insertion of DNA into the cells induces immunoresponses that could interfere with the result interpretation in an experimental setting. In this study, we documented a strong IFN response, DDR activation, and inhibition of cell proliferation induced by nucleofection of mouse fibroblasts with plasmid DNA. Interestingly, we did not find high levels of IFN when transfecting the same plasmids by the cationic polymer (Turbofect) into the cells. These results point to the role of a DNA entry mechanism as key for DNA sensor recognition.

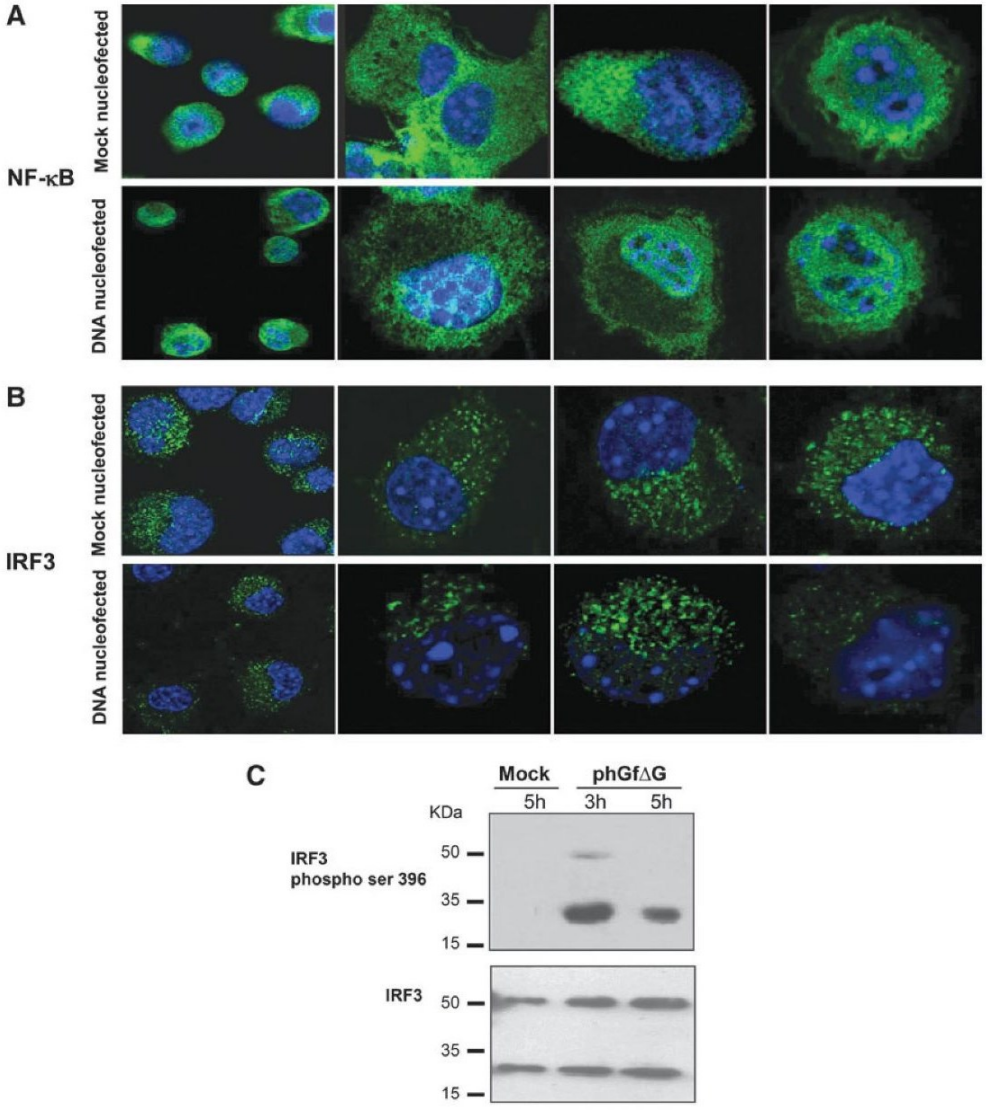

FIG. 8. Activation analysis of transcription factors NfκB and IFN regulatory factor (IRF3). **(A, B)** Activation of the factors was followed 1 h postnucleofection of NIH3T3 cells with phGfΔG plasmid or after mock nucleofection. Selected confocal microscopy sections are presented. Cells were fixed and stained by **(A)** an antibody against nuclear factor-kappa (NF-κB) p-65 (green) and by DAPI (blue) or by **(B)** an IRF3-specific antibody (green) and DAPI (blue). **(C)** IRF3 phosphorylation in NIH3T3 cells nucleofected with phGfΔG or mock nucleofected was analyzed by Western blotting. Cells were lysed at the indicated times, separated by SDS electrophoresis, and blotted. Immunostaining was performed by phospho-IRF3 (Ser396) antibody, specific for the epitope containing phosphorylated serine at position 396. Polyclonal antibody against the IRF3 protein was used as a control.

In detail, although the mechanism of DNA cell delivery during transfection is not completely understood it is known that DNA delivered by liposomes or cations enters the cells via endocytosis (Legendre and Szoka, 1992; Yasuda *et al.*, 2005). Variations in the type of early endosomes that transport the DNA (fast maturing or static) or differences in the mechanism of DNA escape from endosomes may be responsible for the differences in DNA sensing and in the efficiency of nuclear delivery (review in Nguyen and Szoka, 2012).

Even less is known about electroporation. Until very recently, it was accepted that DNA may enter cells through transient membrane pores. In 2011, Rosazza *et al.* (2011) demonstrated that during DNA electroporation, actin polymerizes under the plasma membrane in places where DNA is aggregated. The authors postulated that there is formation

of endocytic-like vesicles (Rosazza *et al.*, 2011). Interestingly, nucleofection is a type of electroporation that combines electrical parameters with a buffer solution, which, by an unknown mechanism, delivers DNA straight into the cell nucleus (Gresch *et al.*, 2004). We speculated that the "straight delivery" of DNA into the nucleus proposed as a mechanism for nucleofection, implies only a faster cytoplasmic DNA traffic, since, in our model, DNA cytoplasmic sensors were activated by nucleofected DNA. The way of trafficking of this DNA and the mechanism of its sensing by cell cytoplasmic sensors has to be assessed. Apparently, unlike cationic DNA delivery, nucleofection arouses DNA recognition by cytoplasmic DNA sensors. We found early post-nucleofection translocation of NF-κB suggesting the role of this transcription factor in signaling, which leads to IFN production. The role of IRF3 in light of our results remains controversial. At first, lack of nuclear translocation of the protein strongly suggests that the factor is not signaling. The low levels of IRF3 in the nuclei of some cells (DNA or mock nucleofected) are consistent with the fact that the protein normally shuttles between the nucleus and the cytoplasm, and due to the presence of nuclear export signals in the protein, the cytoplasmic subpopulation is dominant (Lin *et al.*, 1998). The presence of a small subpopulation of IRF3 phosphorylated at serine 396 in cells 3 h post-transfection with phGfΔG (Fig. 8C) may indicate some activation of the protein that, however, does not result in significant translocation of IRF3 but rather in its degradation as suggested by the appearance of low molecular weight product recognized by antibody specific for phosphorylated IRF3. The possibility that phosphorylation of IRF3 may represent a signal for subsequent degradation by the proteasome pathway was previously suggested (Lin *et al.*, 1998). Further investigation will be required to identify the specific sensor responsible for dsDNA sensing in mouse NIH3T3 fibroblasts and the role of IRF3 in consequent signaling leading to IFN induction.

Although the plasmids used here were rich in unmethylated CpG motifs, and cells were overexpressing TLR9, we demonstrated that the motifs did not play an important role in foreign DNA recognition. The reason can be (1) in the method of transfection and/or (2) in the absence of recognition of sequences flanking the CpG motifs. Indeed, Yoshinaga *et al.* (2006) found that macrophages responded with higher production of inflammatory cytokines when stimulated by DNA containing CpGs complexed with cationic lipids rather than by naked DNA. In our hands, CpG motifs apparently did not contribute to the IFN signaling either when Amaxa nucleofection was used or during cation polymer delivery. Nevertheless, it is also possible that the sequences flanking CpG motifs in our vectors prevent receptor recognition. It has been described that differences in the levels of IFN response in humans and mice were caused by varying recognition of the CpG's flanking sequences by these two species (Weiner, 2000).

In addition, although we found some differences in IFN responses induced by Amaxa nucleofection with different plasmids, phGfΔG, phGfΔGΔR, or pcDNA3.1, we observed that the three plasmids have similar effects on cell proliferation. Consistent with our results, other side effects of nucleofection have been recently reported. Anderson *et al.* (2013) found that nucleofection induces transient Eif2α (eukaryotic initiation factor 2-α subunit) phosphorylation, which results in a general decrease in translation initiation events. Another group (Mello de Queiroz *et al.*, 2012) reported a cell type-dependent increase in the metabolic rate of cells after nucleofection. Therefore, special consideration and additional controls must be taken into account when using transfection for studies of cell responses.

Taken together, all our data and previous reports suggest that the method of transfection, the nature of the DNA, and also transfected cell types determine the degree of the immunoresponse induced. Therefore, neither a specific method nor methylation of DNA can guarantee weak IFN responses and should be assessed for each specific experimental setting.

Concerning the particular set of plasmids used in this study, we should point out that when using the gateway system for cloning by replacement of a part of the vector sequences with genes of interest, the preferable control would be expression vectors with mutated ATG of inserted genes rather than the original destination vector to avoid misleading results.

We observed activation of the DDR pathway, which is a network that detects and repairs DNA breaks. How is the activation of this pathway in the context of transfection induced? There are two possible explanations: (1) transfected DNA is sensed as broken DNA and activates the response as suggested in Wake *et al.* (1984) or (2) DDR activation may be connected with IFN production. It has been described that the production of reactive oxygen species (ROS) induces DNA double-stranded breaks during the IFN response (Moiseeva *et al.*, 2006). In fact, we detected high levels of ROS at 5 h postnucleofection (data not shown). In addition, it was recently described that macrophages exposed to γ-radiation concomitant with DDR activation undergo a type I IFN response indicating crosstalk between these two pathways (Mboko *et al.*, 2012). However, how IFN is connected with DDR is not understood. The responses to transfection of DNA could be a good model for studying this process.

Acknowledgments

This work was generously supported by the Grant Agency of the Czech Republic GACR, no. P304/10/1511 (B.R.), by the project of the Ministry of Education, Youth and Sports of Czech Republic, MSM0021620858 (J.F.) and SVV-2013-267205 (S.H.).

Disclosure Statement

No competing financial interest exists.

References

Anderson, B.R., Karikó, K., and Weissman, D. (2013). Nucleofection induces transient eIF2α phosphorylation by GCN2 and PERK. Gene Ther **20,** 136–142.

Assaf, A., Esteves, H., Curnow, S.J., and Browning, M.J. (2009). A threshold level of TLR9 mRNA predicts cellular responsiveness to CpG-ODN in haematological and non-haematological tumour cell lines. Cell Immunol **259,** 90–99.

Baeuerle, P., and Baltimore, D. (1988). IkB: a specific inhibitor of the NF-kB transcription factor. Science **242,** 540–546.

Bauer, S., Kirschning, C.J., Häcker, H., Redecke, V., Hausmann, S., Akira, S., Wagner, H., and Lipford, G.B. (2001). Human TLR9 confers responsiveness to bacterial DNA via

species-specific CpG motif recognition. Proc Natl Acad Sci U S A **98,** 9237–9242.

Bourke, E., Bosisio, D., Golay, J., Polentarutti, N., and Mantovani, A. (2003). The toll-like receptor repertoire of human B lymphocytes: inducible and selective expression of TLR9 and TLR10 in normal and transformed cells. Blood **102,** 956–963.

Buck, C.B., Day, P.M., Thompson, C.D., Lubkowski, J., Lu, W., Lowy, D.R., and Schiller, J.T. (2006). Human alpha-defensins block papillomavirus infection. Proc Natl Acad Sci U S A **103,** 1516–1521.

Contreras, J., Hsueh, P.Y., Pei, H., and Hamm-Alvarez, S.F. (2012). Use of nucleofection to efficiently transfect primary rabbit lacrimal gland acinar cells. Cytotechnology **64,** 149–156.

Dalpke, A., Frank, J., Peter, M., and Heeg, K. (2006). Activation of Toll-like receptor 9 by DNA from different bacterial species. Infect Immun **74,** 940–946.

Di, J.M., Pang, J., Pu, X.Y., Zhang, Y., Liu, X.P., Fang, Y.Q., Ruan, X.X., and Gao, X. (2009). Toll-like receptor 9 agonists promote IL-8 and TGF-beta1 production via activation of nuclear factor kappaB in PC-3 cells. Cancer Genet Cytogenet **192,** 60–67.

Ewaschuk, J.B., Backer, J.L., Churchill, T.A., Obermeier, F., Krause, D.O., and Madsen, K.L. (2007). Surface expression of Toll-like receptor 9 is upregulated on intestinal epithelial cells in response to pathogenic bacterial DNA. Infect Immun **75,** 2572–2579.

Ferguson, B.J., Mansur, D.S., Peters, N.E., Ren, H., and Smith, G.L. (2012). DNA-PK is a DNA sensor for IRF-3-dependent innate immunity. Elife **1,** e00047.

García, M.A., Gil, J., Ventoso, I., Guerra, S., Domingo, E., Rivas, C., and Esteban, M. (2006). Impact of protein kinase PKR in cell biology: from antiviral to antiproliferative action. Microbiol Mol Biol Rev **70,** 1032–1060.

Gardiner-Garden, M., and Frommer, M. (1987). CpG islands in vertebrate genomes. J Mol Biol **196,** 261–282.

Gresch, O., Engel, F.B., Nesic, D., Tran, T.T., England, H.M., Hickman, E.S., Körner, I., Gan, L., Chen, S., Castro-Obregon, S., Hammermann, R., Wolf, J., Müller-Hartmann, H., Nix, M., Siebenkotten, G., Kraus, G., and Lun, K. (2004). New non-viral method for gene transfer into primary cells. Methods **33,** 151–163.

Hemmi, H., Takeuchi, O., Kawai, T., Kaisho, T., Sato, S., Sanjo, H., Matsumoto, M., Hoshino, K., Wagner, H., Takeda, K., and Akira, S. (2000). A Toll-like receptor recognizes bacterial DNA. Nature **408,** 740–745.

Hornung, V., Ablasser, A., Charrel-Dennis, M., Bauernfeind, F., Horvath, G., Caffrey D.R., Latz, E., and Fitzgerald, K. (2009). AAIM2 recognizes cytosolic dsDNA and forms a caspase-1-activating inflammasome with ASC. Nature **458,** 514–518.

Huerfano, S., Zíla, V., Boura, E., Spanielová, H., Stokrová, J., and Forstová, J. (2010). Minor capsid proteins of mouse polyomavirus are inducers of apoptosis when produced individually but are only moderate contributors to cell death during the late phase of viral infection. FEBS J **277,** 1270–1283.

Ishikawa, H., Ma, Z., and Barber, G.N. (2009). STING regulates intracellular DNA-mediated, type I interferon-dependent innate immunity. Nature **461,** 788–792.

Keating, S.E., Baran, M., and Bowie, A.G. (2011). Cytosolic DNA sensors regulating type I interferon induction. Trends Immunol **32,**574–581.

Kim, T., Pazhoor, S., Bao, M., Zhang, Z., Hanabuchi, S., Facchinetti, V., Bover, L., Plumas, J., Chaperot, L., Qin, J., and Liu, Y.J. (2010). Aspartate-glutamate-alanine-histidine box motif (DEAH)/RNA helicase A helicases sense microbial DNA in human plasmacytoid dendritic cells. Proc Natl Acad Sci U S A **107,** 15181–15186.

Krieg, A.M., Yi, A.K., Matson, S., Waldschmidt, T.J., Bishop, G.A., Teasdale, R., Koretzky, G.A., and Klinman, D.M. (1995). CpG motifs in bacterial DNA trigger direct B-cell activation. Nature **374,** 546–549.

Larsen, F., Gundersen, G., Lopez, R., and Prydz, H. (1992). CpG islands as markers in the human genome. Genomics **13,** 1095–1107.

Legendre, J.Y., and Szoka, F.C., Jr. (1992). Delivery of plasmid DNA into mammalian cell lines using pH-sensitive liposomes: comparison with cationic liposomes. Pharm Res **10,** 1235–1242.

Li, A., Eirín-López, J.M., and Ausió, J. (2005). H2AX: tailoring histone H2A for chromatin-dependent genomic integrity. Biochem Cell Biol **83,** 505–515.

Li, J., Ma, Z., Tang, Z.L., Stevens, T., Pitt, B., and Li, S. (2004). CpG DNA-mediated immune response in pulmonary endothelial cells. Am J Physiol Lung Cell Mol Physiol. **287,** L552–L558.

Lin, R., Heylbroeck, C., Pitha, P.M., and Hiscott, J. (1998). Virus-dependent phosphorylation of the IRF-3 transcription factor regulates nuclear translocation, transactivation potential, and proteasome-mediated degradation. Mol Cell Biol **5,** 2986–2996.

Maurisse, R., De Semir, D., Emmamekhoo, H., Bedayat, B., Abdolmohammadi, A, Parsi, H., and Gruenert, D. (2010). Comparative transfection of DNA into primary and transformed mammalian cells from different lineages. BMC Biotechnol. **10,** 9.

Mboko, W.P., Mounce, B.C., Wood, B.M., Kulinski, J.M., Corbett, J.A., and Tarakanova, V.L. (2012). Coordinate regulation of DNA damage and type I interferon responses imposes an antiviral state that attenuates mouse gammaherpesvirus type 68 replication in primary macrophages. J Virol **86,** 6899–6912.

Mello de Queiroz, F., Sánchez, A., Agarwal, J.R., Stühmer, W., and Pardo, L.A. (2012). Nucleofectioninduces non-specific changes in the metabolic activity of transfected cells. Mol Biol Rep **39,** 2187–2194.

Moiseeva, O., Mallette, F.A., Mukhopadhyay, U.K., Moores, A., and Ferbeyre, G. (2006). DNA damage signaling and p53-dependent Senescence after prologed interferon-β stimulation. Mol Bio Cell **17,** 1583–1592.

Nguyen, J., and Szoka, F.C. (2012). Nucleic acid delivery: the missing pieces of the puzzle? Acc Chem Res **45,** 1153–1162.

Pestka, S., Krause, C.D., and Walter, M.R. (2004). Interferons, interferon-like cytokines, and their receptors. Immunol Rev **202,** 8–32.

Pindel, A., and Sadler, A. (2010). The role of protein kinase R in the interferon response. J Interferon Cytokine Res **31,** 59–70.

Pitha, P.M., and Kunzi, M.S. (2007). Type I interferon: the ever unfolding story. Curr Top Microbiol Immunol **316,** 41–70.

Platanias, L.C. (2005). Mechanisms of type I and type II interferon mediated signalling. Nat Rev Immunol **5,** 375–386.

Platz, J., Beisswenger, C., Dalpke, A., Koczulla, R., Pinkenburg, O., Vogelmeier, C., and Bals, R. (2004). Microbial DNA induces a host defense reaction of human respiratory epithelial cells. J Immunol **173,** 1219.

Rautsi, O., Lehmusvaara, S., Salonen, T., Häkkinen, K., Sillanpää, M., Hakkarainen, T., Heikkinen, S., Vähäkangas, E., Ylä-Herttuala, S., Hinkkanen, A., Julkunen, I., Wahlfors, J., and Pellinen, R. (2007). Type I interferon response against viral and non-viral gene transfer in human tumor and primary cell lines. J Gene Med **9,** 122–135.

Rosazza, C., Escoffre, J.M., Zumbusch, A., and Rols, M.P. (2011). The actin cytoskeleton has an active role in the electrotransfer of plasmid DNA in mammalian cells. Mol Ther **19,** 913–921.

Sharma, S., and Fitzgerald, K.A. (2011). Innate immune sensing of DNA. PLoS Pathog **7,** e1001310.

Stetson, D.B., and Medzhitov, R. (2006). Type I interferons in host defense. Immunity **25,** 373–381.

Takaoka, A., Wang, Z., Choi, M.K., Yanai, H., Negishi, H., Ban, T., Lu, Y., Miyagishi, M., Kodama, T., Honda, K., Ohba, Y., and Taniguchi, T. (2007). DAI (DLM-1/ZBP1) is a cytosolic DNA sensor and an activator of innate immune response. Nature **448,** 501–505.

Takeshita, F., Leifer, C.A, Gursel, I., Ishii, K.J., Takeshita, S., Gursel, M., and Klinman, D.M. (2001). Cutting edge: role of Toll-like receptor 9 in CpG DNA-induced activation of human cells. J Immunol **167,** 3555–3558.

Tolstov, Y.L., Pastrana, D.V., Feng, H., Becker, J.C., Jenkins, F.J., Moschos, S., Chang, Y., Buck, C.B., and Moore, P.S. (2009). Human Merkel cell polyomavirus infection II. MCV is a common human infection that can be detected by conformational capsid epitope immunoassays. Int J Cancer **125,** 1250–1256.

Unterholzner, L., Keating, S.E., Baran, M., Horan, K.A., Jensen, S.B., Sharma, S., Sirois, C.M., Jin, T., Latz, E., Xiao, T.S., Fitzgerald, K.A., Paludan, S.R., and Bowie, A.G. (2010). IFI16 is an innate immune sensor for intracellular DNA. Nat Immunol **11,** 997–1004.

Vasilkoski, Z., Esser, A.T., Gowrishankar, T.R., and Weaver, J.C. (2006). Membrane electroporation: the absolute rate equation and nanosecond time scale pore creation. Phys Rev E Stat Nonlin Soft Matter Phys **74,** 21904–21916.

Wake, C.T., Gudewicz, T., Porter, T., White, A., and Wilson, J.H. (1984). How damaged is the biologically active subpopulation of transfected DNA? Mol Cell Biol **3,** 387–398.

Weiner, G.J. (2000). The immunobiology and clinical potential of immunostimulatory CpG oligodeoxynucleotides.J. Leukocyte Biol **68,** 455–463.

Yang, P., An, H., Liu, X., Wen, M., Zheng, Y., Rui, Y., and Cao, X. (2010). The cytosolic nucleic acid sensor LRRFIP1 mediates the production of type I interferon via a beta-catenin-dependent pathway. Nat Immunol **11,** 487–494.

Yasuda, K., Yamane, I., Nishikawa, M., and Takakura, Y. (2005). Macrophage activation by a DNA/cationic liposome complex requires endosomal acidification and TLR9-dependent and independent pathways. J Leukoc Biol **77,** 71–79.

Yoshinaga, T., Yasuda, K., Ogawa, Y., Nishikawa, M., and Takakura, Y. (2006). DNA and its cationic lipid complexes induce CpG motif-dependent activation of murine dendritic cells. Immunology **120,** 295–302.

Zhang, X., Brann, T.W., Zhou, M., Yang, J., Oguariri, R.M., Lidie, K.B., Imamichi, H., Huang, D.W., Lempicki, R.A., Baseler, M.W., Veenstra, T.D., and Young, H.A., Lane, H.C., and Imamichi, T. (2011a). Cutting edge: Ku70 is a novel cytosolic DNA sensor that induces type III rather than type I IFN. J Immunol **186,** 4541–4545.

Zhang, Z., Yuan, B., Bao, M., Lu, N., Kim, T., and Liu, Y.J. (2011b). The helicase DDX41 senses intracellular DNA mediated by the adaptor STING in dendritic cells. Nat Immunol **12,** 959–965.

Address correspondence to:
Jitka Forstová, PhD
Department of Genetics and Microbiology
Charles University in Praque
Viničná 5
12844 Prague 2
Czech Republic

E-mail: jitka.forstova@natur.cuni.cz

Received for publication December 19, 2012; received in revised form April 25, 2013; accepted May 7, 2013.

The FEBS Journal

FEBS PRESS science publishing by scientists

EDITOR'S CHOICE

Hydrophobic domains of mouse polyomavirus minor capsid proteins promote membrane association and virus exit from the ER

Sandra Huérfano, Boris Ryabchenko, Hana Španielová and Jitka Forstová

Department of Genetics and Microbiology, Charles University in Prague, Czech Republic

Keywords
hydrophobic domains; MPyV; VP2; VP3

Correspondence
J. Forstová, Faculty of Science, Charles University, Department of Genetics and Microbiology, Viničná 5, 128 44 Prague 2, Czech Republic
Fax: +420 221 951 729
Tel: +420 221 951 730
E-mail: jitkaf@natur.cuni.cz

(Received 8 August 2016, revised 19 December 2016, accepted 31 January 2017)

doi:10.1111/febs.14033

The minor structural protein VP2 and its shorter variant, VP3, of mouse polyomavirus (MPyV) are essential for virus exit from the endoplasmic reticulum (ER) during viral trafficking to the nucleus. Here, we followed the role of putative hydrophobic domains (HD) of the minor proteins in membrane affinity and viral infectivity. We prepared variants of VP2, each mutated to decrease hydrophobicity of one of three predicted hydrophobic domains: VP2-mHD1, VP2-mHD2 or VP2-mHD3 mutated in HD1 (amino acids (aa) 60–101), HD2 (aa 125–165) or HD3 (aa 287–307), respectively. Transient production of the mutated proteins revealed that only VP2-mHD2 lost the affinity for intracellular membranes. Cytotoxicity connected with the ability of VP2/VP3 to perforate membranes decreased markedly for VP2-mHD2, but only slightly for VP2-mHD1. The mutant VP2-mHD3 exhibited properties similar to the wild-type protein. MPyV genomes, each carrying one of the mutations, were prepared for virus production. MPyV-mHD1 and MPyV-mHD2 viruses could be isolated, while the HD3 mutation in VP2/VP3 prevented virus assembly. We found that both MPyV-mHD1 and MPyV-mHD2 viruses arrived at the ER without delay and were processed by ER residential enzymes. However, the ability to associate with ER membranes was decreased in the case of MPyV-mHD1 and practically abolished in the case of MPyV-mHD2. Interestingly, while MPyV-mHD2 was not infectious, infection of MPyV-mHD1 virus was delayed. These findings reveal that HD2, common to both VP2 and VP3, is responsible for the membrane binding properties of the minor proteins, while HD1 of VP2 is likely required to stabilize VP2–membrane association and to enhance viral exit from the ER.

Introduction

Mouse polyomavirus (MPyV) belongs to the *Polyomaviridae* family, a group of non-enveloped DNA tumorigenic viruses. In common with other non-enveloped viruses, penetration of intracellular membranes is a crucial step for the delivery of the genome into the nucleus. However, to date, our understanding of the polyomavirus membrane penetration process is still incomplete. Non-enveloped viruses use diverse and sophisticated mechanisms to cross host membranes. For example, human adenovirus 2 is internalized into

Abbreviations
aa, amino acids; B12, DNAJB12; B14, DNAJB14; DAPI, 4′,6′-diamidino-2-phenylindole; EGFP, enhanced green fluorescent protein; ER, endoplasmic reticulum; GAPDH, glyceraldehyde 3-phosphate dehydrogenase; HD, hydrophobic domain; hpi, hours post-infection; LDH, lactate dehydrogenase; LT, large tumour; MPEX, membrane protein explorer; MPyV, mouse polyomavirus; NLS, nuclear localization signal; PDI, protein disulfide isomerase; PLA, proximity ligation assay; WT, wild-type.

clathrin-coated vesicles after binding to the coxsackievirus adenovirus receptor and αvβ1 integrin coreceptor. These interactions give rise to conformation changes that support fibre shedding from the viral particle in the endosome, leading to exposure of the membrane-lytic internal virion protein VI, which mediates escape of the virus from the endosome [1].

Papillomaviruses enter cells by clathrin coated vesicle-mediated endocytosis after attachment to the plasma membrane. At low endosomal pH, virions are partially disassembled and the minor capsid protein, L2, is cleaved by furin, a cell-encoded proprotein convertase. L2 cleaved at its N terminus then mediates either escape from endosomes [2] or sorting of the virus to the *trans*-Golgi network [3]. Recent studies have provided evidence that papillomaviruses require nuclear envelope breakdown during mitosis for delivery of their genomes into the nucleus [4].

Polyomaviruses are internalized, after binding to their receptor, into smooth tightly fitting vesicles. On the productive pathway, the viruses pass through early and late endosomal compartments. Low endosomal pH is required for virus infectivity. The virus is further sorted into the endoplasmic reticulum (ER) prior to nuclear entry [5–7]. Although some changes have been observed in protease sensitivity of viral capsids after binding to the receptor and exposure to low pH [7,8], the most significant changes are known to occur in the ER. Trafficking of the particles from late endosomal compartments to ER and from ER to the cell nucleus is still not well understood. Evidence for the importance of residential ER chaperones and enzymes in viral infectivity strongly supports the hypothesis that polyomaviruses penetrate the membrane at the ER [9–13].

Intact MPyV capsids (45 nm in diameter) have icosahedral symmetry and are composed of 360 copies of the major capsid protein, VP1, and 72 molecules of either VP2 or VP3, the minor capsid proteins. They are arranged such that five molecules of VP1 assemble into each of 72 stable ring-shaped capsomeres, with interpentameric contacts being established by the flexible C-terminal chains of the VP1 molecules [14,15]. Capsomere contacts are stabilized by calcium ions and disulfide bridges [16]. Only one molecule of either VP2 or VP3, which is a shorter variant of VP2 lacking first 116 N-terminal amino acids, is located in the inner site of the central cavity of the VP1 capsomere. Thus, neither VP2 nor VP3 is exposed at the surface of the intact capsids [17,18].

In the lumen of the ER, the virus undergoes rearrangements that involve the reduction and/or isomerization of disulfide bonds due to the activity of protein disulfide isomerase (PDI). For MPyV, isomerases ERp57, PDI and ER29 were found to be required [10], while for BK and SV40 polyomaviruses, ERdj5, PDI and ERp57 were found to mediate conformational changes [11,13]. These conformational changes in the ER lead to the exposure of the minor proteins to the intracellular environment and alterations of the capsid structure, although the overall spherical morphology of the virion is preserved. The changes result in protrusions from the virus particle and the appearance of particle angularity [13,19,20]. Several studies support the essential role of the minor proteins, VP2 and VP3, for polyomavirus infectivity in the very early phase of infection [21–23]. Studying VP2 and VP3 function, we and others have demonstrated their viroporin-like properties. They bind and perforate host cell membranes [24] or microsomes [25].

Although the 3D crystallographic structures of the minor proteins of polyomaviruses have not been solved (because of the insolubility or hydrophobicity of the proteins, preventing crystal formation), for MPyV VP2, a short C-terminal peptide (residues 214–318) was crystalized in complex with VP1 capsomeres. Residues 269–296 were shown to form an α-helix. The hydrophobic helix was shown to be responsible for interactions of VP2 and VP3 with VP1 pentamers [18]. In addition, computer analysis and circular dichroism spectroscopy of MPyV VP2 and VP3 have revealed that both proteins are highly hydrophobic with a high α-helical content [25,26]. In agreement, the viroporins described so far are proteins that contain one or several α-helices that work as transmembrane domains [27].

To date, there are only studies on SV40 regarding the role of the hydrophobic regions of the minor structural proteins, where three protein domains with membrane affinity, essential for virus infectivity, were characterized for VP2 [28]. Apart from hydrophobicity it has been proposed that the N-terminal negatively charged glutamic acid residue in position 17 of VP2 protein of SV40 polyomavirus is important for virus association with ER translocon proteins, Bap31 and J chaperones DNAJB14 (B14) or DNAJB12 (B12) [20,29]. The authors suggest that virus association with the translocon could promote viral exit from ER to the cytosol. Glutamic acid residues at the very N terminus of VP2 are present in all polyomaviruses [20].

There are significant differences in the sequences of the minor capsid proteins of the polyomaviruses [18]. Therefore, molecular mechanisms of interactions of minor proteins with membranes and their role in virus escape into the cytosol can differ for individual members of *Polyomaviridae* family.

In this study, we created and analysed three variants of MPyV VP2, which were mutated in the predicted hydrophobic domains. We also introduced the mutations into the MPyV genome and prepared mutated viruses. Using a combination of microscopy, infectivity assays and biochemistry, we followed the role of the hydrophobic domains in membrane interactions and viral infection. Based on our results, we propose that hydrophobic domain 2, common for both VP2 and VP3, is responsible for the membrane binding properties of the MPyV minor proteins, while HD1, present only in VP2, is required after membrane binding of VP2 for another interaction to enhance virus exit from the ER.

Results

One of three predicted hydrophobic domains of the minor capsid protein VP2 displays very strong affinity for cell membranes

As MPyV VP2 is the longer variant (319 aa) of the two minor capsid proteins, and the VP3 sequence is identical with the C-terminal 203 amino acids of VP2, we analysed the hydrophobicity of the sequence of MPyV VP2 protein to define hydrophobic domains (HD) of VP2 and VP3 using four software programs. Each of the programs uses different features to determine membrane spanning regions. The membrane protein explorer program (MPEX) uses the experimentally defined Wimley–White whole-residue hydrophobicity scale and biological partitioning scale (octanol scale). The octanol scale measures the partitioning of hydrophobic α-helices into the bilayer interior; thus the program takes in account thermodynamic and biological properties of amino acids [30]. The PRED-TMR program uses an algorithm that relies solely on information given by the sequence itself. The algorithm is based on a modified Sipos–von Heijne [31] scale. In addition, the algorithm combines a standard hydrophobicity analysis with a detection of potential termini (starts and ends) of transmembrane regions [32]. The TMPRED program uses algorithms based on the statistical analysis of a database of naturally occurring transmembrane proteins [33]. Finally, the HMMTOP program is based on the hypothesis that the localizations of the transmembrane segments and the topology are determined by the differences in the amino acid distributions in various structural elements of the proteins rather than by specific amino acid compositions of the analysed sequence [34]. A summary of the results obtained by the all programs used is presented in Fig. 1A. A consensus of the amino acid range of the predicted hydrophobic domains is given at the bottom of the table in Fig 1A. In total, three domains were predicted, hydrophobic domain 1 (HD1) from amino acids 60–101, hydrophobic domain 2 (HD2) from amino acids 126–165 and hydrophobic domain 3 (HD3) from amino acids 287–307. From the three domains only HD2 and HD3 are present in the VP3 sequence (VP3 starts from aa 116). It was noted that HD2 was detected only by the program MPEX which, as detailed above, considers thermodynamic and biological properties of amino acids. The plot generated by MPEX is presented in Fig. 1B. The HD domains predicted are marked by red lines and the consensus sequences from all programs are marked by blue lines.

Three mutated variants of VP2 were then prepared, each with decreased hydrophobicity in a single one of the three domains. Since the addition of charged

A

Program	HD domains (aa position)		
	1	2	3
MPEx	69–101	126–165	287–305
Pred -TMR	–	–	287–307
TMpred	60–100	–	287–307 *
HMMTOP	81–100	–	288–307
Consensus	**60–101**	**126–165**	**287–307**

B

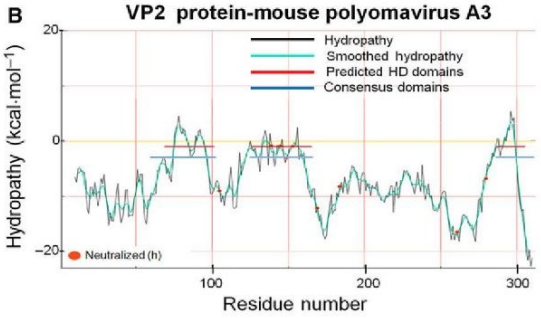

Fig. 1. Hydrophobic domains of MPyV VP2 minor capsid protein. (A) The sequence of VP2 protein of the mouse polyoma virus A3 strain was analysed using software programs as detailed in 'Results'. Predicted hydrophobic domains were annotated according to their position in the protein. (B) Hydropathy plot of VP2 sequence when analysed by the MPEX program. The black curve is the actual profile; the superimposed green curve is a smoothed version of the profile. Hydrophobic domains predicted by MPEX are marked by red lines while the consensus derived from all the program data is marked by blue lines. MPEX assumes a pH of the environment of 7. The default state of histidine (h) is thus neutral, the positions of these residues in the sequence being indicated on the graph by an orange spot. *Score slightly above the cutoff.

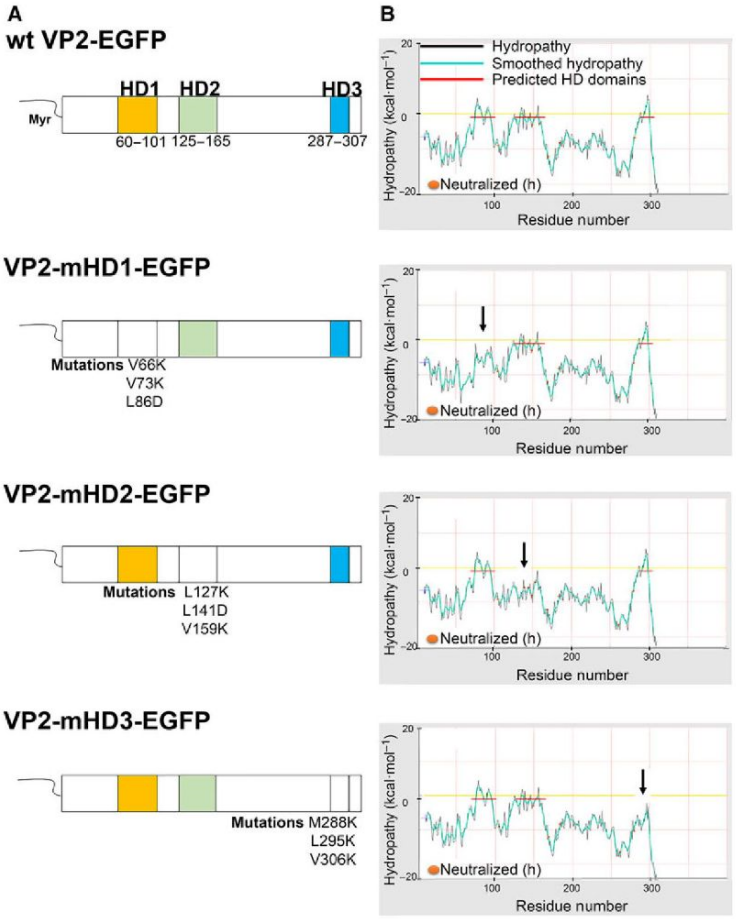

Fig. 2. Design of substitution mutants. (A) Schematic diagram of WT VP2-EGFP protein and mutants VP2-mHD1-EGFP, VP2-mHD2-EGFP and VP2-mHD3-EGFP, each mutated in one of three hydrophobic domains (HD1, orange; HD2, green; HD3, blue; the boundaries of each are given as amino acid position in the relevant protein) to decrease their hydrophobicity. Amino acid substitutions are indicated below the respective mutants. EGFP sequence fused to the C terminus of VP2 is not shown. (B) The hydrophobicity plots generated by the MPEX program for each mutant and WT (for comparison) are displayed. The black curve is the actual profile; the superimposed green curve is a smoothed version of the profile. Hydrophobic domains predicted are marked by red lines. MPEX assumes the pH of environment = 7. The default state of histidine (h) is thus neutral, the positions of these residues in the sequence being indicated on the graph by an orange spot.

amino acids has been shown to efficiently disrupt hydrophobicity of transmembrane domains [28,35], each of the hydrophobic domains was mutated by replacement of three selected hydrophobic amino acids with charged hydrophilic ones: valine (V) with lysine (K), leucine (L) with aspartic acid (D), or leucine and methionine (M) with lysine. This approach is in agreement with studies of topology of membrane proteins that reveal that charged residues are often present in sequences flanking their hydrophobic transmembrane domains, while in the transmembrane domains, they are under-represented [36]. This applies to VP2 of MPyV too. Thus, putative hydrophobic domains are intended to function as flanking regions, once the mutations are introduced.

Mutated protein variants were subjected to analysis using the above-described programs to confirm the decrease of the hydrophobicity of mutated domains. A similar analyses of replacements of hydrophobic amino acids by alanine or polar amino acids (serine, glutamine, asparagine) showed inconsistent and/or insignificant decrease of hydrophobicity in the domains 1 or 3. Therefore, these types of substitutions were not performed for the study.

We prepared the mutated genes by using the plasmid VP2-EGFP-N1 [24] (containing the VP2 gene

Fig. 3. Affinity of VP2-EGFP protein or its mutants, VP2-mHD1-EGFP, VP2-mHD2-EGFP or VP2-mHD3-EGFP, for ER membranes. Mouse NIH3T3 fibroblasts were transfected by nucleofection and processed 4.5 h post-infection. Confocal microscopy analysis was performed by fixing cells and staining with antibody against ER markers (red): (A) ER luminal BiP chaperone; (B) ER membrane protein B14. The minor structural proteins were re-stained with anti-VP2/3 IgG (green). DNA was stained by 4′,6′-diamidino-2-phenylindole (DAPI). Representative confocal sections are presented. Bars: 5 μm.

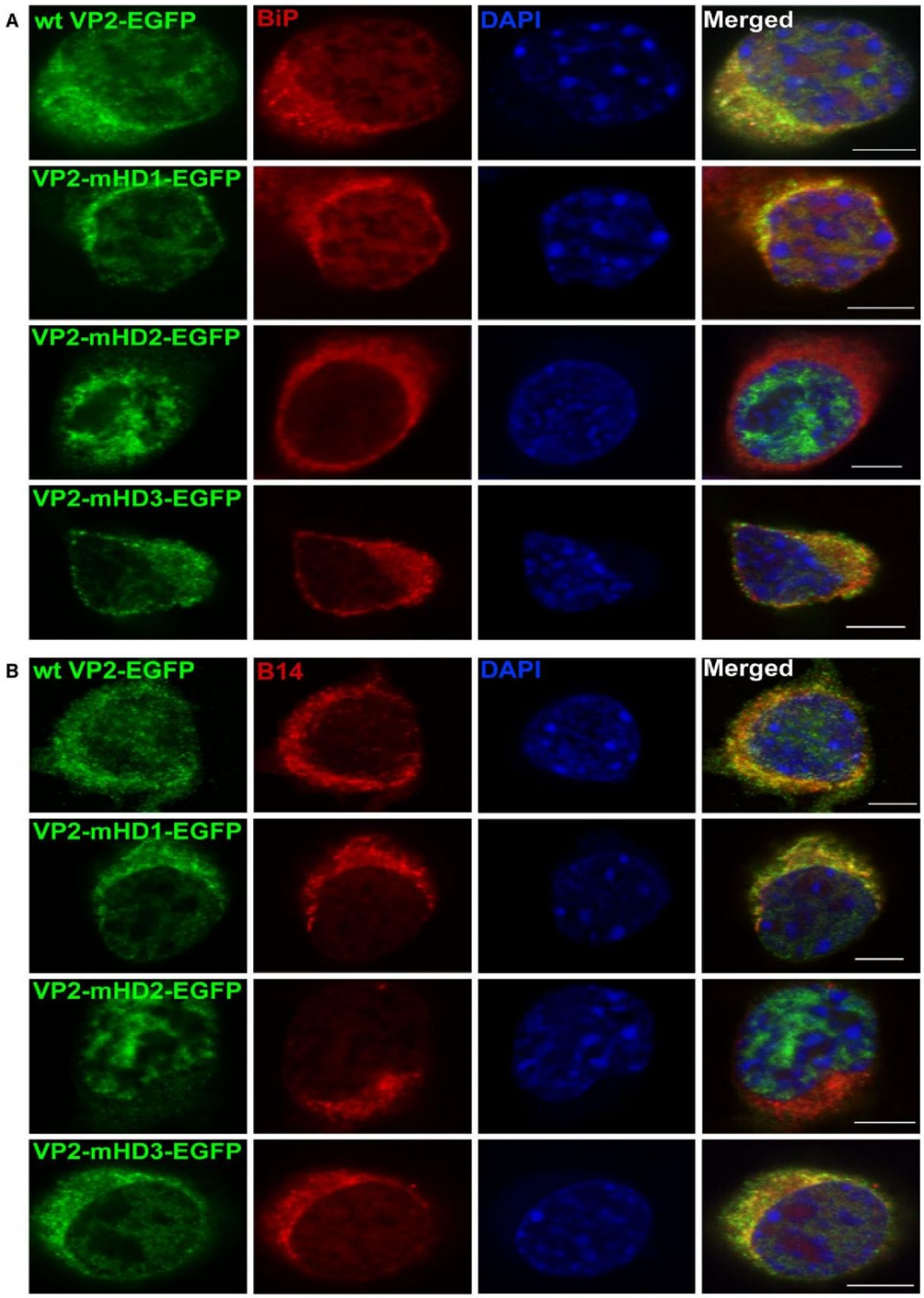
A
wt VP2-EGFP
BiP
DAPI
Merged
VP2-mHD1-EGFP
VP2-mHD2-EGFP
VP2-mHD3-EGFP
B
wt VP2-EGFP
B14
DAPI
Merged
VP2-mHD1-EGFP
VP2-mHD2-EGFP
VP2-mHD3-EGFP

from MPyV A3 strain, fused with enhanced green fluorescent protein (EGFP) sequences) as a template. The mutations introduced into the individual domains are shown in Fig. 2. The hydrophobicity plots obtained by MPEX for each mutant are also presented.

To analyse how the introduced mutations affected the membrane binding of VP2, we performed confocal fluorescence microscopy and cell fractionation. To identify ER, first we used antibodies against BiP, a resident chaperone in the ER, as well as an antibody against the ER membrane protein B14, for confocal microscopy colocalization studies. Then we followed localization of wild-type (WT) VP2-EGFP and VP2 mutants in transfected fibroblasts. In agreement with our results published earlier [24], WT VP2 was present in the nucleus and also in the cytosol, colocalizing there with both BiP and B14 (Fig. 3A,B, respectively). VP2-mHD1-EGFP and VP2-mHD3-EGFP mutant proteins displayed similar behaviour to WT VP2, being associated with intracellular membranes. In contrast, the mutated protein with decreased hydrophobicity in HD2 (VP2-mHD2-EGFP) localized in the cell nucleus or cytosol but it lost affinity for the membranes. Next, cells were analysed by western blotting to determine the distribution of WT VP2 or VP2 mutant variants in the various fractions. As shown in Fig. 4A, we routinely observed that the protein mutated in the hydrophobic domain 2 (VP2-mHD2-EGFP) was present in the nuclear and cytosolic fractions but its presence in the membrane fraction was negligible. The other mutants (VP2-mHD1-EGFP and VP2-mHD3-EGFP) were distributed in all fractions, membrane, nuclear and cytosolic, similar to WT protein. To analyse of the fractionation data further, optical densities corresponding to the intensities of VP2 proteins were quantified. The percentage of total WT or mutated VP2 proteins in the respective membrane fraction is presented in Fig. 4B. While the proportion of membrane-bound VP2-mHD1-EGFP (20–22%) and VP2-mHD3-EGFP (19–27%) was comparable with that of WT VP2-EGFP protein (18–21%), only 0–3% of the protein mutated in HD2 (VP2-mHD2-EGFP) was detected in the membrane fraction.

To confirm the role of the putative hydrophobic domain 2 of VP2 in membrane binding, we prepared three short versions of VP2 protein (fused to EGFP), deleting large amino acid stretches in such a way that each VP2 variant contained only one intact hydrophobic domain. The predicted loss of hydrophobicity by deletions was consistent with analysis using the MPEX software. Deletion mutants were prepared using plasmids VP2- or VP3-EGFP-N1. In

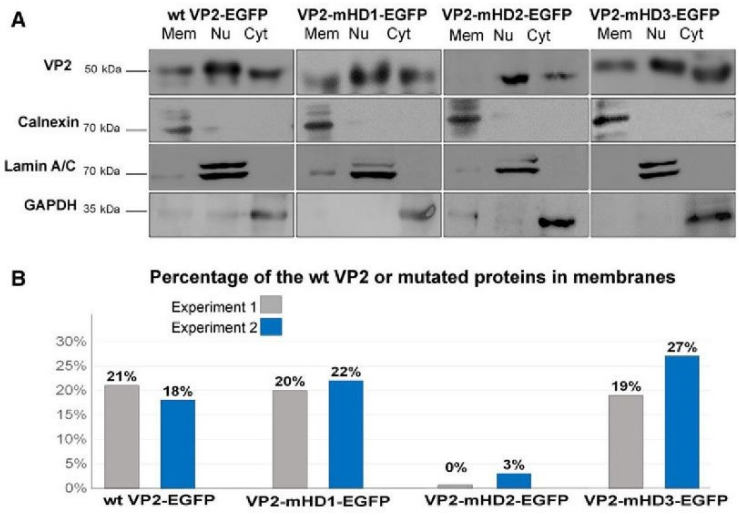

Fig. 4. Affinity of VP2-EGFP protein or its mutants, VP2-mHD1-EGFP, VP2-mHD2-EGFP or VP2-mHD3-EGFP, for cellular membranes analysed by cell fractionation. Mouse NIH3T3 fibroblasts were transfected by nucleofection and processed 4.5 h post-infection. (A) Western blot analysis of cell fractions. Cells were fractionated into membrane (Mem), nuclear (Nu) and cytosolic (Cyt) fractions and the fractions were analysed by western blotting for the presence of VP2 protein or, as control, fraction markers calnexin, lamin A/C or glyceraldehyde 3-phosphate dehydrogenase (GAPDH), respectively. (B) The relative amounts of VP2 protein or mutated variants in individual fractions were quantified by densitometry. The relative proportions of individual proteins detected in the membrane fractions are compared and expressed as a percentage. Data from two independent experiments are given.

all deleted variants, the nuclear localization signal (NLS) was preserved. A summary scheme of mutant variants is presented in Fig. 5A. Deletion mutants were analysed similarly to the substitution mutants by confocal fluorescence microscopy and by cell fractionation. Confocal microscopy revealed that only the variant carrying intact HD2 still colocalized with ER membranes (Fig. 5B). Both variants carrying HD1 or HD3 lost the ability to bind intracellular membranes and were located in the cell nucleus and, partly, also in the cytosol. Figure 5C shows a representative picture of the western blot of membrane, nuclear and cytosolic fractions of VP2 deletion variants, and Fig. 5D, based on quantification of band densities, shows the proportions of the mutated proteins bound to membranes. In agreement with results obtained by substitution mutant analysis, only domain 2 (HD2) was found abundantly (23 and 37% of total cellular VP2 in two independent experiments) in the membrane fraction, while 0–3% was detected for the protein HD1-EGFP carrying domain 1 only, and 1.5–4% for HD3-EGFP carrying domain 3.

Taken together, it was concluded that domain 2 is a strongly hydrophobic region of the minor capsid proteins, and is responsible for their binding to intracellular membranes.

Loss of hydrophobicity of the minor capsid proteins affected their ability to induce cell death

Previously, we showed in transfected cells producing VP2 that its binding to intracellular membranes leads to cell death [24]. Therefore, we were interested to determine whether cytotoxicity of VP2 substitution mutants would be in agreement with their changed membrane affinity. We transfected cells with EGFP variants WT VP2-EGFP, VP2-mHD1-EGFP, VP2-mHD2-EGFP or VP2-mHD3-EGFP and followed the release of lactate dehydrogenase (LDH) into the cell medium 12 h post-transfection. We found that, in contrast to WT protein, VP2 mutated in the HD1 displayed a slightly reduced ability to induce cell death while the protein with mutated HD2 exhibited markedly reduced cell toxicity that only slightly exceeded that obtained with control plasmid expressing EGFP. By contrast, VP2 mutated in HD3 was still able to kill cells almost as efficiently as WT VP2 (Fig. 6). Altogether, our results indicate that the cytotoxic properties of the mutated VP2s reflect their affinity for intracellular membranes. The results also revealed that the HD2 present in both VP2 and VP3 is responsible for membrane binding and cell death induced by membrane damage.

Genomes carrying mutation in HD1 of VP2 or in HD2 of VP2 and VP3 are able to generate virions

To understand the role of hydrophobic regions of the minor capsid proteins during early steps of infection, we prepared by site-direct mutagenesis MPyV genomes mutated in the hydrophobic domains of VP2/3 gene, as described above (Fig. 2). We used as a template the plasmid pMJG [37], which contains the entire genome of MPyV strain A3, interrupted by *Eco*RI sites in the large tumour (LT) gene. Next, we investigated the ability of mutated genomes to form viral particles. For this, the genomes were excised from the mutated plasmids with *Eco*RI and recircularized with DNA ligase. Mutant or WT genomes were transfected into 3T6 mouse fibroblasts and after 6 days, viruses were isolated. The viruses mutated in HD1, HD2 and HD3 of VP2 were designated MPyV-mHD1, MPyV-mHD2 and MPyV-mHD3, respectively. All three mutated genomes were efficiently transcribed and replicated and capsid proteins could be detected by immunofluorescence (data not shown). However, transfection of the MPyV-mHD3 genome did not result in efficient virion production. Mostly pentamers and only a few viral particles could be isolated. We suggest that mutation at the very C terminus, which is employed in VP1–VP2/VP3 interaction, can affect the assembly and/or stability of the virus. Virions of mutated genomes MPyV-mHD1 and MPyV-mHD2 could be isolated. Nevertheless, the yield of MPyV-mHD2 particles (measured by haemagglutination) from the same amount of transfected DNA was repeatedly two orders lower than that of the WT and MPyV-mHD1 mutant. Isolated virions of MPyV-mHD1 and MPyV-mHD2 mutants were characterized by electron microscopy. Both mutants displayed normal morphology, i.e. icosahedral particles of approximately 50 nm diameter (Fig. 7A). SDS/PAGE of isolated virions of mutated viruses stained by SYPRO® Ruby Protein Gel Stain (Fig. 7B) and western blot analysis with antibody directed against the minor proteins, VP2 and VP3 (Fig. 7C), confirmed the presence of all three structural proteins, which migrated according to their size. Moreover, the presence of cellular histones in mutant virions can be seen in the Fig. 7B, in similar proportions to that of the WT virus.

Infectivity of the mutated viruses is affected

Next, we explored the ability of mutant viruses MPyV-mHD1 and MPyV-mHD2 to infect permissive cells. First, we quantified the numbers of virions by measuring the virus DNA content by qPCR. Then, we infected cells with equal amounts of WT or mutated

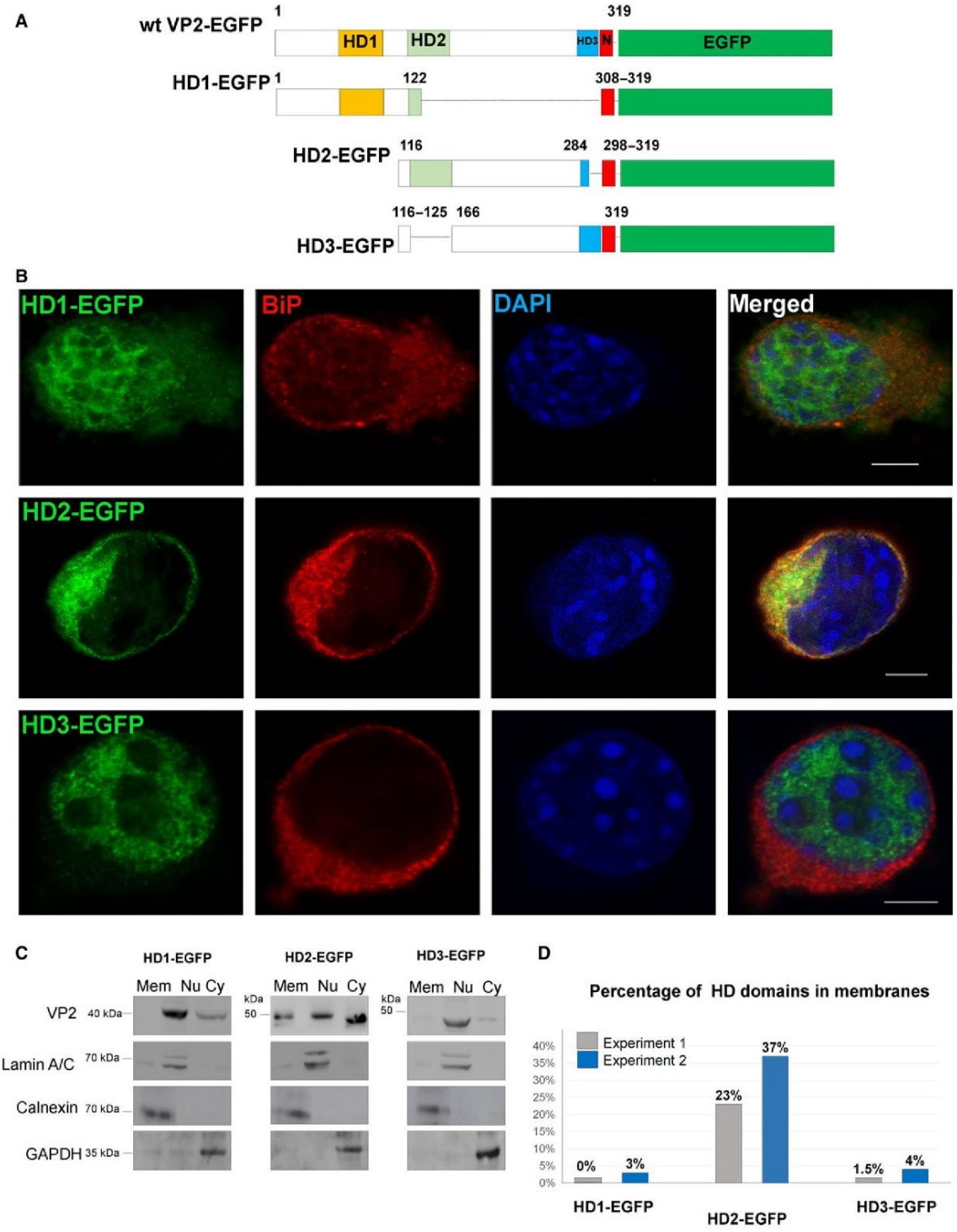
A
wt VP2-EGFP
1
319
HD1
HD2
HD1
N
EGFP
HD1-EGFP
1
122
308–319
HD2-EGFP
116
284
298–319
HD3-EGFP
116–125
166
319
B
HD1-EGFP
BiP
DAPI
Merged
HD2-EGFP
HD3-EGFP
C
HD1-EGFP
HD2-EGFP
HD3-EGFP
Mem Nu Cy
kDa
50
VP2 40 kDa
Lamin A/C 70 kDa
Calnexin 70 kDa
GAPDH 35 kDa
D
Percentage of HD domains in membranes
Experiment 1
Experiment 2
40%
35%
30%
25%
20%
15%
10%
5%
0%
0%
3%
23%
37%
1.5%
4%
HD1-EGFP
HD2-EGFP
HD3-EGFP

Fig. 5. Membrane affinity of VP2-EGFP deletion mutants carrying one of three hydrophobic domains, HD1, HD2 or HD3. (A) Scheme of the deletion mutants. WT VP2-EGFP is presented for comparison. HD1, orange; HD2, light green; HD3, blue; NLS, red; and EGFP, dark green. (B) Confocal microscopy. Mouse 3T3 fibroblasts were transfected with the individual deletion variants using nucleofection, fixed 4.5 h post-transfection and stained with antibody against BiP/ER marker (red); minor structural proteins were re-stained with anti-VP2/3 IgG (green). DNA was stained with DAPI. Representative confocal sections are presented. Bars: 5 μm. (C) Western blot analysis of cell fractions. Membrane, nuclear and cytosol fractions of cells prepared 4.5 h post-transfection were analysed by immunoblotting for the presence of VP2 protein or, as control, fraction markers calnexin, lamin A/C or GAPDH, respectively. (D) Relative amounts of VP2 deletion variants in individual fractions were quantified by densitometry. The relative proportions of individual proteins detected in the membrane fractions are compared and expressed as a percentage. Data from two independent experiments are given.

virus, and 24 h post-infection (hpi), we counted numbers of infected cells by detection of early LT antigen by immunofluorescence. Surprisingly, at this time, almost no infection was detected, not only for the virus mutated in HD2 but also for the virus mutated in HD1. Infection by WT virus led to the expression of LT in approximately 70–80% of the cell population, while LT expression in cells infected with MPyV-mHD1 or MPyV-mHD2 was < 2% (Fig. 8A).

To reveal whether this was due to a delay in the virus infection cycle, we infected cells with mutated viruses as described above and counted LT positive cells 48 and 72 hpi. The results demonstrated a substantial rise of infected cells 72 hpi by the MPyV-mHD1 mutant but not by the virus mutated in domain HD2 (Fig. 8B). In agreement with our previous experiments (Fig. 7A), when cells were transfected with the same amount of mutated genomes, only low yields of MPyV-mHD2 virions were obtained, while abundant amounts of WT virus and MPyV-mHD1 virus were isolated 6 days post-infection (the interval in which reinfection takes place). Together, our data indicate that the MPyV-mHD2 mutant has abolished infectivity while the MPyV-mHD1 mutant virus is markedly delayed in the early phase of the infection cycle.

Mutations on hydrophobic domains affect association of virions with membranes in ER

Previous studies revealed that in the productive pathway, MPyV is sorted through early and late endosomal compartments to the ER [7]. Therefore, we tested whether both mutated viruses could be detected, similar to the WT virus, in ER at early time post-infection. We followed colocalization of mutated viruses within the ER using antibodies against BiP (luminal) or B14 (membrane) protein and against VP1 in a proximity ligation assay (PLA). In this assay, the appearance of

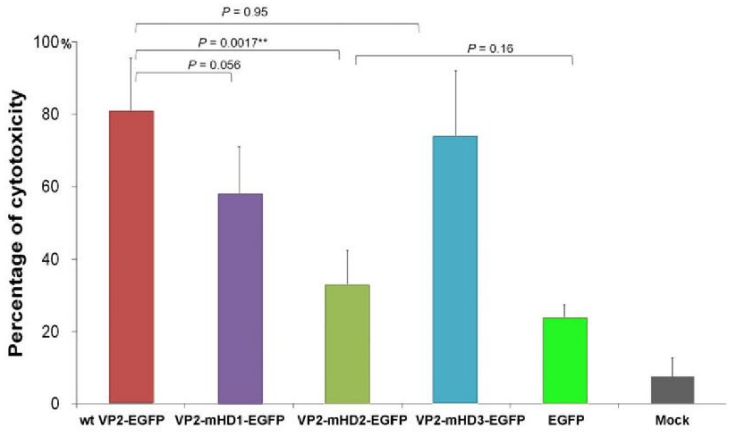

Fig. 6. Cytotoxicity of WT VP2 protein or its mutated variants. Mouse NIH3T3 fibroblasts were transfected with plasmids encoding WT VP2-EGFP or mutants (VP2-mHD1-EGFP, VP2-mHD2-EGFP or VP2-mHD3-EGFP). After transfection, cells were seeded onto 24-well plates and dead or non-adherent cells were removed 3 h post-transfection and incubated in fresh culture medium. At 12 h post-transfection samples were processed to measure the LDH released into the medium. Values are presented relative to that of the LDH release obtained after treatment of cells by Triton X-100. Mock-transfected and EGFP-expressing cells were used as controls. Data in the graph represent mean values ± SD from three experiments. Toxicity of WT *vs.* each mutant or mutant (VP2-mHD2-EGFP) *vs.* EGFP was compared by Student's *t*-test. *P* values are presented and asterisks represent statistically significant differences (**$P \leq 0.01$).

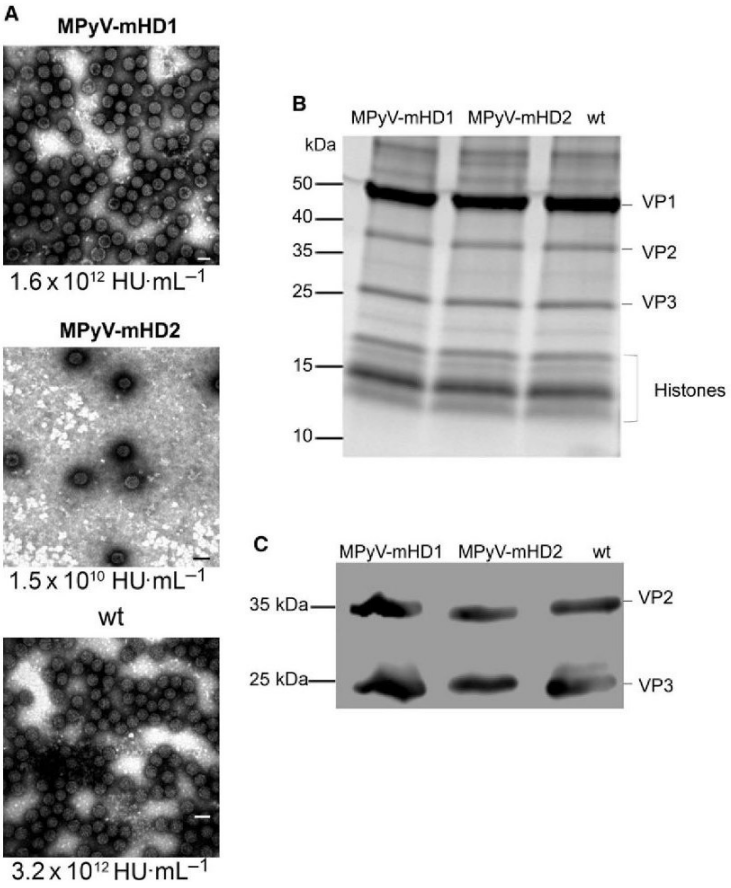

Fig. 7. Characterization of mutant viruses. Mutated MPyV-mHD1, MPyV-mHD2 or WT MPyV genomes were transfected into 3T6 fibroblast, and 6 days post-transfection virions were isolated and purified by CsCl gradient centrifugation. (A) Electron microscopy (negative staining) pictures of virus preparations; the haemagglutination titre of each viral fraction is presented at the bottom of each picture (haemagglutination units (HU)·ml^{-1}). (B) The same number of particles of each virus were denatured and separated by SDS/PAGE (4–20% gradient gel), then stained with SYPRO® Ruby Protein Gel Stain. (C) Western blot analysis of virion preparations using an antibody against MPyV VP2/VP3 proteins.

fluorescent spots indicates that the proximity of target proteins is < 40 nm. We selected the time 5 hpi, since, at this time, a subpopulation of the WT virus has previously been detected in ER [7,38]. The PLA spots per cell were quantified in three independent experiments in 40 cells per experiment for each virus variant. Analysis of infected cells using anti-BiP detected all three viruses (WT, as well as both mutated viruses) in the ER lumen in comparable amounts However, using anti-B14, we found a dramatic decrease of PLA spot numbers in cells infected with MPyV-mHD2 in comparison with those present in WT MPyV infected cells. In cells infected with PyV-mHD1, the decrease of PLA spots was not as strong as in the case of MPyV-mHD2. Thus, mutated viruses have a problem in associating with ER membranes. Figure 9 shows representative pictures of PLA spots (Fig. 9A,B) and a graph of quantitative analysis (Fig. 9C).

Further, we examined whether mutant viruses are modified by ER-resident enzymes (which include enzymes that disrupt disulfide bonds). For this, we employed an assay previously used for SV40 and BK [9,11,20,39] that monitors appearance of VP1 monomers and oligomers. Specifically, Shelhaas [11] found that during SV40 infections, ERp57 enzyme eliminates specific interpentameric disulpfide bonds, which leads to release of a subpopulation of monomers from the capsids. Although the disulfide bonded networks in MPyV are different from those in SV40 capsids, previous studies have shown that *in vitro* treatment of the virus by ERp57 generates monomers and oligomers of VP1 [40]. We performed non-reducing SDS/PAGE to monitor the appearance of monomers, dimers or oligomers of VP1. We prepared lysates of cells infected with WT or mutant viruses under alkylating conditions to prevent disulfide bond isomerization during preparation of the lysates. Analysis of VP1 by immunoblotting showed that while 3 hpi, no VP1 was detected on running gel, at later times, 5 and 8 hpi, VP1 monomers, dimers or oligomers of WT and all mutants were

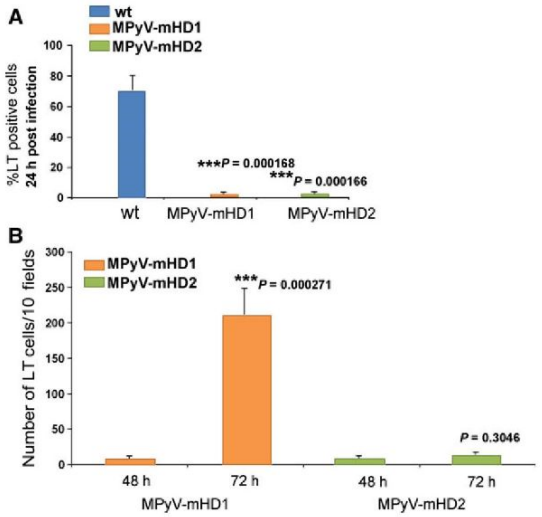

Fig. 8. Infectivity of mutant viruses MPyV-mHD1 and MPyV-mHD2. Mouse 3T6 cells were grown on coverslips to 40% confluency and infected with WT MPyVor mutant viruses MPyV-mHD1 or MPyV-mHD2. The amounts of viruses used were the equivalent of 15 ng of viral DNA per sample. Cells were fixed at the indicated times and stained with antibody against the early viral antigen, LT, and by DAPI. (A) The percentage of LT positive cells (24 hpi) was calculated by counting about 500 cells per experiment. Data in the graph represent mean values of three independent experiments ± SD and infectivity of WT *vs.* each mutant was compared by Student's *t*-test. *P* values are presented. Asterisks represent statistically highly significant differences (***$P \leq 0.001$). (B) The columns represent numbers of LT positively stained cells at 48 or 72 hpi scored per 10 microscopy fields. At these times, uninfected cells had divided several times so a meaningful percentage of infected cells compared to the total cell population could not be calculated. Data in the graph represent mean values ± SD from three experiments. Values of LT positive cells for each mutant in the two different time points were compared by Student's *t*-test. *P* values are presented. Asterisks represent statistically highly significant differences (***$P \leq 0.001$).

present (Fig. 10A), suggesting that all viruses underwent conformational changes in the ER lumen at similar times post-infection.

Together these results indicate that mutated viruses are sorted to the ER without delay, and are processed there by ER-resident enzymes. However, their affinity to membrane is seriously impaired. This suggests a possible defect of the mutated viruses in ER exit.

To follow this, we prepared the ER-enriched microsomal fraction 16 hpi to determine whether virus genomes were still in the ER. Cells were infected (using the same amounts of virus genome equivalents for WT and each mutant), and 1 hpi extracellular virions were neutralized with polyclonal antibodies against VP1 to prevent further viral entry. Cells were then incubated for 6 h (as the loading control, representing the viral subpopulation that arrived at the ER) or 16 hpi. Fractions at 6 hpi were tested by western blotting using antibody against B14 protein (ER marker) to control loading and antibody against VP1 to detect the virus arriving to ER (Fig. 10Ba). Fractions of microsomes from cells harvested at 16 hpi were used for DNA extraction by phenol/chloroform, and viral DNA was amplified by PCR using primers against the LT gene. As control, 16 h microsomal fractions were subjected to western blotting for detection of B14 (microsomal marker). Significant amounts of amplified genomes were detected in the case of MPyV-mHD1 and MPyV-mHD2 mutants (Fig. 10Bb) while only a negligible DNA signal was detected in the sample where WT virus was used.

Together, the above results suggest that mutant viruses with decreased hydrophobicity in minor structural proteins are retained in the ER, apparently as a consequence of impaired association with, and an action on, ER membranes. Infectivity assays revealed that for the MPyV-mHD1 mutant, the exit from the ER appears to be delayed as its early LT antigen could be detected no sooner than 72 hpi (Fig. 8B). Exit of the second mutant, MPyV-mHD2, from the ER seems to be completely prevented. No LT production was detected 72 hpi (Fig. 8B) and even during longer periods post-infection (not shown).

Sensitivity of the mutated viruses to reducing agents, proteases or ER enzymes is not affected by mutations in the hydrophobic domains

Although we did not observe any changes in capsid stability generated by introduction of the mutations in the HD1 or HD2 domains, and in addition in the ER we detected specific disassembly of virions into monomers for all examined viruses (WT, MPyV-mHD1 and MPyV-mHD2), we could not exclude the possibility that mutant viruses could be processed in the ER lumen in a manner that might differ from that observed for WT virus. Therefore, we further evaluated (a) the ability of capsids to disassemble, (b) further morphology changes that are induced by ER proteins (the level of disassembly as well as the exposure of the minor capsid proteins VP2/3), and (c) the pattern of sensitivity to proteases. We found that mutant viruses, as well as WT, were able to disassemble within 300 s to pentamers when treated with dithiothreitol (DTT) and the calcium chelator ethylene glycol-bis (β-aminoethyl ether)-*N*,*N*,*N*′,*N*′-tetraacetic acid (EGTA; Fig. 11Aa,b), indicating that the mutations introduced do not prevent chemical induced virus

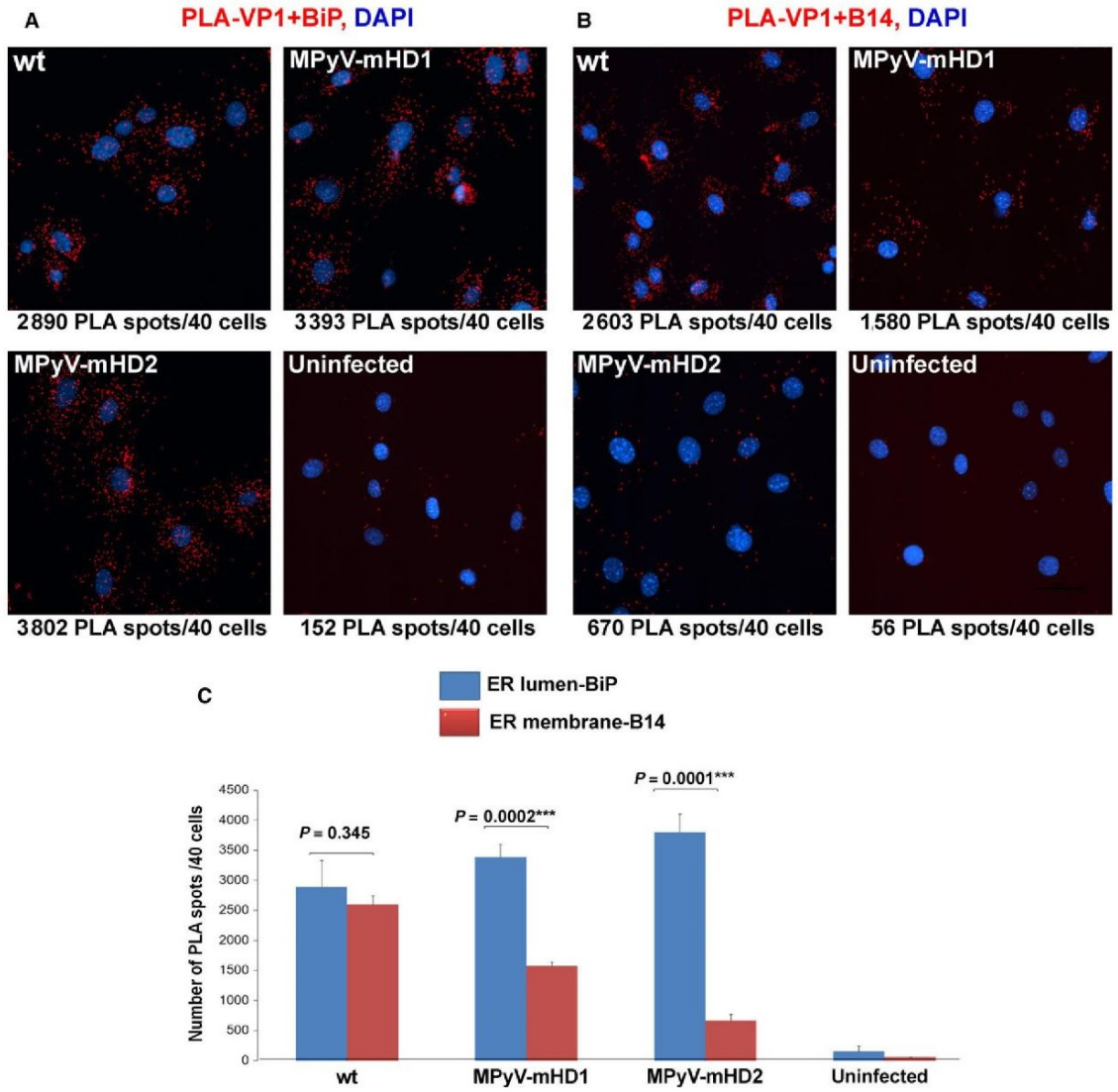

Fig. 9. Proximity ligand assay (PLA) of VP1 and markers of ER in cells infected by WT or mutant viruses. Mouse 3T6 fibroblasts were grown on coverslips infected with MPyV WT or mutants (MPyV-mHD1 or MPyV-mHD2) using amounts of virus equivalent to 15 ng of virus DNA per coverslip. Infected cells were fixed 5 hpi and PLAs performed using primary mouse antibody against VP1 and rabbit antibody against ER luminal marker BiP (A) or mouse antibody against VP1 and rabbit antibody against ER membrane marker B14 (B). As secondary antibodies, the PLA oligoprobe tagged anti-mouse and anti-rabbit antibodies were used. Red spots represent products of oligonucleotide ligation, which takes place only when the oligo probes are in close proximity (< 40 nm). Nuclei were stained with DAPI. As a control, uninfected cells were also assayed. At the bottom of each picture, the average of the numbers of PLA spots from three independent experiments is presented (for each experiment 40 cells were analysed). (C) Graph presenting the values of the PLA spots quantified in three independent experiments for VP1 + BiP antibodies (blue columns) or VP1 + B14 antibodies (red columns). Data in the graph represent mean values of three independent experiments ± SD. Samples were compared by Student's *t*-test. *P* values are given and asterisks represent statistically highly significant differences (***$P \leq 0.001$).

disassembly. When we treated capsids with ER luminal extract, using electron microscopy, we found that both mutant viruses, MPyV-mHD1 and MPyV-mHD2, undergo structural changes similar to those observed for WT. Structural changes led to deformation of particles and, in some cases, to the appearance of

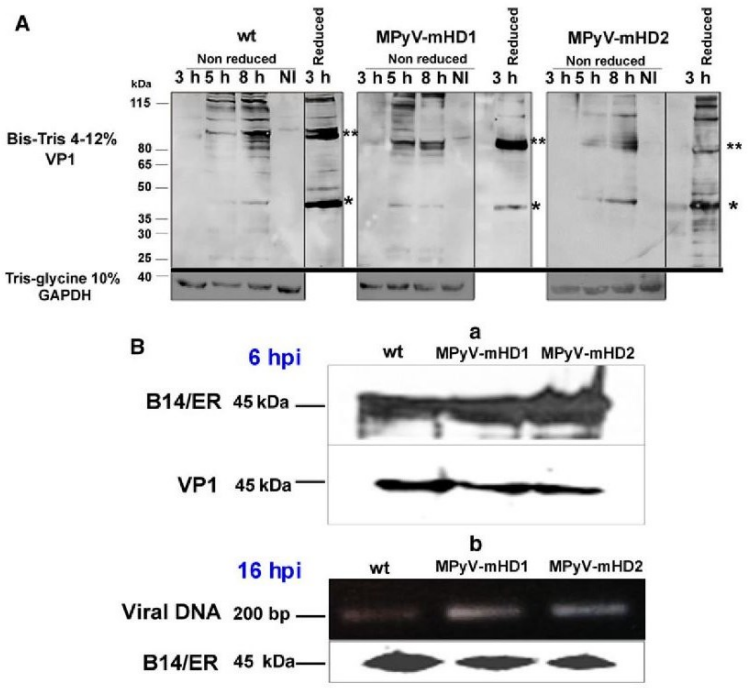

Fig. 10. Analysis of ER processing of virions and exit of their genomes from the ER. Mouse 3T6 fibroblasts were grown on 6 cm-diameter plates and infected with MPyV WT or mutants (MPyV-mHD1 or MPyV-mHD2) using amounts of virus equivalent to 40 ng of virus DNA per plate. (A) Western blots of non-reducing SDS/PAGE for detection of VP1 monomers during infection. Cells were infected with WT or mutant viruses at indicated times post-infection. Cell lysates prepared under alkylating conditions and separated by 4–12% non-reducing gradient SDS/PAGE were immunoblotted for detection of VP1. Three controls were included: lysates of non-infected cells (NI), samples harvested 3 hpi reduced by DTT and, as a loading control, reduced samples for GAPDH detection. VP1 monomers and dimers are indicated by one and two asterisks, respectively. (B) Detection of viral genomes in the ER 16 hpi. Cells were processed 16 hpi (and 6 hpi as loading control) for isolation of enriched microsomal fraction by gradient centrifugation. (a) Control western blot analysis of the presence of VP1 in the microsomal fractions 6 hpi; (b) 1% agarose electrophoresis of viral genomes isolated from the microsomal fractions 16 hpi, amplified by PCR using LT primers. As a control, microsomal fractions 16 hpi were western blotted and stained by antibody against the ER marker B14.

previously described [13] tubular protrusions (Fig. 11Ac; see arrows). The frequency of deformed viruses was determined by observing 200 particles of each virus variant, and revealed no substantial differences between WT virus (81%) and viruses mutated in HD1 (86%) or HD2 (79%) of VP2, indicating that mutant viruses underwent no structural modification by ER enzymes, similar to the WT. In addition, treatment of both WT and mutant viruses with ER luminal extract resulted in exposure of the minor capsid proteins (Fig. 11Ac, right panel). Finally, when we investigated the sensitivity of mutated viruses to trypsin or proteinase K treatment, we found no difference between WT virus and the mutants (Fig. 11B). Taken together these results indicate that mutants and WT virus are likely to be equally stable and sensitive to host cell factors, such as ER enzymes. Thus, the reduction of infectivity of viruses mutated in VP2/VP3 hydrophobic domains is connected with interactions of the minor capsid proteins with ER membranes rather than with conformation changes of virions.

Discussion

Several years of intensive research have resulted in a detail description of the life cycle of polyomaviruses. Nevertheless, molecular mechanisms of some steps of the viral infection need to be further clarified. MPyV, when entering cells along a productive pathway, associates with the endosomal system, passing from early to late endosomes from where the virus is further sorted to the ER. In the lumen of the ER, the virus is processed to expose the minor capsid proteins, and following that it enters the cytosol, just before the viral genome can be detected in the cell nucleus [19,20]. The mechanism by which this transition occurs is poorly

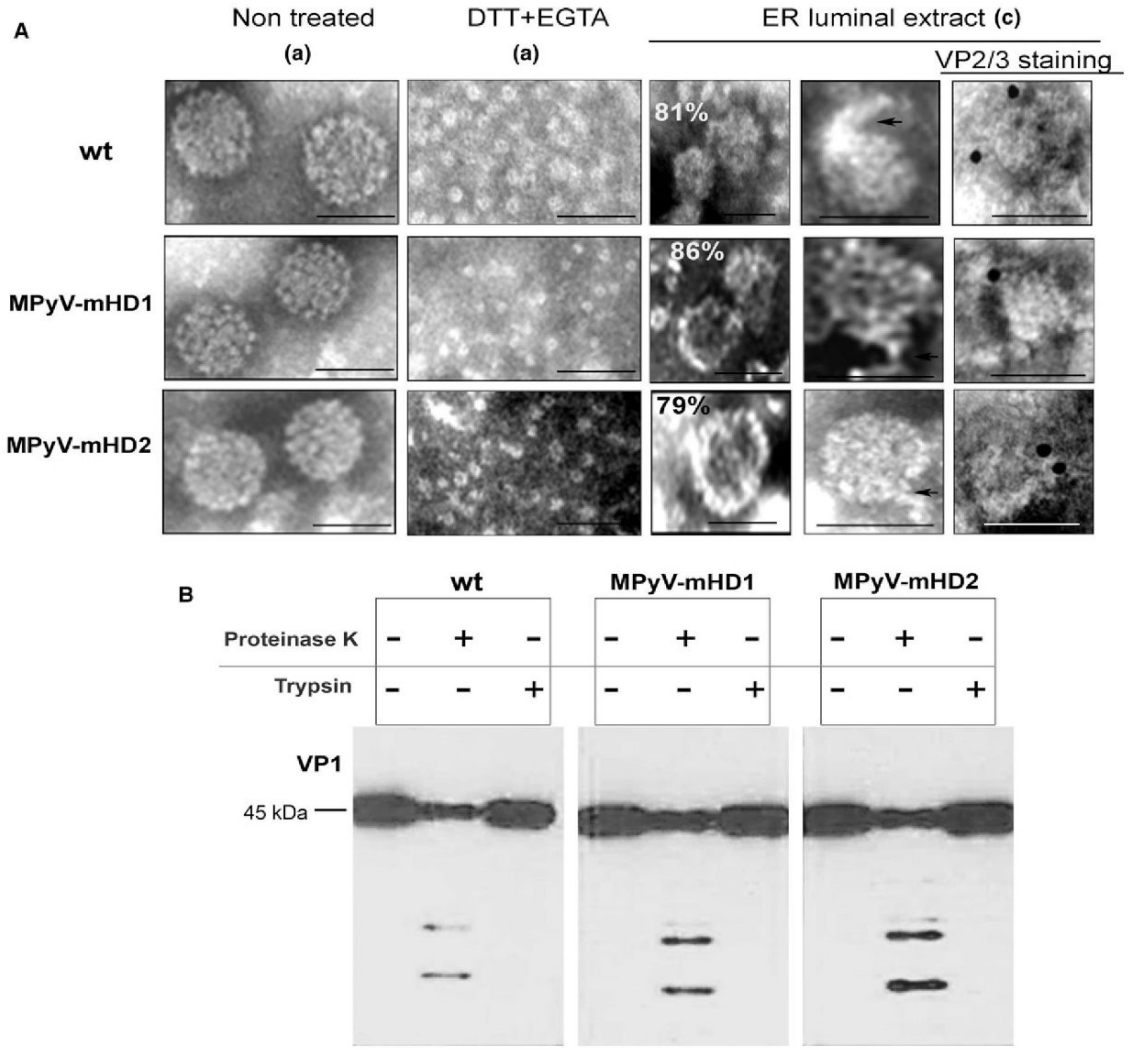

Fig. 11. Mutations in VP2 hydrophobic domains 1 or 2 do not affect virus stability. (A) Electron microscopy (negative staining) of isolated WT or mutant viruses (MPyV-mHD1 or MPyV-mHD2): (a) untreated, (b) treated with 2 mM DTT and 5 mM EGTA for 300 s, or (c) treated by ER luminal extract for 2 h. Note in the left hand panel virus with morphological changes due to the ER luminal extract treatment. The percentage of virions that underwent changes was calculated by analysing features of 200 virions per WT or each mutant. Values are presented in the images. A fraction of the virus treated with ER luminal extract (right panel) was stained with antibodies against VP2/3 protein, followed by a secondary antibody conjugated with 5 nm gold particles (black dots). Bars: 50 nm. Arrows indicate selected features. (B) Western blot of WT and mutant viruses treated with proteinase K or with trypsin, using anti-VP1 antibody.

understood. Previous studies made by our group and others have shown that the MPyV minor structural proteins, VP2 and VP3, when expressed individually, interact with intracellular membranes of host cells [24]. The interaction of minor capsid proteins with microsomal membranes was also observed *in vitro* [25].

Here, we have approached the question of how the hydrophobic sequences of the MPyV minor structural proteins contribute to viral translocation to the cytosol. We used mutation analysis to examine the contributions of individual hydrophobic sequences of the minor capsid proteins in the exiting of virions from the ER. First, we defined the theoretical or potential hydrophobic regions of the minor capsid proteins. On the basis of programs available online, we generated three consensual hydrophobic domains for the larger

minor capsid protein, VP2. We showed previously that both VP2 and VP3 proteins when expressed individually interact with membranes and cause them damage [24]. We now show here that HD2, present in both the VP2 and VP3 minor proteins, is responsible for the minor proteins' ability to bind to membranes, as an HD2-EGFP fusion protein colocalized with ER membranes, while VP2 mutated in HD2 lost this ability. Consistent with this, the virus mutated in VP2/VP3 domain 2 was found in the ER lumen but poorly associated with membranes and was retained in ER. Retention of virus in the ER reflects the inability of the minor capsid proteins to interact with ER membrane. As a consequence, the mutated virus does not productively infect cells. The results of the study of HD1 at the unique N-terminal part of VP2 (not present in VP3) are not so explicit. Isolated HD1 fused with EGFP did not exhibit any affinity for membranes, while the VP2 protein mutated in HD1 bound membranes efficiently. However, the virus mutated in VP2 HD1 was found to be retained in ER for longer, exhibiting some defects in associating with ER membrane (at least a delay in the association, since at 5 hpi the virus did not properly bind to membrane in comparison to WT) and the infectivity of the virus was significantly delayed. From all these results, we suggest that viroporin-like activity of VP2 could be exerted by cooperation of both HD1 and HD2 domains. In our proposed model, HD2 binds with high affinity to ER membrane facilitating either subsequent or simultaneous membrane interaction with HD1, which stabilizes VP2–membrane association and possibly mediates the ability of the protein to induce membrane perforation.

This model is consistent with data showing that viroporins with two α-helices follow a similar pathway, in which a second domain inserts into the membrane only after the insertion of the first domain. It has been suggested that insertion of the second domain facilitates oligomerization to enhance the viroporin activity [41].

Interestingly, HD3, which corresponds to the amino acid stretch at the C terminus of VP2/VP3 that was described earlier by crystallography as an α-helix [18], did not display viroporin properties under the evaluated conditions. VP2 protein mutated in HD3 was still able to bind to membranes efficiently and to induce cytotoxicity. HD3 alone fused with EGFP localized in the cell nucleus and did not bind membranes. In the context of the virus, this hydrophobic region makes contact with the central cavity of VP1 pentamers and until considerable conformation change has taken place, it is not free for interactions with cellular structures. Unfortunately, in our hands, any mutation introduced to decrease hydrophobicity of HD3 affected virion assembly and/or stability. Interestingly, at low pH (pH 5), a peptide representing the last 35 amino acids from the C terminus of VP2/VP3 (containing the HD3) acted as a protein transduction domain able to interact with and perforate liposomes (our unpublished data). These data suggest that HD3 behaves as a hydrophobic domain under low pH conditions. Although MPyV first enters the cell in acidic vesicles, because MPyV seems not to be disassembled in these endosomes, the HD3 sequence will not be exposed and, therefore, is probably prevented from any membrane interaction. Further, in the ER, where polyoma virion remodelling was described [9,19], pH conditions are not optimal for viroporin-like action of this domain.

Our results are in agreement with those from an earlier study where authors, using an *in vitro* system, demonstrated that VP2 protein added to isolated microsomes bound to and perforated their membranes, while VP3 protein (lacking HD1) bound membranes but was not able to perforate them [25].

Here, we show that VP2 protein with mutated HD1 binds membranes as efficiently as WT VP2 but its cytotoxicity is lower. Indeed, in our previous study [24], we noticed a slightly decreased ability of VP3 (which lacks this domain) to perforate the cells by measuring LDH release at 12 h post-transfection. Nevertheless, later (24 h post-transfection), both VP2 and VP3 were able to efficiently kill all cells transfected. We suppose that these differences in the kinetics of cell killing can be explained by different abilities of VP2 and VP3 to perforate membranes, as observed in the *in vitro* experiment [25] mentioned above. As membranes can be perforated by different mechanisms, for instance the transient modification of membranes, pore formation, or total local disruption [27], we assume that VP2 mutated in HD1 or VP3 (lacking HD1) can induce, through the integration of HD2, transient membrane modification into the membrane. Thus, the overexpression of the proteins may finally result in membrane disruption. On the other hand, WT VP2 may act as a real lytic factor that induces efficient and fast pore formation, most likely by oligomerization after insertion of the HD1 domain. Our conclusion is supported by the experiments showing that the mutant virus carrying mutation in HD1 is retained in the ER, but later, with a delay of 2 days, when the membrane is destabilized, the virus exits the ER and continues in productive infection.

It was shown that SV40 interacts with ER translocon-related proteins through recognition of an N-terminal positively charged glutamic acid residue in position 17 of the VP2 protein [20,29]. These findings have led

to the hypothesis that the virus exploits a translocon channel to exit from the ER to the cytosol. Recent studies, trying to clarify the role of ER translocon proteins during early steps of infection by SV40 polyomavirus, revealed that B14/B12, which are localized in foci, bind to small glutamine-rich tetratricopeptide repeat-containing protein α (SGTA) in an Hsp70-dependent manner: STGA engages the virus and acts as a driving force essential to complete virus penetration to the cytosol [13]. Our studies show that in addition to the possible interactions between MPyV minor proteins and ER translocon, direct membrane interactions of hydrophobic domains, HD1 of VP2 and HD2 common to both VP2 and VP3, are necessary for the efficient exit of MPyV from the ER and for virus infectivity. The results presented in this paper are in agreement with Giorda *et al.*, [28], who described three hydrophobic domains in the VP2 protein of SV40 virus, which are required for viral infectivity. Thus, polyomaviruses exploit hydrophobic properties of minor proteins to exit to the cytosol on their way to the nucleus, where they replicate.

Materials and methods

Cell lines and viruses

Mouse fibroblasts, 3T6 (ATCC; Manassas, VA, USA; CCL-96) and NIH 3T3 (ATCC; CRL-1658), were grown at 37 °C in a humidified incubator with a 5% CO_2 atmosphere, using Dulbecco's modified Eagle's medium (DMEM) from Sigma-Aldrich (St Louis, MO, USA) supplemented with 10% fetal bovine serum (Thermo Fisher Scientific, Waltham, MA, USA) and 4 mM L-glutamine (Thermo Fisher Scientific). Mouse polyomavirus, A3 strain (GenBank: J02289.1) was prepared using pMJG plasmid, which contains the entire genome of MPyV strain A3. Derivatives of pMJG, MPyV-mHD1, MPyV-mHD2 and MPyV-mHD3, were used as a source of mutated genomes. To prepare WT and mutated MPyV genomes, the viral sequences were excised from the plasmids with *Eco*RI and circularized. Ligation mixtures were used for the transfection of 3T6 cells by nucleofection. Cells transfected were incubated for 6–8 days and then virus was isolated by CsCl gradient centrifugation [42].

Plasmids and transfections

We used the plasmids VP2-EGFP-N1, VP3-EGFP-N1 [24], a derivative of the vector pEGFP-N1 (Clontech, Mountain View, CA, USA) encoding MPyV minor capsid proteins, VP2 or VP3, and the pMJG plasmid containing the entire genome sequence of the mouse polyomavirus strain A3 [37].

VP2-EGFP-N1 and pMJG plasmids were used as templates for introducing mutations into the hydrophobic domains of the minor capsid proteins using the QuikChange site-directed mutagenesis Kit (Stratagene, La Jolla, CA, USA).

Short versions of VP2 or VP3 protein with deletions were prepared by using VP2-EGFP-N1 or VP3-EGFP-N1 plasmids. The deletion variant of VP2 carrying intact HD1 (HD1-EGFP) only was prepared by restriction of VP2-EGFP-N1 with *Kpn*I and *Bam*HI. The fragment corresponding to the vector plus the sequence encoding the first 122 amino acids of VP2 protein was isolated and fused to a synthetic oligonucleotide encoding VP2 NLS (EEDGPQ-KKKRRL). The second hydrophobic domain fused to EGFP (HD2-EGFP) was prepared using the VP3-EGFP-N1 plasmid as template for PCR. The fragment generated encodes the VP3 sequence with deletion of 13 amino acids (aa 285–297) in the C terminus part, upstream of the NLS. To produce this fragment, we used the following set of primers: VP3 (*Bgl*II): 5′-CAGAC AGATCT AGAAA-TATGGCGTTGATACC-3′; and VP(2 + 3) deltaHX (*Eco*RV) 5′-CAGAC GATATC AGTGACTCTTTGG-TGGGAC-3′. Next, the *Bgl*II–*Eco*RV fragment of the VP3-EGFP-N1 vector was replaced by the PCR product generated above.

The third domain fused to EGFP (HD3-EGFP) was prepared using VP3-EGFP-N1 plasmid as a template for PCR to generate a fragment lacking 40 amino acids at the N terminus of VP3 (126–165 aa numbering in VP2). To produce this fragment, we used the following set of primers: VP3ΔD2 *Nhe*I: 5′-TT GAC GCT AGC ATG GCG TTG ATA CCA-3′; and VP2/3ΔD2 *Hin*dIII: 5′-AT CTG AAG CTT TCG CCA AGT CCC GAG ACG CCG CTT TTT C-3′. The PCR product was cloned into the plasmid EGFP-N1.

Plasmid DNAs were prepared using the EndoFree maxi kit (Qiagen, Hilden, Germany), diluted in TE and stored at −20 °C. Plasmid concentration and purity were determined by nanodrop (Thermo Fisher Scientific). Transfections were performed by electroporation within a Nucleofector™ device, using Amaxa-kit V (Lonza, Basel, Switzerland) according to the manufacturer's instructions. Briefly, cells were seeded 24 h before transfection, and 4×10^6 cells were transfected with 6 μg of plasmid DNA.

Viral genome quantification

Isolated viral particles were treated by DNase I to remove residual extracellular DNA. After DNase inactivation, capsids were disassembled by proteinase K and DTT treatment, then viral DNA was extracted by phenol/chloroform followed by ethanol precipitation according to the protocol previously described [43]. Viral DNA was quantified by real-time PCR assay using iQ™ SYBR® Green Supermix (Bio-Rad Laboratories, Hercules, CA, USA) detection. The primers sets used were the following: VP1: 5′-GCAA-GAAGGCGACGAC-3′ and 5′-TGGCCTCCCTCATAAG-T-3′; and LT: 5′-GCTGACAAAGAAAGGCTGCT-3′ and

5′-AGCCGGTTCCTCCTAGATTC-3′. Thermal cycling was performed in a Light Cycler 480 II (Roche, Penzberg, Upper Bavaria, Germany). DNA concentrations were calculated using a standard curve of known viral DNA concentrations.

Hemagglutination assay

Viruses were subjected to haemagglutination assays using guinea pig erythrocytes as previously described [42]. Te HA titre was defined as the reciprocal of the highest virus dilution showing haemagglutination.

SDS/PAGE and western blot analysis

Samples for reducing SDS/PAGE were resuspended in Laemmli buffer [44] and applied to gradient gels of 4–20% (Mini-PROTEAN® TGX, Bio-Rad) or 10% acrylamide gels. Next, the gels were either stained using SYPRO® Ruby Protein Gel Stain (Thermo Fisher Scientific) or electroblotted to nitrocellulose or polyvinylidene fluoride membrane and immunostained using the indicated antibodies.

For non-reducing SDS/PAGE, cell lysates were prepared under alkylating conditions using *N*-ethylmaleimide (Sigma-Aldrich), according to the protocol of Jiang *et al.* [39]. Next, cell lysates were resuspended in the sample buffer – NuPAGE® LSD (Thermo Fisher Scientific) under non-reducing conditions. Samples were run on NuPAGE® Bis–Tris on 4–12% gradient gel (Thermo Fisher Scientific) with running buffer without antioxidants.

Cell fractionation

Cells were transfected by Amaxa nucleofector, and at indicated times cells were collected and fractionated using the subcellular protein fractionation kit for cultured cells (Thermo Fisher Scientific), according to manufacturer's instructions.

Antibodies

The primary antibodies used were rabbit polyclonal anti-BiP from Abcam (Cambridge, UK), rabbit polyclonal anti-DnaJB14 (B14) from Proteintech (Chicago, IL, USA), rabbit anti-calnexin (Abcam), mouse monoclonal anti-lamin A/C (Santa Cruz Biotechnology, Dallas, TX, USA), rabbit polyclonal anti-GAPDH (Santa Cruz), rabbit polyclonal anti-VP1 antibody and mouse monoclonal anti-VP2/3 (prepared in our laboratory), mouse monoclonal anti-VP1 and rat monoclonal anti-LT (provided by B. E. Griffin, Imperial College of Science, Technology and Medicine at St Mary's, London, UK).

The secondary antibodies used were goat anti-mouse and goat anti-rabbit conjugated with peroxidase, donkey anti-mouse conjugated with AlexaFluor 488 and donkey anti-rabbit conjugated with Alexa Fluor 546, all from Thermo Fisher Scientific. Goat anti-mouse conjugated with 5-nm diameter gold particles was obtained from GE Healthcare (Waukesha, WI, USA).

Electron microscopy

Samples for negative staining were processed by placing a drop of sample on a carbon-coated copper or nickel grid (where indicated, samples loaded on the grid were incubated with antibodies and gold particles as detailed in the figure legends) and then the grid was stained with 2% phosphotungstic acid. The samples were observed with a JEOL JEM (Akishima, Tokyo, Japan) 1200EX electron microscope operating at 80 kV.

Immunofluorescence staining

Cells were grown on coverslips and at the appropriate time points fixed with 4% paraformaldehyde in PBS for 15 min and permeabilized with 0.5% Triton X-100 in PBS for 5 min. After washing in PBS, cells were incubated for 30 min with 0.25% bovine serum albumin and 0.25% porcine skin gelatine in PBS. Immunostaining with primary and secondary antibody was carried out for 1 h and 30 min, respectively, with extensive washing with PBS after each incubation. Coverslips were mounted on droplets of glycerol with 4′,6′-diamidino-2-phenylindole (DAPI). Images were obtained with a TCS SP8 confocal microscope (Leica, Wetzlar, Germany).

Proximity ligation assay

The assay was performed using the Duolink kit (Sigma-Aldrich) according to the manufacturer's instructions. The probes used were anti-rabbit plus (DUO92002) and anti-mouse minus (DUO92004). The infected cells were fixed and incubated with two combinations of antibodies: mouse antibody against VP1 and rabbit antibody against BiP (ER luminal marker) or mouse antibody against VP1 and rabbit antibody against B14 (ER membrane marker). After washing, cells were incubated with PLA oligoprobe tagged secondary anti-mouse and anti-rabbit antibodies. Then the ligation reaction was performed. For detection of ligation products, *in situ* PCR was carried out and products visualized by hybridization of fluorescently labelled oligonucleotides (λ_{ex} = 594 nm and λ_{em} = 624 nm). The signal was detected by fluorescence microscopy.

ER luminal extract preparation

Mouse microsomes from Sigma-Aldrich were used as a source of luminal proteins. In brief, to prepare luminal

extract, approximately 1 mg of microsomes was treated with detergent buffer (23 mM *N*-octyl β-D-glucopyranose, 25 mM Tris pH 7, 250 mM sucrose) for 30 min on ice. Then detergent was removed by using SM-2 BioBeads from Bio-Rad.

Enriched microsomal fractions

Crude ER microsomal fractions were prepared by differential centrifugation using the ER Isolation Kit (Sigma-Aldrich), according to the manufacturer's instructions.

Virion treatment with proteinase K and trypsin

From viral stocks, samples equivalent to 0.4 μg of protein were diluted in PBS to a final volume of 10 μL. Then, samples were treated either with Proteinase K (2.5 $ng \cdot mL^{-1}$ final concentration) or with trypsin (1 $mg \cdot mL^{-1}$ final concentration) and incubated for 20 min on ice. Then, the samples were resuspended in Laemmli buffer and subject to SDS/PAGE.

Virus infection

Cells were seeded on 13-mm glass coverslips and grown to a confluency of about 40%. For infection, cells were washed with serum-free DMEM and incubated with MPyV diluted in serum-free medium for 1 h at 37 °C. The infection start point was measured from when the virus was added to cells. After virus adsorption, cells were washed to remove the unbound virus and incubated in DMEM supplemented with 10% FBS until the indicated times.

Cytotoxicity measurement

The release of LDH that occurred upon cell lysis was quantified using a CytoTox 96 cytotoxicity assay kit (Promega, Fitchburg, WI, USA), according to the manufacturer's instructions. Briefly, cells were transfected by electroporation and then seeded on 24-well plates. Three hours post-transfection, the medium was replaced with fresh medium to remove dead cells (the cells that died due to the electrical pulse). Twelve hours post-transfection, medium from growing cells was harvested to measure LDH. Medium from cells treated by Triton X-100 was harvested to calculate total LDH release. Absorbance was measured by an ELISA reader (490 nm).

Acknowledgements

This study was supported by the Grant Agency of the Czech Republic (Project P302/13-26115S), by Charles University in Prague (Project UNCE 204013) and by the project BIOCEV – Biotechnology and Biomedicine Centre of the Academy of Sciences and Charles University (CZ.1.05/1.1.00/02.0109), from the European Regional Development Fund. We thank Ondrej Vit for constructing the HD1-EGFP and HD3-EGFP plasmids and Vojtech Zila for the construction of HD2-EGFP; also the Imaging Methods Core Facility at BIOCEV, an institution supported by the Czech-Bio Imaging large RI project (LM2015062 funded by MEYS CR), for their support with obtaining scientific data presented in this paper.

Author contributions

Conception and design of the experiments: SH, JF, HS, BR. Performance of the experiments: SH, BR, HS. Analysis of the data: SH JF, HS, BR. Writing of the paper: SH, JF.

References

1 Burckhardt CJ, Suomalainen M, Schoenenberger P, Boucke K, Hemmi S & Greber UF (2011) Drifting motions of the adenovirus receptor CAR and immobile integrins initiate virus uncoating and membrane lytic protein exposure. *Cell Host Microbe* **10**, 105–117.

2 Richards RM, Lowy DR, Schiller JT & Day PM (2006) Cleavage of the papillomavirus minor capsid protein, L2, at a furin consensus site is necessary for infection. *Proc Natl Acad Sci USA* **103**, 1522–1527.

3 Day PM, Thompson CD, Schowalter RM, Lowy DR & Schiller JT (2013) Identification of a role for the trans-Golgi network in human papillomavirus 16 pseudovirus infection. *J Virol* **87**, 3862–3870.

4 Aydin I, Weber S, Snijder B, Samperio Ventayol P, Kühbacher A, Becker M, Day PM, Schiller JT, Kann M, Pelkmans L *et al.* (2014) Large scale RNAi reveals the requirement of nuclear envelope breakdown for nuclear import of human papillomaviruses. *PLoS Pathog* **10**, e1004162.

5 Moriyama T & Sorokin A (2008) Intracellular trafficking pathway of BK Virus in human renal proximal tubular epithelial cells. *Virology* **371**, 336–349.

6 Liebl D, Difato F, Hornikova L, Mannova P, Strokrova J & Forstova J (2006) Mouse polyomavirus enters early endosomes, requires their acidic pH for productive infection, and meets transferrin cargo in rab11-positive endosomes. *J Virol* **80**, 4610–4622.

7 Qian M, Cai D, Verhey KJ & Tsai B (2009) A lipid receptor sorts polyomavirus from the endolysosome to the endoplasmic reticulum to cause infection. *PLoS Pathog* **5**, e1000465.

8 Cavaldesi M, Caruso M, Sthandier O, Amati P & Garcia MI (2004) Conformational changes of murine polyomavirus capsid proteins induced by sialic acid binding. *J Biol Chem* **279**, 41573–41579.

9 Inoue T & Tsai B (2011) A large and intact viral particle penetrates the endoplasmic reticulum membrane to reach the cytosol. *PLoS Pathog* **7**, e1002037.

10 Magnuson B, Rainey EK, Benjamin T, Baryshev M, Mkrtchian S & Tsai B (2005) ERp29 triggers a conformational change in polyomavirus to stimulate membrane binding. *Mol Cell* **20**, 289–300.

11 Schelhaas M, Malmström J, Pelkmans L, Haugstetter J, Ellgaard L, Grünewald K & Helenius A (2007) Simian Virus 40 depends on ER protein folding and quality control factors for entry into host cells. *Cell* **131**, 516–529.

12 Dupzyk A & Tsai B (2016) How Polyomaviruses Exploit the ERAD Machinery to Cause Infection. *Viruses* **8**, doi: 10.3390/v8090242.

13 Inoue T, Dosey A, Herbstman JF, Ravindran MS, Skiniotis G & Tsai B (2015) The ERdj5 reductase cooperates with PDI to promote SV40 ER membrane translocation. *J Virol* **89**, 8897–8909.

14 Stehle T & Harrison SC (1996) Crystal structures of murine polyomavirus in complex with straight-chain and branched-chain sialyloligosaccharide receptor fragments. *Structure* **4**, 183–194.

15 Liddington RC, Yan Y, Moulai J, Sahli R, Benjamin TL & Harrison SC (1991) Structure of simian virus 40 at 3.8-A resolution. *Nature* **354**, 278–284.

16 Rayment I, Baker TS, Caspar DL & Murakami WT (1982) Polyoma virus capsid structure at 22.5 A resolution. *Nature* **295**, 110–115.

17 Barouch DH & Harrison SC (1994) Interactions among the major and minor coat proteins of polyomavirus. *J Virol* **68**, 3982–3989.

18 Chen XS, Stehle T & Harrison SC (1998) Interaction of polyomavirus internal protein VP2 with the major capsid protein VP1 and implications for participation of VP2 in viral entry. *EMBO J* **17**, 3233–3240.

19 Kuksin D & Norkin LC (2012) Disassociation of the SV40 genome from capsid proteins prior to nuclear entry. *Virol J* **9**, 158.

20 Geiger R, Andritschke D, Friebe S, Herzog F, Luisoni S, Heger T & Helenius A (2011) BAP31 and BiP are essential for dislocation of SV40 from the endoplasmic reticulum to the cytosol. *Nat Cell Biol* **13**, 1305–1314.

21 Mannova P, Liebl D, Krauzewicz N, Fejtova A, Stokrova J, Palkova Z, Griffin BE & Forstova J (2002) Analysis of mouse polyomavirus mutants with lesions in the minor capsid proteins. *J Gen Virol* **83**, 2309–2319.

22 Gasparovic ML, Gee GV & Atwood WJ (2006) JC virus minor capsid proteins Vp2 and Vp3 are essential for virus propagation. *J Virol* **80**, 10858–10861.

23 Nakanishi A, Itoh N, Li PP, Handa H, Liddington RC & Kasamatsu H (2007) Minor capsid proteins of simian virus 40 are dispensable for nucleocapsid assembly and cell entry but are required for nuclear entry of the viral genome. *J Virol* **81**, 3778–3785.

24 Huerfano S, Zila V, Boura E, Spanielova H, Stokrova J & Forstova J (2010) Minor capsid proteins of mouse polyomavirus are inducers of apoptosis when produced individually but are only moderate contributors to cell death during the late phase of viral infection. *FEBS J* **277**, 1270–1283.

25 Rainey-Barger EK, Magnuson B & Tsai B (2007) A chaperone-activated nonenveloped virus perforates the physiologically relevant endoplasmic reticulum membrane. *J Virol* **81**, 12996–13004.

26 Burkert O, Kressner S, Sinn L, Giese S, Simon C & Lilie H (2014) Biophysical characterization of polyomavirus minor capsid proteins. *Biol Chem* **395**, 871–880.

27 Moyer CL & Nemerow GR (2011) Viral weapons of membrane destruction: variable modes of membrane penetration by non-enveloped viruses. *Curr Opin Virol* **1**, 44–49.

28 Giorda KM, Raghava S, Zhang MW & Hebert DN (2013) The viroporin activity of the minor structural proteins VP2 and VP3 is required for SV40 propagation. *J Biol Chem* **288**, 2510–2520.

29 Walczak CP, Ravindran MS, Inoue T & Tsai B (2014) A cytosolic chaperone complexes with dynamic membrane J-proteins and mobilizes a nonenveloped virus out of the endoplasmic reticulum. *PLoS Pathog* **10**, e1004007.

30 Snider C, Jayasinghe S, Hristova K & White SH (2009) MPEx: a tool for exploring membrane proteins. *Protein Sci* **18**, 2624–2628.

31 Sipos L & von Heijne G (1993) Predicting the topology of eukaryotic membrane proteins. *Eur J Biochem* **213**, 1333–1340.

32 Pasquier C, Promponas VJ, Palaios GA, Hamodrakas JS & Hamodrakas SJ (1999) A novel method for predicting transmembrane segments in proteins based on a statistical analysis of the SwissProt database: the PRED-TMR algorithm. *Protein Eng* **12**, 381–385.

33 Hoffman K & Stoffel W (1993) TMbase – A database of membrane spanning proteins segments. Paper presented at the *Biol Chem Hoppe-Seyler* **374**, 166.

34 Tusnády GE & Simon I (2001) The HMMTOP transmembrane topology prediction server. *Bioinformatics* **17**, 849–850.

35 Mitra B, Gerlt JA, Babbitt PC, Koo CW, Kenyon GL, Joseph D & Petsko GA (1993) A novel structural basis for membrane association of a protein: construction of a chimeric soluble mutant of (S)-mandelate dehydrogenase from Pseudomonas putida. *Biochemistry* **32**, 12959–12967.

36 von Heijne G (2006) Membrane-protein topology. *Nat Rev Mol Cell Biol* **7**, 909–918. Review.

37 Krauzewicz N, Streuli CH, Stuart-Smith N, Jones MD, Wallace S & Griffin BE (1990) Myristylated polyomavirus VP2: role in the life cycle of the virus. *J Virol* **64**, 4414–4420.
38 Zila V, Difato F, Klimova L, Huerfano S & Forstova J (2014) Involvement of microtubular network and its motors in productive endocytic trafficking of mouse polyomavirus. *PLoS ONE* **9**, e96922.
39 Jiang M, Abend JR, Tsai B & Imperiale MJ (2009) Early events during BK virus entry and disassembly. *J Virol* **83**, 1350–1358.
40 Walczak CP & Tsai B (2011) A PDI family network acts distinctly and coordinately with ERp29 to facilitate polyomavirus infection. *J Virol* **85**, 2386–2396.
41 Martinez-Gil L & Mingarro I (2015) Viroporins, examples of the two-stage membrane protein folding model. *Viruses* **7**, 3462–3482.
42 Horníková L, Žíla V, Španielová H & Forstová J (2015) Mouse polyomavirus: propagation, purification, quantification, and storage. *Curr Protoc Microbiol* **38**, 14F.1.1–14F.1.26.
43 Orlando SJ, Nabavi M & Gharakhanian E (2000) Rapid small-scale isolation of SV40 virions and SV40 DNA. *J Virol Methods* **90**, 109–114.
44 Laemmli UK (1970) Cleavage of structural proteins during the assembly of the head of bacteriophage T4. *Nature* **227**, 680–685.

The FEBS Journal

FEBS PRESS science publishing by scientists

Immune sensing of mouse polyomavirus DNA by p204 and cGAS DNA sensors

Boris Ryabchenko, Irina Soldatova, Vojtech Šroller, Jitka Forstová and Sandra Huérfano

Department of Genetics and Microbiology, Faculty of Science, Charles University, Biocev, Czech Republic

Keywords
cGAS sensor; immune sensing of DNA; mouse polyomavirus; p204 sensor; pattern recognition receptors

Correspondence
S. Huérfano, Department of Genetics and Microbiology, Faculty of Science, Charles University, Biocev, Vestec 25250, Czech Republic
Tel: +420325873955
E-mail: huerfano@natur.cuni.cz

Boris Ryabchenko and Irina Soldatova contributed equally to this work.

(Received 16 March 2021, revised 20 May 2021, accepted 7 May 2021)

doi:10.1111/febs.15962

The mechanism by which DNA viruses interact with different DNA sensors and their connection with the activation of interferon (IFN) type I pathway are poorly understood. We investigated the roles of protein 204 (p204) and cyclic guanosine-adenosine synthetase (cGAS) sensors during infection with mouse polyomavirus (MPyV). The phosphorylation of IFN regulatory factor 3 (IRF3) and the stimulator of IFN genes (STING) proteins and the upregulation of IFN beta (IFN-β) and MX Dynamin Like GTPase 1 (MX-1) genes were detected at the time of replication of MPyV genomes in the nucleus. STING knockout abolished the IFN response. Infection with a mutant virus that exhibits defective nuclear entry via nucleopores and that accumulates in the cytoplasm confirmed that replication of viral genomes in the nucleus is required for IFN induction. The importance of both DNA sensors, p204 and cGAS, in MPyV-induced IFN response was demonstrated by downregulation of the IFN pathway observed in p204-knockdown and cGAS-knockout cells. Confocal microscopy revealed the colocalization of p204 with MPyV genomes in the nucleus. cGAS was found in the cytoplasm, colocalizing with viral DNA leaked from the nucleus and with DNA within micronucleus-like bodies, but also with the MPyV genomes in the nucleus. However, 2′3′-Cyclic guanosine monophosphate–adenosine monophosphate synthesized by cGAS was detected exclusively in the cytoplasm. Biochemical assays revealed no evidence of functional interaction between cGAS and p204 in the nucleus. Our results provide evidence for the complex interactions of MPyV and DNA sensors including the sensing of viral genomes in the nucleus by p204 and of leaked viral DNA and micronucleus-like bodies in the cytoplasm by cGAS.

Introduction

The Polyomaviridae family of small nonenveloped DNA tumor viruses consists of viruses that infect birds and mammals. Presently, 14 human polyomaviruses have been described [1,2]. Some, notably the BK polyomavirus (BKPyV), the JC polyomavirus (JCPyV), the Merkel cell polyomavirus (MCPyV), and the trichodysplasia spinulosa polyomavirus (TSPyV), were found to have a clear association with human diseases [3–6]. Human polyomaviruses are prevalent in the healthy population [7] and cause disease in immunosuppressed hosts. The high prevalence of polyomaviruses in the healthy population suggests that these viruses modulate the immune response to keep low levels of replication in favor of persistence [8–10].

Abbreviations
2′3′-cGAMP, 2′3′-Cyclic guanosine monophosphate–adenosine monophosphate; cGAS, cyclic guanosine-adenosine synthetase; IFI16, interferon-gamma-inducible protein 16; IFN, interferon; IFN-β, interferon beta; IRF3, interferon regulatory factor 3; MPyV, mouse polyomavirus; MX-1, MX Dynamin Like GTPase 1; p204, protein 204; STING, the stimulator of IFN genes.

Two nonhuman members of the family, the simian virus 40 (SV40) and the mouse polyomavirus (MPyV), have served as models for the study of the polyomavirus replication cycle, cellular processes, such as DNA replication and endocytosis, targeting the cell nucleus, and mechanisms of cell transformation. In this study, MPyV was used as a model polyomavirus to study the host mechanisms of viral DNA sensing. MPyV has a capsid with icosahedral symmetry composed of 72 pentamers of the major capsid protein, VP1. One molecule of the two minor capsid proteins, either VP2 or VP3, is noncovalently bound to the central cavity of each VP1 pentamer [11,12]. Inside the capsid, the circular double-strand (ds) DNA genome, approximately 5.3 kbp long, forms a condensed nucleocore with cellular 2A, 2B, 3, and 4 histones. The genome encodes four early regulatory proteins, large tumor antigen (LT), small T antigen (ST), middle T (MT), and tiny T antigen (reviewed in [13]), and three late gene structural proteins, VP1, VP2, and VP3. The genomes of polyomaviruses are transcribed and replicated in the cell nucleus. Electron microscopy studies of MPyV minichromosomes isolated from cell nuclei have shown that there are gaps free of nucleosomes present in approximately 20% of genomes. The gaps were mapped to the regulatory region, between the origin of replication (ORI) and late transcription start [14–16].

MPyV virions are internalized by host cells in monopinocytic vesicles and sorted through the early and late endosomes to the endoplasmic reticulum (ER) [17–19]. In the ER, the virus undergoes conformational changes that promote the exit of remodeled and partially disassembled virions to the cytosol [20–22]. At approximately 6 h postinfection (hpi), the partially disassembled viral particles interact with importins, which promote viral DNA translocation to the nucleus via nucleopores [23]. Once the viral genomes appear in the nucleus, transcription of the early region starts. Genome replication initiated by the LT antigen and coincident late transcription from the complementary strand can be detected from 12 to 15 hpi. At 20–24 hpi, there is a dramatic change in the relative abundance of the late/early transcripts dependent on massive viral DNA replication (reviewed in [13]). The new virus progeny is assembled and released from infected cells at 40–48 hpi [24].

Innate immune DNA sensors are proteins that recognize pathogenic DNA and induce the production of interferon (IFN) and other host cytokines. DNA sensors are localized in the endosomes, free in the cytosol and, unexpectedly, in the cell nucleus. Toll-like receptor 9 (TLR9) is the only DNA sensor found in endosomes [25–27], whereas at least 11 DNA sensors were found to signal from the cytosol: DNA-dependent activator of IFN regulatory factors (DAI) [28]; RNA polymerase III (converting the cytosolic poly (dA-dT) DNA into 5′-pppRNA, which is then recognized by the RIG-I pathway) [29]; absence in melanoma 2 (AIMS 2) [30]; IFN-gamma-inducible protein 16 (IFI16) or its mouse ortholog, protein 204 (p204) [31–33]; leucine-rich repeat containing protein [34]; Ku70/Ku80 protein [35]; DEAH box polypeptide 9 and DHX36 (DEAH box polypeptide 36) [36]; DDX41 helicase [37]; cyclic guanosine-adenosine synthetase (cGAS) [38,39]; and IFN-inducible protein X (IFIX) [40]. Of these sensors, IFI16 (p204 in mice) and IFIX [32,40–43] were found to sense DNA in the nucleus. In addition, cGAS, described as a cytosolic sensor, is found in both the cytoplasm and the cell nucleus and there is one report suggesting its nuclear activation. The authors showed that in dendritic cells, the overproduction of cGAS fused to the nuclear localization signal (NLS) functionally upregulates the cellular innate immune responses [44]. The mechanisms used by DNA nuclear sensors to distinguish self-DNA from foreign DNA in the nucleus are an emerging topic of study [44–52]. It was shown that nucleosomes are barriers that prevent IFI16 from targeting self-DNA in the nucleus [45]. Likewise, it was shown that cGAS anchors nucleosomes. The nucleosome-binding interface was shown to be occupied by the DNA binding surface of the sensor, thus preventing sensing of self-DNA [53]. For IFI16 and cGAS, post-translational modifications including phosphorylation, acetylation, glutamylation, and ubiquitination have been shown to affect the activity or distribution of the protein [41,46–48,51,54,55].

At present, the most well-characterized mechanisms of DNA sensing are those mediated by IFI16 (p204 homolog) and by cGAS. The nuclear sensing of viral DNA by IFI16 has been studied widely in herpes viral infections. In detail, after the binding of IFI16 to herpesvirus genomes, IFI16 is acetylated and exported to the cytosol where it is available for interaction with the stimulator of IFN genes (STING) [56,57]. Further studies showed that IFI16 or p204 oligomerizes on DNA to induce the formation of filaments [45,50,58,59]. Coimmunoprecipitation experiments revealed that IFI16 forms complexes with STING and promotes the recruitment and activation of Tank-binding kinase 1 (TBK1). A model was proposed, in which IFI16 filaments recruit STING and TBK1, resulting in the phosphorylation of STING (at serine 366 in humans and 365 in mice). The phosphorylation of STING induces the recruitment of IFN-regulating

factor 3 (IRF3) and its phosphorylation via TBK1. The activation of IRF3 transcription factor results in IFN type I production [60,61].

The sensor cGAS binds to DNA in the cytoplasm and catalyzes the synthesis of cyclic guanosine-adenosine di-phosphate, 2′3′-Cyclic guanosine monophosphate–adenosine monophosphate (2′3′-cGAMP) [62]. The dinucleotide 2′3′-cGAMP binds to STING, which is then translocated to perinuclear areas where it interacts with TBK1 and the signaling proceeds as described for IFI16, resulting in the production of IFN type I.

We hypothesized that MPyV genomes could be sensed by DNA sensors either at early times postentry when the virus transported in endosomes is released into the cytosol to be imported to the nucleus or, alternatively, later after infection when the viral DNA replicates in the cell nucleus. In this study, we have shown that the MPyV virus is hidden from innate immune system recognition at early postinfection times. Nevertheless, viral DNA genomes are sensed during replication in the nucleus. MPyV genomes are sensed by p204 in the nucleus, while in the cytoplasm, viral DNA leaked from the nucleus and micronucleus-like bodies (which increase in incidence with the progress of infection) are sensed by cGAS.

Results

Interferon response is detected at late stages of the MPyV infection cycle

Interferon response to DNA occurs extremely rapidly. Previously, it has been described that mouse fibroblasts already produce an abundance of IFN beta (IFN-β) at 2 h after DNA transfection. In addition, murine skeletal myoblasts were also shown to produce IFN-β at 4 h after DNA transfection [63,64]. To study whether MPyV induced an IFN response in its natural host and to evaluate the possible time when the response was induced, we followed the expression of *IFN*-β and the IFN-regulated gene *MX-1* by qPCR in mouse fibroblasts (3T6 cells) within the time interval of 5–30 hpi. Representative experiments are displayed in the graphs in Fig. 1. Using five multiplicity of infection (MOI; Fig. 1A) and MOI 30 (Fig. 1B), we detected the upregulation of IFN-β mRNA in the cells from 24 hpi, with an increase at 30 hpi. In addition, significant upregulation of MX Dynamin Like GTPase 1 (MX-1) mRNA was detected at 30 hpi in both MOI 5- (Fig. 1A) and MOI 30-infected cells (Fig. 1B). Interestingly, at 30 hpi, the levels of IFN-β and MX-1 mRNA were higher in cells infected with a higher MOI (sevenfold for IFN-β and twofold for MX-1). Our data suggested that the main IFN response was launched at late postinfection times when viral DNA replication occurs and that the strength of the IFN response was dependent on MOI.

We noticed that the strength of IFN response induced by MPyV, in cells infected with MPyV MOI 30, was low when compared with responses obtained previously in mouse fibroblasts transfected with plasmid DNA (pDNA) [63]. To verify this, we exposed 3T6 cells to different stimuli, such as pDNA, CpG, dinucleotides, polyinosinic:polycytidylic acid (poly (I:C)), or 2′3′-cGAMP (Fig. 1C,D), for the indicated times (described in Materials and methods), and we measured the expression of *IFN*-β and *MX-1* genes by qPCR. The results are presented in Fig. 1C,D. We observed that 3T6 fibroblasts stimulated with pDNA or other stimuli upregulated the IFN-β mRNA by 4000- to 80 000-fold. In contrast, for MPyV infection at MOI 30 (Fig. 1B), IFN-β mRNA was upregulated only by approximately 300-fold. The levels of MX-1 mRNA differed based on the stimulus applied, but were, in some cases, comparable with those induced by MPyV. The data suggested that the induction of *IFN*-β gene expression in response to MPyV infection was moderate in comparison with the responses induced by pDNA or other stimuli, whereas the regulation of the IFN-inducible *MX*-1 gene appears to be tightly controlled in 3T6 cells.

Interferon response to MPyV infection is dependent on the activation of STING and IRF3 proteins

Next, we focused on signaling related to the IFN response. We followed the time of activation (by phosphorylation) of IRF3, an essential transcription factor for *IFN*-β gene regulation. In addition, we also followed the phosphorylation of STING, a protein described as mediator of the IFN type I production in response to pathogenic intracellular DNA and a variety of intracellular pathogens. By western blotting, we detected the phosphorylation of both STING and IRF3 at 24 hpi (Fig. 2A). At 18 hpi, we did not detect phospho-STING or phospho-IRF3; thus, we concluded that activation occurred within 18–24 hpi. Accordingly, confocal microscopy images of the cell sections revealed phosphorylated STING (green) as patches in the cytoplasm of cells at 24 hpi, but not in the control (mock-infected) cells (Fig. 2B). These results suggested that MPyV is recognized by the immune system late postinfection and that the viral nucleic acids were likely to be first sensed in the nucleus during viral DNA replication.

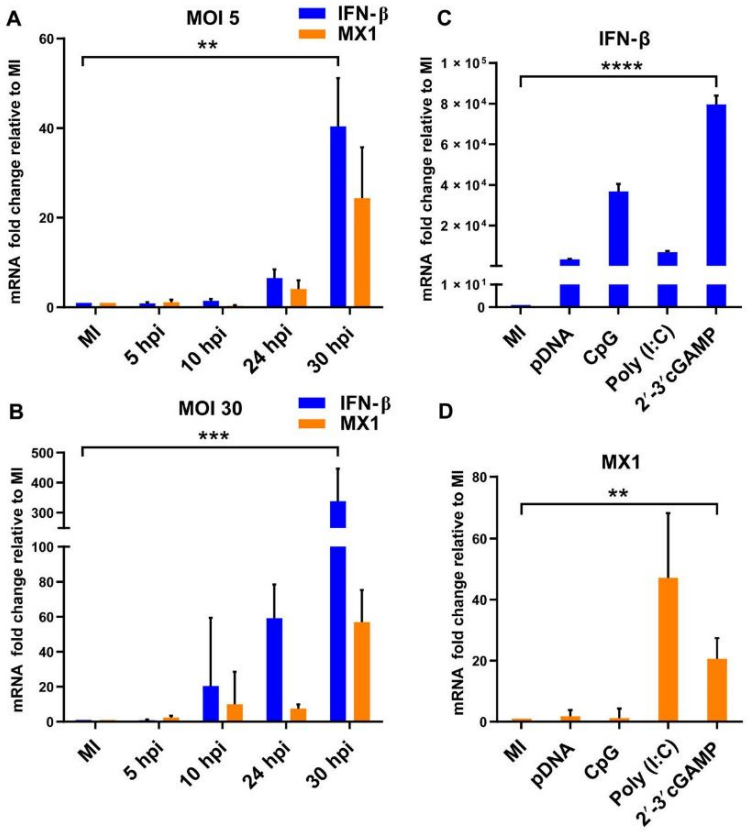

Fig. 1. Kinetics of the IFN response during MPyV infection. (A, B) Mouse 3T6 fibroblasts were infected with MPyV at 5 MOI (A) or 30 MOI (B). After 5, 10, 24, and 30 hpi, the cells were collected, and RNA was isolated. (C, D) 3T6 cells were stimulated with pDNA, CpG, poly (I:C), or 2′3′-cGAMP and collected at the indicated times (described in Materials and methods) for RNA isolation. For all samples (A–D), the levels of IFN-β and MX-1 RNAs were detected by qPCR and normalized to the GAPDH mRNA levels. The displayed data correspond to one representative experiment from at least three independent repeats (each experiment was performed with a different viral stock), and the presented values correspond to the mean of biological triplicate ± SD. Selected data were compared using Student's *t*-test. Asterisks indicate *P*-values representing statistically significant differences. For (A) IFN-β, $^{**}P = 0.0024$; for (B) IFN-β, $^{***}P = 0.0007$; for (C) IFN-β, $^{****}P = 0.0001$ and (D) MX-1, $^{**}P = 0.0074$. For the experiments, mock-infected cells (MI) were used as the control.

To determine the influence of STING on the signaling leading to IFN-β production during MPyV infection, we used a MEF-STING knockout (MEF-STING KO) and parental MEF-STING wild-type (wt) cell lines. We first confirmed the absence of STING protein in the KO cells by immunoblotting (Fig. 2C, upper western blot). Next, we analyzed IRF3 activation in response to MPyV in the KO cells. The phosphorylated IRF3 isoform was not detected in the infected MEF-STING KO cells, but was abundant in the infected MEF-STING wt cells (Fig. 2C, lower western blot). We then followed the IFN response by qPCR (Fig. 2D) and found that there was no upregulation of *IFN-β* or *MX-1* gene expression in the MEF-STING KO cells (Fig. 2D). In contrast, the MEF-STING wt cells responded to MPyV infection by increasing levels of INF-β (188-fold) and MX-1 (48-fold) mRNAs. To characterize the ability of MEF-STING KO cells to respond to other stimuli, such as RNA, the cells were treated with poly (I:C). We followed the levels of phosphorylated IRF3 by western blotting (Fig. 2E) and IFN mRNA levels by qPCR (Fig. 2F). We found that MEF-STING KO cells could activate IRF3 and induce *IFN-β* and *MX-1* gene expression when stimulated by RNA. Thus, our results showed that STING protein is essential for the induction of the IFN-β response during MPyV infection. Given that STING and IRF3 are phosphorylated in the same time frame during MPyV infection (Fig. 2A) and that STING KO cells do not activate IRF3 in response to MPyV infection (Fig. 2C), this provides support for the model in which activated STING promotes the recruitment of IRF3 to TBK1 active sites [61].

The presence of MPyV genomes in the cell nucleus is crucial for the induction of the interferon response

To further confirm the essential role of late (nuclear) phases of MPyV infection in the DNA sensing in contrast to the early phase, when the virus travels undetected by sensors in endosomes (Fig. 1), we used a mutated MPyV that was unable to translocate efficiently to the cell nucleus (a mutant previously constructed and

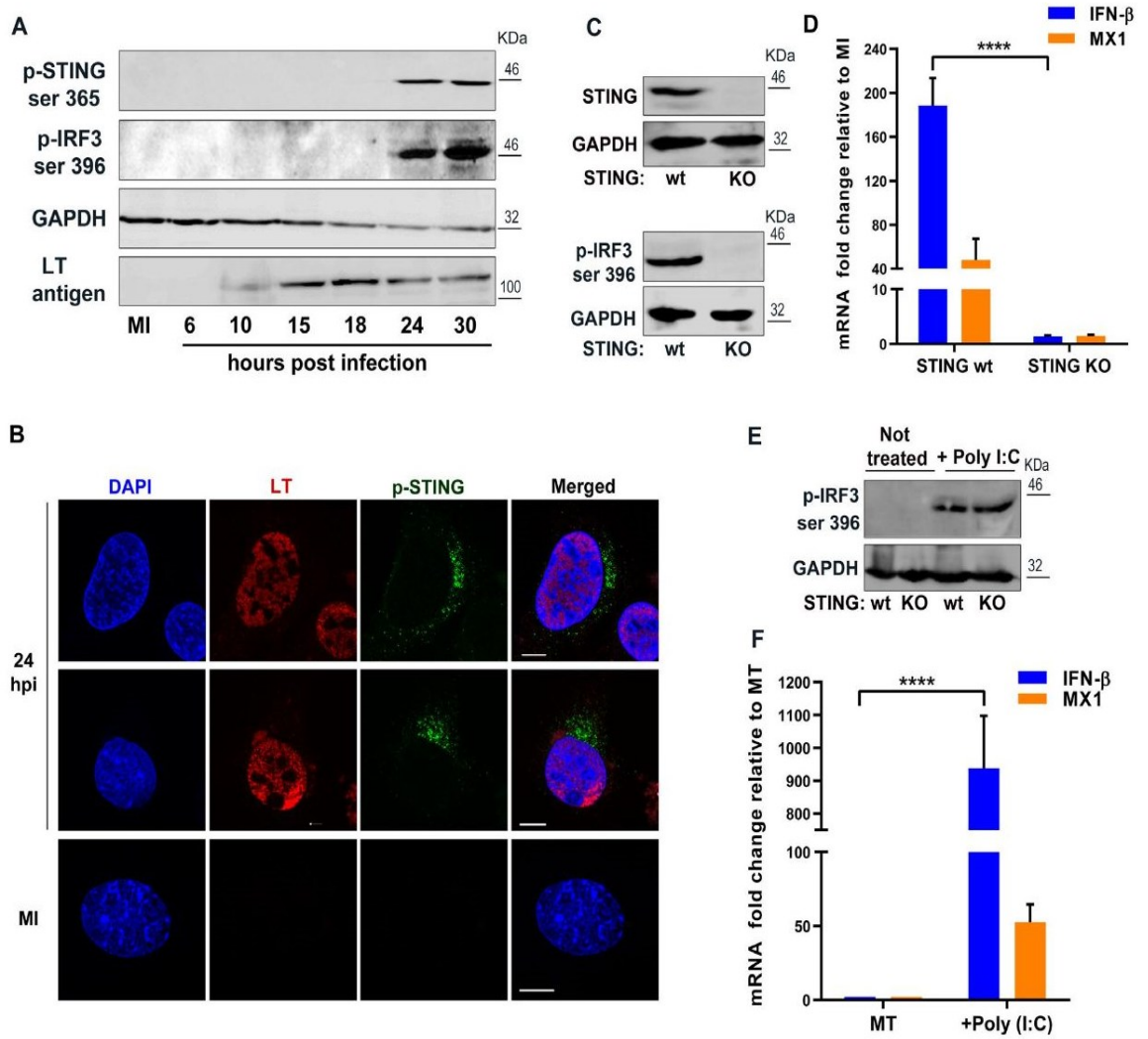

Fig. 2. STING and IRF3 are involved in the IFN response induced by MPyV. (A) Mouse 3T6 fibroblasts were infected with MPyV (MOI = 10). At the indicated times, cell lysates were prepared and phospho-IRF3 (p-IRF3), phospho-STING (p-STING), or GAPDH and LT antigen as controls, were detected by western blotting. (B) Mouse 3T6 fibroblasts were either mock-infected (MI) or infected with MPyV (MOI = 3), fixed at 24 hpi, and stained by DAPI (blue) and by antibodies directed to MPyV early LT antigen (red) and phospho-STING (p-STING; green). Confocal microscopy images of representative cell sections are presented. Bars = 10 μm. (C) MEF-STING KO or STING wt cells were infected with MPyV (MOI = 20) and the cell lysates were prepared at 30 hpi. The samples were analyzed by western blotting for the presence of STING, phospho-IRF3 (p-IRF3), and GAPDH as a loading control. (D) MEF-STING KO and STING wt cells were mock-infected or infected with MPyV (MOI = 20). At 30 hpi, RNA was isolated and subjected to qPCR for quantification of IFN-β, MX-1and GAPDH mRNAs, with values normalized to the transcripts in the mock-infected cells (MI). (E, F) MEF-STING KO or STING wt cells were treated with poly (I:C) (+) or not treated (MT) and cells were collected after 16 h. Cell lysates were prepared and the presence of phospho-IRF3 (p-IFR3) and GAPDH (as a loading control) was followed by western blotting (E). RNA was isolated and the IFN-β, MX-1, and GAPDH mRNA levels were quantified by qPCR (F). For (A), (C), and (E), each of the presented western blots is representative of at least two independent experiments. For (D) and (F), the presented data correspond to the mean values of three independent experiments; the corresponding SD values are presented. Selected data were compared using Student's *t*-test. Asterisks indicate *P*-values representing statistically significant differences. For (D) IFN-β, ****$P = 0.0001$ for (F) IFN-β, ****$P = 0.0001$.

characterized in our laboratory) [23]. The virus mutant that lacks the NLS of the structural proteins enters cells efficiently and can be released, similar to the wt virus, into the cytosol after its trafficking to ER. However, because of the lack of NLS, the virus exhibits defective nuclear entry via nucleopores and its infectivity is decreased by 80%. Here, stocks of the mutated virus were produced after transfection of the mutated

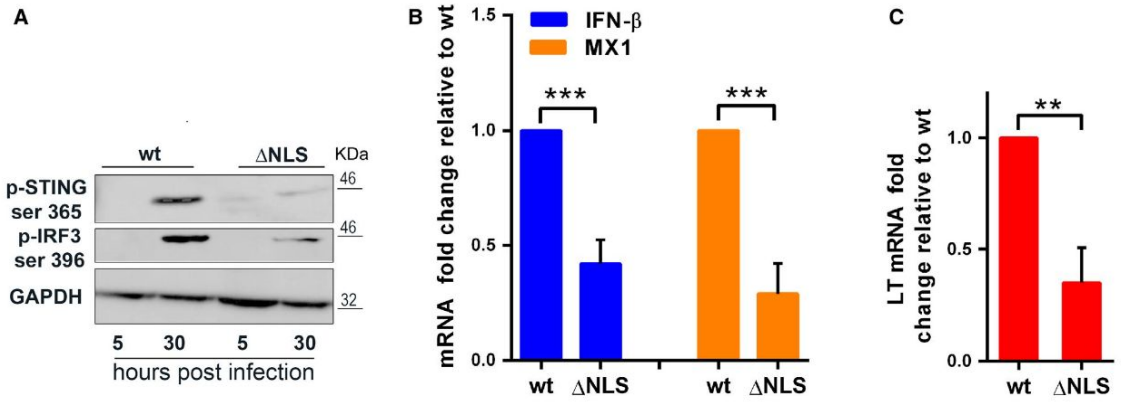

Fig. 3. IFN response in MPyV-infected cells is strongly dependent on the presence of viral genomes in the cell nucleus. 3T6 fibroblasts were infected with MPyV-wt (wt) or MPyV-mutated in NLS (Δ NLS) with MOI corresponding to 200 genomes per cell, as quantified by qPCR. The cells were collected at 5 or 30 hpi for the preparation of cell lysates and 30 hpi for isolation of RNA. (A) Cell lysates were subjected to western blotting and assayed for phospho-IRF3 (p-IRF3), phospho-STING (p-STING), and GAPDH. The western blot shown is representative of two experiments. (B) RNAs were isolated and the mRNA for IFN-β, MX-1 (B), or for LT (C) were measured by qPCR. For (B) and (C), the presented data correspond to mean values of three independent experiments (performed with three different viral stocks); the corresponding SD values are presented. For each experiment, the values were normalized to those of wt virus. The data were compared using Student's *t*-test. Asterisks indicate *P*-values representing statistically significant differences (IFN-β, $***P = 0.0006$; MX-1, $***P = 0.0007$; LT, $**P = 0.0021$).

genomes. In the same way, wt MPyV was prepared as a control. We followed the IFN response (as described previously) and the levels of infection by measuring LT viral antigen production. The western blot (Fig. 3A) revealed that IRF3 and STING phosphorylated proteins were markedly lower in the cells infected with NLS mutant virus compared with that in wt MPyV-infected cells. In agreement, we found the expression of the IFN-related genes significantly decreased in the cells infected with the NLS mutant virus. Specifically, the levels of IFN-β mRNA decreased by 60% and the levels of MX-1 mRNA decreased by 70% (Fig. 3B). Accordingly, lower expression of LT antigen (by 70%) was observed in the cells infected with the NLS mutant virus compared with that of cells infected with the wt virus (Fig. 3C). These results strongly support the above observation that IFN induction is associated with the late phase of infection, in which viral genomes replicate in the cell nucleus.

The DNA sensor p204 is involved in *IFN*-β induction during MPyV infection

Previously, human herpesvirus was shown to be sensed in the nucleus by the innate immune DNA sensor, IFI16. We hypothesized that the mouse protein related to IFI16 protein, p204, could sense MPyV DNA in the nucleus during viral genome replication. To test the involvement of p204 in the induction of IFN by MPyV, we followed the IFN response in cells with downregulated p204. For this, we used small interfering RNAs (siRNAs) against p204 (si-p204) or random siRNA as the control. Knockdown efficiency was confirmed by western blotting (Fig. 4A). The levels of p204 decreased approximately by 60% in the cells treated with si-p204 in comparison with those in untreated cells or cells treated with random siRNA. The effect of p204 knockdown on *IFN*-β and *MX-1* transcription was assessed by RT-qPCR. The results (Fig. 4B) showed that both IFN-β and MX-1 mRNA levels were significantly reduced (by 65% and 55%, respectively) in the p204-knockdown cells compared with the nonsilenced control cells. Finally, a substantial decrease (by 47%) of activated IRF3 in p204-knockdown cells was estimated from phospho-IRF3 and GAPDH band densities on the western blot (Fig. 4C). To better understand the mechanism of p204 activation, we assessed the localization of p204 and replicating MPyV genomes in infected cells by confocal microscopy. For that, we labeled MPyV genomes by fluorescence *in situ* hybridization (FISH), p204 by a specific antibody, and whole DNA by 4′,6′-diamidino-2-phenylindole (DAPI). Using a standard fixation protocol, p204 was spread throughout the nucleus and clear colocalization with MPyV genomes was observed only sporadically (data not shown). To uncover interaction between viral

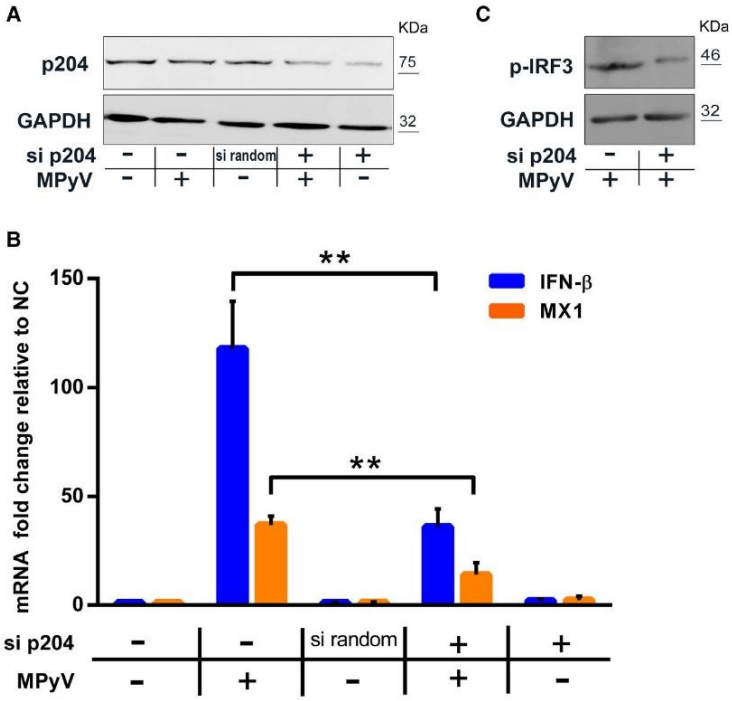

Fig. 4. p204 plays a role in IFN induction by MPyV infection. (A–C) Mouse 3T6 fibroblast cells were transfected with p204 siRNA. Random siRNA transfection or untransfected cells were used as the control. After 48 h, the cells were infected with MOI = 20 or mock-infected and incubated for 30 h. (A) A representative western blot (of the three prepared) is presented. (B) IFN-β or MX-1 mRNA levels were measured by qPCR. The values were normalized to GAPDH mRNA levels. The data presented correspond to mean values of three independent experiments; the corresponding SD values are presented. Samples were compared by Student's *t*-test. Asterisks indicate *P*-values representing statistically significant differences (IFN-β, $^{**}P = 0.0053$; MX1, $^{**}P = 0.0064$). (C) Cell lysates were prepared and subjected to immunoblotting for evaluation of the levels of phospho-IRF3 (p-IRF3) and GAPDH. A representative western blot (of the three prepared) is presented.

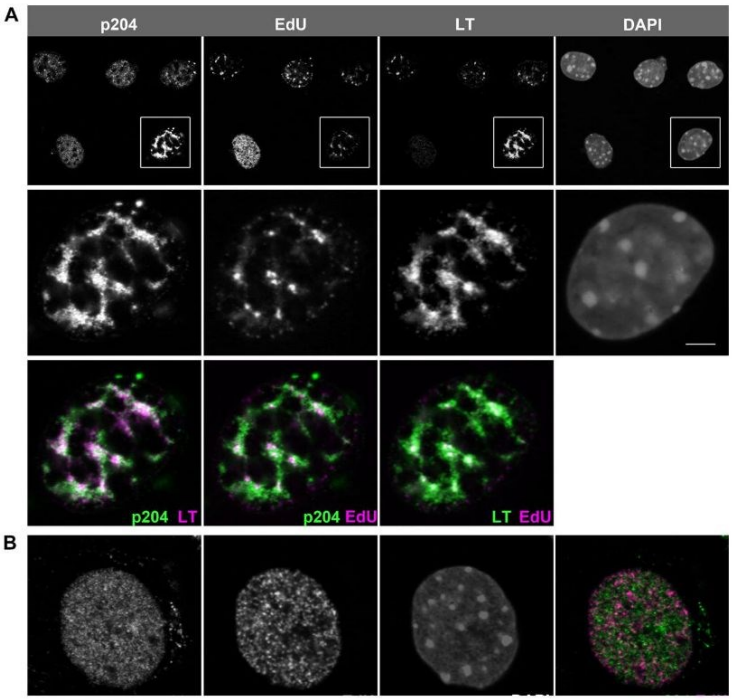

Fig. 5. p204 accumulates in areas of MPyV DNA replication. MEF cells were infected with MPyV (MOI = 5) (A) or mock-infected (B) and incubated for 24 h. EdU was added for the last 30 min of incubation. Then, cells were treated for 5 min with pre-extraction buffer and fixed. For immunofluorescence, cells were stained with anti-p204 (green) and anti-MPyV LT (far red, displayed as magenta or green) antibodies. EdU was visualized by the Click-iT EdU reaction (red, displayed as magenta) and DNA was stained by DAPI (displayed as white). Representative confocal cell sections were analyzed. Scale bar = 5 μm.

DNA and p204, the cells were stained using a protocol including prefixation permeabilization (using a pre-extraction buffer) [65]. Replicating genomes were labeled by EdU and the p204 protein and viral LT antigen were detected by using specific antibodies. We found that p204 accumulated in the areas of replication/transcription of viral genomes where it markedly colocalized with EdU-labeled replicating viral genomes and

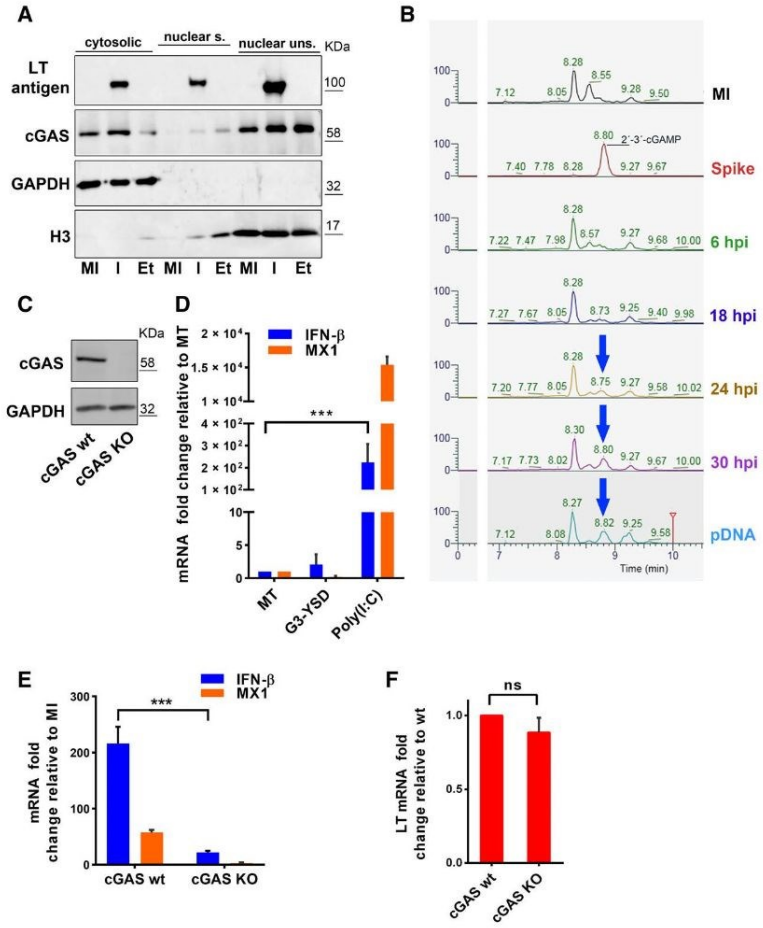

Fig. 6. cGAS is activated during MPyV infection. (A) Mouse 3T6 fibroblasts were mock-infected (MI) or infected (I) with MPyV (MOI = 3) for 24 h or treated with etoposide (Et) for 6 h. Then, the cells were collected and subjected to subcellular fractionation. The fractions [cytosolic and nuclear-soluble (s), and nuclear-insoluble (ins)] were immunoblotted and stained with antibodies against cGAS or, as controls, against GAPDH, Histone 3 (H3), or LT. (B) Mouse 3T6 fibroblasts were infected with MPyV (MOI = 5), and at the indicated times, dinucleotides were extracted from the cells, and samples were analyzed by LC-MS for detection of 2′3′-cGAMP. Mock-infected cells or cells transfected were included as controls. In addition, an internal control of commercial 2′3′-cGAMP was spiked into the lysate of mock-infected cells. Specific transitions for 2′3′-cGAMP (675.1 > 136.1, 675.1 > 524.1, 675.1 > 312.1, 675.1 > 506.0, 675.1 > 152.1, 675.1 > 476.0, 675.1 > 330.0) were used to detect 2′3′-cGAMP. In the graph, transition 506.0 is shown. 2′3′-cGAMP (retention time: 8.75–8.82 min) is shown in the spike and indicated by arrows in the samples when present. (C) MEF-cGAS KO or wt MEF were cultivated for 24 h, and the cell lysates were prepared and subjected to western blotting for detection of cGAS. GADPH was detected as the control. (D) MEF-cGAS KO cells were either mock-transfected (MT) or transfected with 26-mer DNA (G3-YSD) or with poly (I:C). After 16 h, the cells were collected, and RNA was isolated. IFN-β, MX-1, and GAPDH mRNA levels were quantified by qPCR. (E, F) MEF-cGAS KO and cGAS wt cells were infected with MPyV (MOI = 5) and incubated for 30 h before collection for RNA preparation. RNAs were isolated and used to measure IFN-β, MX-1 (E), and LT (F) mRNA levels by qPCR. (D–F) The data presented correspond to mean values of three independent experiments; the corresponding SD values are presented. Selected data were compared using Student's *t*-test. Asterisks indicate *P*-values representing statistically significant differences. For (D) IFN-β, ***$P = 0.0004$; for (E) IFN-β, ***$P = 0.0002$; for (F) the *P*-value obtained did not show statistically significant differences, denoted as ns, $P = 0.0807$.

LT antigen (Fig. 5A). In mock-infected cells (Fig. 5B), p204 was distributed throughout the nucleus in distinct dots that, in part, overlapped with EdU-labeled replicating cellular DNA (Fig. 5B). Collectively, our results showed that p204 was involved in the induction of IFN response by MPyV and indicated that p204 became activated in the cell nucleus. However, to uncover the detailed role of p204, further research is required.

The DNA sensor cGAS is essential for IFN-β production in MPyV-infected cells

Although described as a cytosolic sensor, cGAS is located not only in the cytoplasm but also in the cell nucleus. During DNA transfection, both IFI16 and cGAS sense DNA independently. In contrast, during herpesvirus infection, cGAS was found to bind to IFI16, promoting its stability by preventing its degradation [57]. Therefore, we assessed whether cGAS participated in the IFN response induced by MPyV.

First, we followed the subcellular localization of cGAS in infected cells by cell fractionation. As controls, we also fractionated noninfected cells and noninfected cells treated with etoposide. Etoposide, upon forming a ternary complex with DNA and topoisomerase II, causes breaks in dsDNA. It has been shown that upon DNA damage, cytosolic cGAS translocates to the nucleus [46]. The cells were fractionated into three fractions: cytosolic, nuclear-soluble, and nuclear-insoluble, and we detected cGAS by western blotting (Fig. 6A). We found that during infection, as well as in uninfected cells, cGAS was found in both the nuclear-insoluble fraction and the cytosolic fraction. In contrast with cells treated with etoposide, we did not observe significant mobilization of the cytoplasmic cGAS pool to the nucleus.

As the activation of cGAS in response to DNA binding results in the production of 2′3′-cGAMP, we followed the production of the dinucleotide during infection by liquid chromatography-mass spectrometry (LC-MS). Infected or mock-infected 3T6 cells were harvested from 6 to 30 hpi and processed for the detection of 2′3′-cGAMP. We first detected 2′3′-cGAMP at 24 hpi and its synthesis has increased substantially by 30 hpi (Fig. 6B).

To determine whether cGAS activation had any effect on the induction of IFN expression by MPyV, we analyzed IFN responses in MEF-cGAS KO or MEF-cGAS wt cells. First, we verified the knockout of cGAS by western blotting (Fig. 6C). Next, we performed an additional control, to confirm that the cGAS KO cells responded to RNA but did not respond to DNA stimulus via cGAS. To achieve this, we transfected the cells with either poly (I:C) or with the cGAS agonist G3-YSD. G3-YSD is a 26-mer DNA sequence derived from the HIV-1 RNA genome, which has a Y-shape owing to a palindromic sequence flanked by unpaired guanosine trimers. This DNA sequence has been identified as a minimal recognition motif required for cGAS activation. After measurement of the mRNA levels by qPCR, we found that in the MEF-cGAS KO cells, poly (I:C) induced the upregulation of *IFN-β* and *MX-1* whereas G3-YSD did not induce an IFN response (Fig. 6D). Next, we used qPCR to measure the levels of IFN-β and MX-1 mRNA in MPyV-infected MEF-cGAS KO or MEF-cGAS wt cells (Fig. 6E,F). In cGAS KO cells, the IFN-β mRNA levels were dramatically lower (by ninefold) than in MEF-cGAS wt cells. Accordingly, while high production of MX-1 mRNA was induced in MEF-cGAS wt cells, almost no detectable mRNA production was observed at the same time postinfection in cGAS KO cells. As an infection control sample, we measured the levels of mRNA of LT antigen in the MEF-cGAS KO and MEF-cGAS wt cells and found no significant difference. Our results showed that there was a particularly important contribution from cGAS activation in the IFN response induced by MPyV. Nevertheless, it is important to highlight that the IFN response is not completely abolished by the absence of cGAS. Thus, we can conclude that at least two mechanisms are activated in parallel during MPyV infection: viral genome sensing by p204 and activation of cGAS.

cGAS senses DNA leaked from the nucleus to cytoplasm and micronucleus-like bodies

Further, we addressed the question of whether cGAS participated in IFN induction by MPyV through sensing of viral DNA in the nucleus, as recently described [44], or if there are other mechanisms that lead to cGAS activation. Using confocal microscopy, we followed whether cGAS present in the nucleus had an affinity for replicating MPyV genomes. To achieve this, mouse fibroblasts expressing cGAS-EGFP were prepared and infected with MPyV. Then, cells were subjected to FISH using sequences of the MPyV genome as a probe (Fig. 7). Surprisingly, we found colocalization of viral DNA with cGAS in different subcellular compartments. We observed strong colocalization of cGAS with viral DNA probably leaked from the nucleus to the cytosol in a subpopulation of cells (Fig. 7A–C). Further, in a subpopulation of cells, the cGAS signal overlapped with MPyV genomes in the

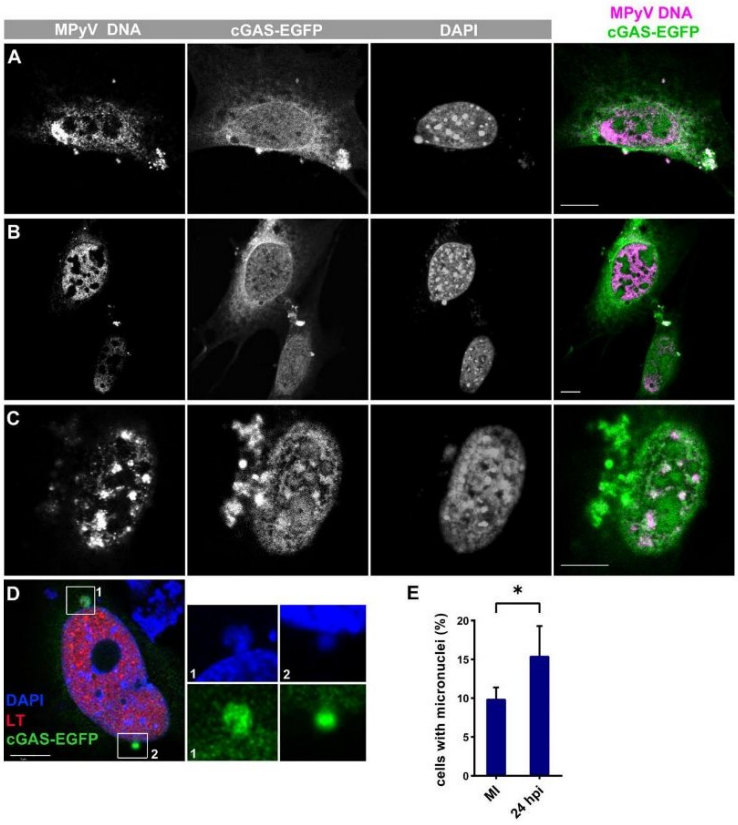

Fig. 7. cGAS colocalizes with MPyV genomes and micronucleus-like bodies. (A–D) 3T6 cells expressing GFP-cGAS were infected with MPyV (MOI = 3) and fixed at 24 hpi. (A–C) Cells were stained with antiGFP (green) to enhance the signal, and then subjected to FISH with MPyV DNA probe labeled with biotin, followed by staining with anti-biotin antibody (magenta). Confocal sections of the cells displaying colocalization of GFP-cGAS with MPyV genomes are presented. Bars = 10 μm. (D) Cells were stained with anti-LT antibody (red), cGAS-EGFP was visualized by anti-GFP (green), and DNA was labeled by DAPI staining. Confocal sections of the cells displaying micronucleus-like structures colocalizing with GFP-cGAS are presented. Bars = 10 μm. (E) Mouse fibroblasts infected at MOI 3 or mock-infected were fixed at 24 hpi and DNA was labeled by DAPI staining. The cells were scored for the presence of micronucleus-like bodies; the results are summarized in the graph. The data presented correspond to mean values of three independent experiments (At least 250 cells in each experiment were examined); the corresponding SD values are presented. Student's *t*-test was performed. Asterisks indicate *P*-values representing statistically significant differences (**P* = 0.0152).

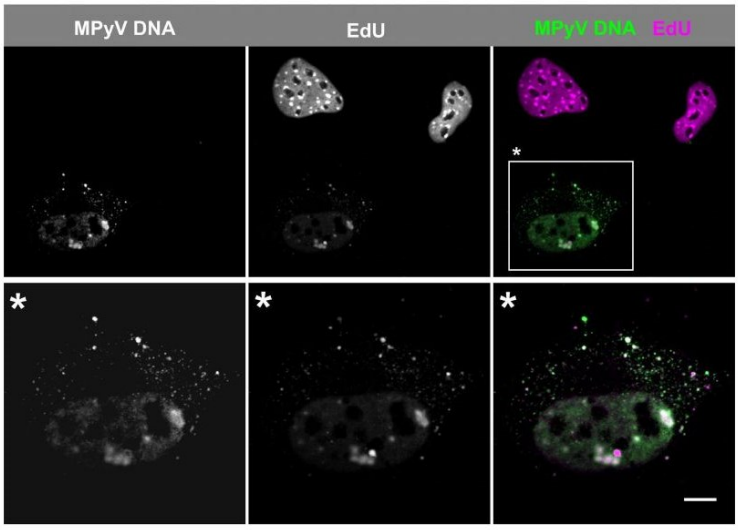

Fig. 8. Leakage of DNA to cytosol during MPyV infection. MEF cells were infected with MPyV (MOI = 3) in presence of EdU. After 24 h, the cells were fixed, the Click-iT EdU reaction was performed, and the cells were used for FISH with MPyV DNA probe labeled with biotin and detected with anti-biotin antibody. Representative confocal section of cells displaying EdU DNA (magenta) and viral DNA (green). A white asterisk is used to highlight the infected cell among the uninfected ones. Bar = 5 μm.

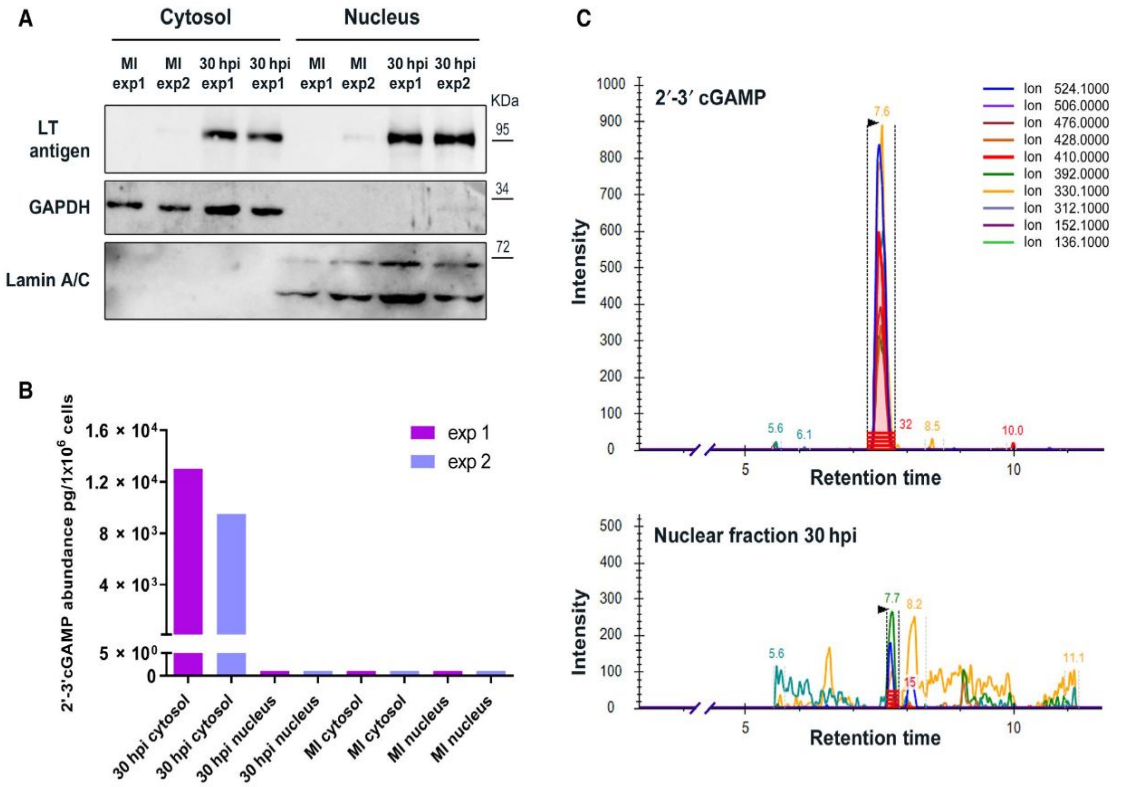

Fig. 9. 2′3′-cGAMP is detected only in the cytosolic fraction of infected cells. Mouse fibroblasts were infected with MPyV at MOI 5 or mock-infected (MI). After 30 h, the cells were fractionated. Two independent experiments were performed (A) The fractions were verified by western blotting using antibodies against lamin A/C for the nuclear fractions, GAPDH for the cytosolic fraction, and LT (to verify infectivity). One of two representative experiments is displayed. (B) The cell fractions were used for detection of 2′3′-cGAMP by competitive ELISA. Standards were prepared in the cell lysis buffers. Two independent experiments are displayed (exp1 and exp2). (C) Nuclear fractions were analyzed by LC-MS. Specific transitions for 2′3′-cGAMP (675.1 > 136.1, 675.1 > 524.1, 675.1 > 312.1, 675.1 > 506.0, 675.1 > 152.1, 675.1 > 476.0, 675.1 > 330.0) were used to detect 2′3′-Cgamp. One of two representative experiments is displayed. As the spike, commercial 2′3′-cGAMP was used.

nucleus (Fig. 7C) and, unexpectedly, we also found micronucleus-like bodies loaded with cGAS (Fig. 7D).

Next, we compared the number of micronucleus-like bodies in mock-infected and infected cells at the time postinfection when IFN induction became detectable. For this experiment, we used cells not overexpressing cGAS to exclude any effect of the overexpression on the formation of micronucleus-like bodies. MPyV-infected or mock-infected cells were fixed and subjected to DAPI staining; then, using confocal microscopy, micronucleus-like bodies were counted. Although we observed micronucleus-like bodies in both infected and mock-infected cells, the total number of micronucleus-like bodies in infected cells was significantly higher than in mock-infected cells (Fig. 7E).

To provide a more convincing demonstration that the viral cytosolic DNA detected in infected cells was leaked from the nucleus, we labeled the host and viral replicating DNA with EdU and then performed FISH for detection of MPyV genomes to search for overlapping signals in the cytosol. In detail, EdU was added to the growth medium at the beginning of infection and at 24 hpi click chemistry was used to detect EdU and FISH. As expected, we detected EdU and the MPyV genome signal colocalizing in the cytosol. In addition, only the EdU signal (not colocalized with MPyV genomes) apparently corresponding to leaked host DNA was detected in the cytosol (Fig. 8). Next, to determine whether the interactions of cGAS with MPyV minichromosomes in the cell nucleus resulted in cGAS activation, we analyzed the levels of 2′3′-cGAMP in separated cytosolic and nuclear fractions of infected cells. The separation of nuclear and cytosolic fractions was verified by western blotting (Fig. 9A) and the fractions were examined for 2′3′-cGAMP by competitive ELISA (Fig. 9B). We found an abundance

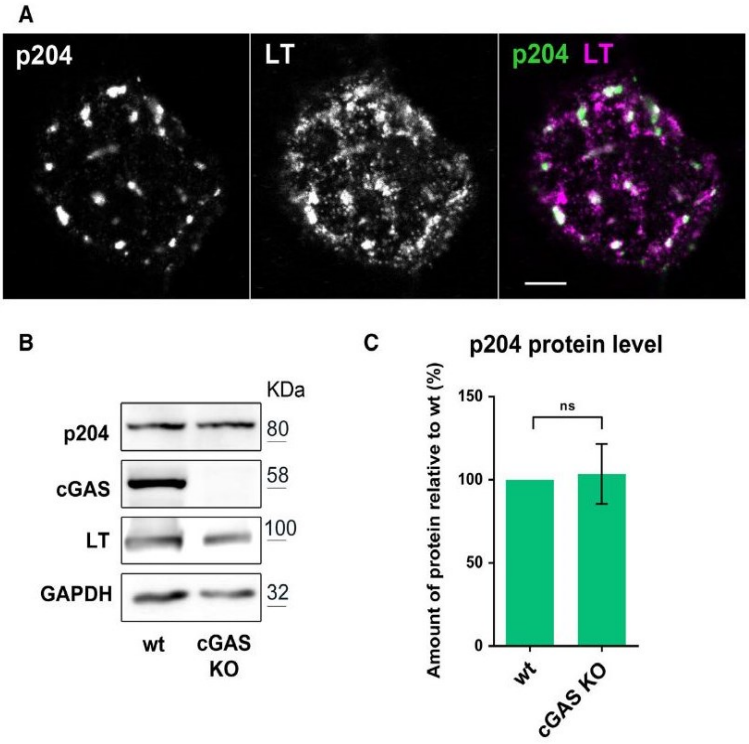

Fig. 10. Absence of cGAS did not affect either the interaction of p204 with the MPyV genomes or its level in cells. (A) MEF-cGAS KO cells were infected with MPyV (MOI = 3) and incubated for 24 h. The cells were treated for 5 min with pre-extraction buffer and then fixed. Next, the cells were stained with anti-MPyV LT antigen (magenta) and anti-p204 (green) antibodies. The image shows a confocal section of the nucleus of the infected cell. Scale bar = 5 μm. (B, C) MEF wt and cGAS KO cells were infected with MPyV (MOI = 5). At 30 hpi, cell lysates were prepared and analyzed by western blotting to follow the p204 levels. As a control, antibodies against cGAS, GAPDH, and LT antigen were used. Three independent experiments were performed (B). The graph represents comparison of levels of p204 (related to levels of GAPDH loading controls) in MEF-cGAS wt and MEF-cGAS KO cell lysates. The data presented correspond to mean values of three independent experiments; the corresponding SD values are presented. Student's *t*-test was performed. The *P*-value obtained did not show statistically significant differences, denoted as ns, $P = 0.85$ (C).

of 2′3′-cGAMP in the cytosolic fraction of infected cells. However, we did not detect any 2′3′-cGAMP in the nuclear fractions of infected cells, similar to all fractions of control (uninfected) cells. To confirm the absence of 2′3′-cGAMP in the nuclear fractions of infected cells by a second method, we analyzed the samples by LC-MS. A representative chromatogram of the nuclear fraction of infected cells is shown in Fig. 9C: 2′3′-cGAMP was not detected in the nuclear fractions; only traces of a dinucleotide with different spectra were found.

Our results strongly suggest that cGAS senses viral DNA present in the cytosol but is not activated in the nucleus of MPyV-infected cells. Colocalization of cGAS with viral genomes in the nucleus may represent an additional role of the nuclear cGAS independent of its activation. However, the activation of cGAS in the cytosol reflects its interactions not only with viral or cellular DNA leaked from the nucleus, but also with micronucleus-like bodies formed by genotoxic stress induced by the infection.

Absence of cGAS does not affect the interaction of p204 with MPyV genomes in the cell nucleus or the levels of p204

As the ability of cGAS to degrade IFI16 on the genomes of herpesviruses in the nucleus has been reported [57], we investigated whether cGAS had similar effects on p204 in MPyV infection. First, we assessed whether cGAS absence affects the colocalization of p204 with viral genome replication sites. To achieve this, we used confocal microscopy to examine the colocalization of p204 with LT viral antigen in cGAS KO cells (Fig. 10A). We found that p204 protein could be preferentially seen in LT spots, similar to infected wt cells (Fig. 5A). Thus, our results indicated that the absence of cGAS did not impair p204 localization on viral

DNA replication areas. In addition, we examined the possible contribution of cGAS to the prevention of fast turnover of p204. Therefore, we examined the levels of p204 protein in MPyV-infected cGAS KO and wt cells by western blotting. We found that at 30 hpi, the levels of p204 in lysates of both cell lines were comparable, regardless of the presence or absence of cGAS (Fig. 10B,C). The above results showed that cGAS did not stabilize p204 on viral genomes and suggested that the sensing of MPyV genomes by both DNA sensors occurs simultaneously, but independently.

Discussion

Nucleic acids of pathogens can be recognized through pattern recognition receptors by host cells. This leads to production of IFN and other hundreds of proteins with antiviral effects. In the past decade, many sensors of invading nucleic acids have been described and an understanding of the molecular bases of DNA and RNA immune recognition has emerged. Genomes of herpes simplex virus-1, kaposi's sarcoma-associated herpesvirus, vaccinia virus, murine gamma herpesvirus 68, adenovirus, hepatitis B virus, and HIV (reviewed in [66]) have been shown to be recognized by specific nucleic acid sensors. We therefore aimed to determine whether small DNA viruses, such as polyomaviruses, which travel to the nucleus in endosomal compartments and have genomes organized into minichromosomes, are recognized by host DNA sensors. We focused on the possible interactions between MPyV genomes and host DNA sensors, p204 (closely related to human IFI16) and cGAS. We found that regardless of the MOI, a moderate IFN response was launched not sooner than the late phase of infection (approximately 24 h), at the time when genome replication occurs.

The absence of IFN induction at early times postinfection suggests that the virus is hidden or invisible for the immune system when sorted through the endosomal system to ER. Although virions, partially disassembled in the ER, appear in the cytosol prior to their importin-mediated transfer to the nucleus [23], their genomes remain inaccessible to interaction with cytosolic DNA sensors for several reasons. At first, genomic DNA in polyomavirus virions is tightly packed in the form of a nucleocore condensed with cellular histones (except H1) and the capsid protein VP1, making it inaccessible to other protein interactions. Indeed, studies of polyomavirus have suggested that the release of the nucleocore into relaxed minichromosomes with nucleosomes occurs in the cell nucleus [67]. Subsequently, depending on cell type, only small fractions of internalized virions travel by productive endocytic pathway to the ER and then are released into the cytosol [19,23]. Substantial portions of virions remain in late recycling endosomes from where they exit cells and in endolysosomal compartments where they are subject to degradation. Moreover, in the cytosol, viruses can be degraded by proteosomes and any DNA released from proteasomes is probably degraded rapidly by exonuclease TREX-1 (which can degrade dsDNA). The activation of proteasomal systems during BK polyomavirus infection has been documented [68] and genomes of herpesvirus present in the cytosol or HIV reverse transcripts were degraded by TREX-1 [69,70]. All these previous observations account for the absence of IFN induction during transport of the virus into the nucleus and are in agreement with observed poor IFN response induced by the mutant virus with impaired ability to enter the nucleus (Fig. 3).

In the late phase of MPyV infection, replicating and transcribing viral DNA accumulate in the cell nucleus. The induction of IFN response at this time suggested the involvement of a nuclear DNA sensors. Therefore, we focused on the p204 protein—the mouse homolog of the human IFI16 protein found to sense herpesvirus DNA genomes in the cell nucleus. The ability to sense pathogenic DNA in the nucleus raised questions about the mechanisms preventing self-DNA recognition. IFI16 was found to be excluded from self-DNA recognition by the presence of nucleosomes that impede the one-dimensional movement (scanning) of the protein along DNA. The scanning of DNA allows the clustering of IFI16 required for its activation [45,50,58,59]. Herpesvirus genomes are chromatinized after they enter the nucleus. In addition, the density of nucleosomes is lower, their distribution more irregular, and histone association looser than that of the host DNA [71,72]. Therefore, their genomes are easily sensed by IFI16 in the nucleus [42]. Much smaller polyomavirus genomes are in complex with cellular histones already in virions, and in the nucleus, they function covered by nucleosomes in the form of minichromosomes. We did not expect too significant colocalization of p204 with viral genomes. However, MPyV genomes may overcome the restriction owing to the absence of nucleosomes in the regulatory region that includes sequences for transcription regulation and the ORI [14–16]. Indeed, we revealed that p204 interacts with replicating MPyV genomes (EdU-labeled viral DNA) and with the early viral LT antigen shown to bind the ORI region to promote viral replication. We cannot exclude that during replication, transcription, or repair processes, partial removal of histones from genomes can contribute to p204 sensing.

The activation of p204 during MPyV DNA sensing could involve post-translational modifications and/or

complexation with other molecules. During the recognition of herpesvirus genomes, the formation of a protein complex between IFI16, BRCA1 [DNA damage responses (DDRs) protein], and the histone H2B plays a significant role in IFI16 activation [73,74]. In addition, the acetylation of p204, similar to that described for IFI16 in herpesvirus genome sensing, could also control shuttling of p204 between the cytoplasm and the nucleus during p204 activation [41,56]. Our preliminary results from a proximity ligation assay using antibodies against p204 and acetylated lysine revealed the acetylation of p204 and/or the formation of a complex of p204 and an acetylated protein in the nucleus of infected cells (Data not shown). Further experiments will be needed to determine the molecular mechanism through which the p204 protein activates STING. Efforts to investigate the role of p204 in *IFN*-β gene induction further have been hampered by the unavailability of anti-p204 antibodies applicable for immunoprecipitation experiments. Interestingly, although it has been described that IFI16 can sense pathogenic DNA in both the cytoplasm and the nucleus [32,33,42,45,75], p204 does not seem to contribute to the cytosolic sensing of MPyV genomes. We did not observe high subpopulation of p204 in the cytosol. Some sporadic spots of p204 seen in the cytosol (data not shown) could correspond to the acetylated protein(s) (data not shown) shuttling from the nucleus to the cytosol to activate STING.

Recently, a new noncanonical pathway for IFN induction has been described [76]. In this pathway, ubiquitinylated, but not phosphorylated, STING extensively activates NF-kB and only minimally activates IRF3. The noncanonical pathway is postulated to be induced by dsDNA breaks that recruit p53, IFI16, and TRAF6. In this study, we followed the classical pathway of p204 activation as we found: (a) that massive concomitant STING and IRF3 phosphorylation is induced by MPyV infection and (b) that in p204-knockdown cells, infection by MPyV results in a significant reduction in IFN-β production associated with a marked decrease in IRF3 phosphorylation. Nevertheless, the contribution of noncanonical pathway to the IFN response induced by MPyV needs to be explored. Indeed, DNA damage response is activated during replication of the MPyV genome.

We further investigated involvement of the DNA sensor cGAS in the sensing of MPyV genomes. Using cGAS KO experiments, we demonstrated that cGAS was essential for the induction of IFN response by MPyV. The multiple locations of viral and cellular DNA colocalizing with cGAS was intriguing and surprising. However, we detected production of 2′3′-cGAMP only in the cytosolic fraction and not in the nuclear fractions of infected cells, consistent with most studies confirming cGAS sensing of DNA, its activation, and 2′3′-cGAMP production in the cytosol [77–80]. The production of 2′3′-cGAMP as a result of DNA sensing in the nucleus has been described in only one study. The authors of this study showed that dendritic cells produce low levels of2′3′-cGAMP in response to the overexpression of cGAS fused with the NLS sequence [44]. Our results, despite detection of abundant presence of cGAS in the nucleus and its occasional colocalization with MPyV genomes (Fig. 7C), strongly support the cytosolic sensing of cGAS and underline the existence of a tight regulatory mechanism that prevents sensing of MPyV DNA by cGAS in the nucleus. The binding of cGAS to nucleosomes and post-translational modifications, such as phosphorylation and acetylation, are involved in the prevention of self-DNA sensing [48,53]. The presence of cGAS on the viral genomes can be explained by its engagement in DDRs activated during polyomavirus replication. It was recently shown that cGAS colocalizes with H2AX and PARP1 in sites of DNA ds breaks (DSBs). cGAS binding to the site of DSBs was shown to inhibit homologous recombination repair by disruption of the formation of the PARP1–TIMELESS complex and by preventing the loading of RAD51 [46,81].

An increasing number of studies shows that cGAS and IFI16, besides their direct function in DNA recognition, can interact and affect the activation of STING in the cytosol [43,60]. In the nucleus, cGAS was shown to interact with IFI16 bound to herpesvirus DNA and protect IFI16 from proteasomal degradation [57]. We did not observe any detectable difference in the levels of p204 protein in infected wt MEFs and cGAS KO MEFs (Fig. 10). We also were not able to detect complexes of cGAS and IFI16 proteins in infected or noninfected cells by coimmunoprecipitation assays (data not shown). We assumed that structural differences between human IFI16 and its mouse ortholog, p204, distinct properties of host cells, and differences in the arrangement of nucleosomes on DNA accounted for the different findings obtained in this study.

It is well established that cGAS senses in the cytoplasm self-originated DNA present in micronuclei and activates IFN response [82]. The formation of micronuclei is the result of chromosome mis-segregation caused by replication stress or chromosomal instability. It requires the completion of mitotic cell division. Nevertheless, the cells in interphase (as during MPyV infection) can also display signs of stress, such as chromatin herniation, lamina alterations, and DNA DSBs allocated in the nuclear envelop opening sites,

which result in the formation of nuclear blebs (micronucleus-like bodies). Once a micronucleus is formed, the nuclear envelope reseals rapidly, assisted by the ESCRT III membrane-remodeling machinery [83,84]. Micronucleus membranes are fragile and defects in their biochemical composition have been characterized [85]. Thus, micronucleus-like bodies, similar to micronuclei, may also have defects in membranes that make DNA accessible to cGAS sensing.

Cells infected with polyomaviruses have several characteristics supporting the formation of micronucleus-like bodies and leakage of DNA into the cytosol. Polyomaviruses induce host genome instability by the actions of their early regulatory proteins. They activate the host DDR to prolong the S-phase, but also have the ability to inhibit DDR downstream effectors, for example, by suppressing p53 to avoid untimely p53-induced apoptosis or senescence [86,87]. S-phase arrest induced by DDR enables exploitation of cellular DNA replication machinery for viral genome replication. Massive replication of viral genomes is accompanied by a large rearrangement and enlargement of the cell nucleus and nuclear envelope remodeling; membrane disruption may be caused by the viroporin properties of minor structural proteins of MPyV, VP2, and VP3. Specifically, viroporins may be responsible for the disruption of nuclear and ER membranes [20,88].

The induction of IFN type I by human JCPyV in human astrocytes or by BKPyV in microvascular endothelial (cells that are a potential BKPyV reservoir) has been described [89,90]. Our study represents the first effort to understand the molecular mechanisms that govern IFN induction in polyomavirus infections. Here, we presented two mechanisms of sensing of MPyV DNA, one through the interaction of p204 with viral genomes in the nucleus and the second in the cytosol by cGAS binding of DNA fragments leaked directly from the nucleus or sensing DNA accessible after membrane disruption of micronucleus-like bodies. The sensors p204 and cGAS appear to be activated independently by the virus during infection. Surprisingly, the production of IFN is moderate in MPyV-infected cells, suggesting a tight regulation of the IFN response by cells and by the intervention of viral antigens. The moderate IFN induction may contribute to polyomavirus persistency in the host.

Materials and methods

Cell lines and viruses

Mouse 3T6 fibroblasts (ATCC, Manassas, VA, USA; CCL-96), mouse embryo fibroblasts (MEFs) M-Fb-481 (Lonza, Basel, Switzerland), immortalized MEF-STING wt, MEF-STING KO, MEF-cGAS wt, and MEF-cGAS KO (kindly provided by J. Cambier, University of Colorado, USA, and J. Rehwinkel, University of Oxford, UK) were grown at 37 °C in a humidified incubator with an atmosphere of 5% CO_2, using Dulbecco's modified Eagle's medium (DMEM) from Sigma-Aldrich (St. Louis, MO, USA) supplemented with 10% fetal bovine serum (Invitrogen, Waltham, MA, USA) and 4 mM L-glutamine (Invitrogen). The MPyV strain BG (GenBank: AF442959.1) was isolated and purified from infected 3T6 cells using the standard protocol for purification by CsCl [91]. Mutant viruses lacking the NLS in capsid proteins (MPyVΔNLS: VP1K6Q-S7R-G8R-VP2/VP3 K314A-K315A-R317A) were prepared as described in [23]. In detail, a pMJG plasmid containing the entire genome of MPyV BG strain was used for mutagenesis. Next, the mutated or wt genomes were used for the transfection of 3T6 cells. After transfection, viruses were purified as described above [91] and purity of preparations was followed by electron microscopy using negative staining as described before [23].

Generation of 3T6 cell line expressing GFP-cGAS

For the production of N-terminally eGFP-tagged mouse cGAS, the plasmid pMSCVpuro-eGFP-mcGAS, coding for GFP-cGAS (gift from Andrew Jackson & Martin Reijns—plasmid # 108675 from Addgene, Watertown, MA, USA) [82], was transfected using Lipofectamine into Phoenix Ecotropic cells for the production of the retrovirus. Then, the retrovirus was used for transduction of 3T6 cells in the presence of polybrene. Mouse cells were further selected for stable integration using 1–10 $\mu g \cdot mL^{-1}$ puromycin.

Viral genome quantification

The quantification of MPyV genomes was performed by real-time PCR assay using iQ™ SYBR® Green Supermix (Bio-Rad Laboratories, Hercules, CA, USA), as described in [23]. The primer sets used were: VP1, 5′-GCAAGAAGGCGACGAC-3′ and 5′-TGGCCTCCCTCATAAGT-3′; and LT 5′-GCTGACAAAGAAAGGCTGCT-3′ and 5′-AGCCGGTTCCTCCTAGATTC-3′.

Reverse transcription quantitative PCR

Total cellular RNA was extracted using High Pure RNA Isolation Kit (Roche, Penzberg, Upper Bavaria, Germany) in accordance with the manufacturer's protocol. The RNA concentration and purity were measured by a nanodrop spectrophotometer (Thermo Fisher Scientific, Waltham, MA, USA). Reverse transcription was performed using the iScriptcDNA synthesis kit (Bio-Rad Laboratories) in accordance with the manufacturer's instructions. cDNAs were amplified by PCR using the following primer sets:

MX-1, 5′-GGTCGGCTTCTGGTTTTGTA-3′ and 5′-GAACAGGTCCACTTCCTCCA-3′;

GAPDH, 5′-ATGACATCAAGAAGGTGGTG-3′ and 5′-ATACCAGGAAATGAGCTTG-3′;

IFN-β, 5′-CCCTATGGAGATGACGGAGA-3′ and 5′-CTGTCTGCTGGTGGAGTTCA-3′;

spliced *LT*, 5′-GAACCGGCTTCCAGGGCTC-3′ and 5′-CTTAGGCGGCGACTGGTAG-3′.

The quantification of PCR products in real-time was performed in a LightCycler 480 II (Roche) using the LightCycler® 480 SYBR Green I Master kit (Roche) in accordance with the manufacturer's protocol. The quantification of target gene expression was performed using LightCycler 480 II software based on the relative quantification method, which determined the concentration of target amplicons normalized to the reference gene GAPDH.

SDS/PAGE and western blotting analysis

The cells were harvested and then resuspended in modified RIPA buffer (10 mM Tris/HCl, pH 7.4, 1 mM EDTA, 150 mM NaCl, 1% Nonidet P-40, 1% sodium deoxycholate, 0.1% SDS) supplemented with protease inhibitor cocktail (Complete Mini EDTA free from Roche). Then, the cells were lysed in RIPA for 20 min on ice and cell debris was removed by centrifugation. The proteins were resuspended in Laemmli buffer and separated by 10% SDS/PAGE. The gels were blotted to nitrocellulose membranes and immunoassayed using the indicated antibodies. The proteins were visualized by chemiluminescence using the application of AI-600 (GE Healthcare, Chicago, IL, USA).

Nuclear-cytoplasmic fractionation

We used either the nuclear and cytosol extraction kit to prepare cell fractions in accordance with the manufacturer's instructions (G-Biosciences, Saint Louis, MO, USA) or performed extraction using NP40 in accordance with the protocol described by Nabbi *et al.* [92]. In addition, when required, nuclear fractions were further separated into soluble and insoluble fractions. Nuclear fraction was resuspended in Solution B (3 mM EDTA, 0.2 mM EGTA, and 1 mM DTT) and incubated on ice for 30 min. The soluble fraction was separated by centrifugation at 1700 ***g*** for 4 min at 4 °C. The pellet containing chromatin was washed with Buffer B, and the chromatin pellet was lysed in RIPA buffer.

Antibodies

Rat monoclonal anti-large T antigen (LT; provided by B. E. Griffin, Imperial College of Science, Technology and Medicine at St. Mary's, London, UK), rabbit polyclonal antibody against GAPDH (Sigma-Aldrich), rabbit polyclonal anti-phospho-IRF3 (Ser369(4D4G); Cell Signaling Technology, Danvers, MA, USA), rabbit polyclonal anti-phospho-IRF3 (Ser369 (D601M); Cell Signaling Technology), rabbit polyclonal anti-phospho-STING-Ser365-D8F4W (Cell Signaling Technology), rabbit polyclonal anti-phospho-STING (Ser365(D1C4T); Cell Signaling Technology), rabbit polyclonal against IFI16/p204 (Elabscience, Houston, TX, USA), rabbit polyclonal anti STING/anti MPYS (Sigma), rabbit monoclonal anti cGAS (Cell Signaling Technology), polyclonal rabbit anti-biotin antibody (A150; Bethyl Laboratories, Montgomery, TX USA), rabbit IgG-HRP (Bio-Rad), goat anti-rat IgG-HRP (Bio-Rad), Cy3® goat anti-rabbit IgG (Thermo Fisher Scientific), Alexa Fluor® 488 goat anti-rabbit IgG (Thermo Fisher Scientific), Alexa Fluor® 488 goat anti-rat IgG (Thermo Fisher Scientific), Alexa Fluor® 488 goat anti-rabbit (Cell Signaling Technology), and Alexa Fluor® 647 goat anti-rat IgG (Thermo Fisher Scientific).

Immunofluorescence staining

The cells were grown on coverslips. At the indicated time points, the cells were fixed in 4% paraformaldehyde (PFA) for 15 min or ice-cold methanol for 10 min at −20 °C and permeabilized with 0.5% Triton X-100 in PBS for 5 min (after fixation with PFA). After washing in PBS, the cells were incubated with blocking solution (0.25% BSA and 0.25% porcine skin gelatin in PBS) for 30 min. Immunostaining was conducted with primary and secondary antibodies for 1 h and 30 min, respectively, with extensive washing in 1× PBS after each incubation.

The coverslips were stained with DAPI, mounted on droplets of Anti-Fade Fluorescence Mounted Medium (Abcam, Cambridge, UK), and images were obtained using a LSM 880NLO confocal microscope (Carl Zeiss, Oberkochen, Germany).

Immunofluorescence staining with pre-extraction buffer

Cells were grown on coverslips. At the indicated time points, the medium was removed, and the cells were incubated for 5 min on ice with pre-extraction buffer containing 25 mM HEPES, 50 mM NaCl, 3 mM $MgCl_2$, 300 mM sucrose, and 0.5% Triton X-100 (pH 7.4). The cells were then washed once with 1× PBS and fixed with ice-cold methanol for 10 min at −20 °C. After washing in PBS, cells were incubated for 30 min in blocking buffer, as above, and the staining was performed as for regular immunofluorescence staining (as described above).

Fluorescence *in situ* hybridization combined with immunofluorescence or Edu labeling

We performed FISH in combination with immunofluorescence in accordance with the protocol described by Solovei and Cremer [93]. In brief, cells were grown on coverslips,

fixed with 2% PFA for 10 min, permeabilized with 0.5% Triton X-100 for 10 min, incubated in blocking solution (1% BSA/PBS) for 1 h, and stained by the selected antibodies or subjected to Edu Click chemistry. The cells were postfixed with 4% PFA for 5 min, treated with RNAse, and incubated with 20% glycerol/PBS for 1 h. Then, five freeze-thaw cycles were performed in liquid nitrogen. The cells were then equilibrated in 50% formamide/2× SSC for 8 h and hybridized with the MPyV DNA probe generated by nick translation using BioNick DNA Labeling System (Invitrogen). Denaturation and hybridization were performed as follows: 90 °C-2 min, 80 °C-2 min, 70 °C-2 min, 60 °C-2 min, 50 °C-2 min, 42 °C-1 h, and 37 °C overnight. After hybridization, the cells were washed three times in 2× SSC at 37 °C and twice in 0.1× SSC at 60 °C. Each wash step was performed for 10 min. After washing, the cells were incubated with blocking solution (1% BSA/PBS) for 1 h and processed for the detection of biotin by using antibodies. Coverslips were stained with DAPI and mounted on droplets of Anti-Fade Fluorescence Mounted Medium (Abcam). Images were obtained using a LSM 880NLO confocal microscope (Carl Zeiss).

Viral infection

Cells were seeded on 13-mm glass coverslips or plates and grown to a confluency of approximately 50%. On the day of infection, the cells were washed with serum-free DMEM and incubated with MPyV diluted in serum-free medium for 1 h at 37 °C. The start of infection was measured from the time the virus was added to cells. After virus adsorption, the cells were washed to remove the unbound virus and incubated in DMEM supplemented with 10% FBS for the indicated times.

Cell stimulation with inducers of IFN

Polyinosinic:polycytidylic acid (GE Healthcare) was used to stimulate 3T6 cells; specifically, 2×10^6 cells were transfected by TurboFect (Thermo Fisher Scientific) with 20 μg of poly (I:C). The cells were incubated for 16 h and then collected for isolation of RNA or for the preparation of cell lysates. c-di-GAMP (InvivoGen, San Diego, CA, USA), pDNA, CpG oligonucleotide (InvivoGen) or 26-mer DNA (G3-YSD, InvivoGen) were used to stimulate 3T6 cells as follows: cells (4×10^6) were transfected with 4 μg of c-di-GAMP, 6 μg of pDNA, or 4 μg CpG by Amaxa nucleofector (Lonza), incubated for a further 6 h, and collected for the isolation of RNA.

EdU click chemistry

The Click-iT EdU reaction was performed in accordance with the instructions for the Click-iT imaging kit (Invitrogen). In brief, a solution of 20 μM EdU was prepared in complete medium and added to growing cells on coverslips to a final concentration of 10 μM. After incubation for 30 min, the cells were fixed, permeabilized, blocked in 3% BSA/PBS, and subjected to Click-iT reaction.

siRNA transfection

Sense and antisense siRNA for p204 were prepared in Lipofectamine in accordance with manufacturer's instructions (Thermo Fisher Scientific). The siRNA sequences were: 5′-GUUUCAUCAAGAUAUCAAAtt-3′ and 5′-UUUGAUAUCUUGAUGAAAtg-3′. As a control, the Silencer® Select Negative Control #1 siRNA (Thermo Fisher Scientific) was used.

2′3′-cGAMP detection by LC-MS

For detection of 2′3′-cGAMP, the cells were detached using trypsin and 4×10^6 cells were collected and used for the experiment. The cells were washed five times with 1 mL of 1× PBS and lysed in lysis buffer (20% acetonitrile and 40% methanol in deionized water). Then, the lysates were heated for 10 min at 60 °C and cooled for 10 min on ice. After cooling, the samples were centrifuged at 17 000 ***g*** for 10 min at 4 °C, and the supernatant was collected in a clean Eppendorf tube (Supernatant A). The pellet produced in the previous centrifuge step was washed in 500 μL of H_2O and centrifuged at 17 000 ***g*** for 10 min at 4 °C, and the supernatant was collected in a clean Eppendorf tube (Supernatant B). Supernatants A and B were combined and centrifuged at 17 000 ***g*** for 5 min at 4 °C and transferred to a new Eppendorf tube. To prepare the samples for analysis by LC-MS, the samples were frozen at −80 °C for 1 day, dried by vacuum centrifugation, and resuspended in 40 μL of H_2O.

As control, an internal standard of 100 pmol of 2′3′-cGAMP was spiked into the lysate of mock-infected cells or cells transfected with a pDNA and collected after 2 h.

2′3′-cGAMP expression was measured using a Dionex Ultimate 3000RS LC system coupled to a TSQ Quantiva mass spectrometer (Thermo Fisher Scientific) using an ESI source in positive mode with the following ion source parameters: ion transfer tube temperature, 300 °C; vaporizer temperature, 125 °C; spray voltage, 3500 V; sheath gas, 35 arbitrary units (au); auxiliary gas, 5 au. A ZIC®-HILIC column (150 mm × 2.1 mm, 5 μm) from Merck (Darmstadt, Germany) was used to separate the analytes. The column was maintained at room temperature and an injection volume of 2 μL was used per sample. A gradient elution was set from 15% B to 60% B (A: 95% acetonitrile and 5% 10 mM ammonium acetate pH 9.3, B: 10 mM ammonium carbonate in water, pH 9.3) in 7.3 min at a flow rate of 200 $\mu L \cdot min^{-1}$, followed by a washing phase (2.7 min of 60% B) and an equilibration phase (9 min of 15% B). For the targeted determination of 2′3′-cGAMP,

a selective reaction monitoring assay was used, which was developed previously, comprising infusion of the pure compound and monitoring the following seven transitions: 675.1 > 136.1, 675.1 > 524.1, 675.1 > 312.1, 675.1 > 506.0, 675.1 > 152.1, 675.1 > 476.0, and 675.1 > 330.0. The integration of 2′3′-cGAMP peak areas was related to the transition 675.1 > 506, which provided appropriate signal intensity and was less affected by the matrix effect.

2′3′-cGAMP ELISA detection

2′3′-cGAMP ELISA was performed in accordance with the manufacturer's protocol using 2′3′-cGAMP ELISA Kit (Arbor Assays, Ann Arbor, MI, USA). In brief, mock-infected or infected cells, (1.5×10^6) were used for fractionation with the kit described above. The fractions were handled on ice and immediately used for ELISA. The 2′3′-cGAMP standards were prepared in the cytosolic and nuclear cell lysis buffers to achieve precise calculation of the 2′3′-cGAMP concentration in the samples. The cell fractions or standards were added to the ELISA plates, followed by antibodies against 2′3′-cGAMP and HRP-labeled–2′3′-cGAMP for a competition assay. After incubation for 2 h, the plates were washed; subsequently, the reaction was developed using TMB and stopped by HCl. The optical density (OD) was measured at 450 nm using a microplate ELISA reader (Tecan, Männedorf, Switzerland). The data were processed using the Four Parameter logistic (4PL) curve calculator available online (myassays.com) as recommended by the manufacturer.

Statistical analysis

Student's *t*-test was performed using the GRAPHPAD PRISM software, version 6.0 (GraphPad Software, La Jolla, CA, USA). Asterisks indicate *P*-values representing statistically significant differences ($*P \leq 0.05$, $**P \leq 0.01$, $***P \leq 0.001$, $****P \leq 0.0001$).

Acknowledgements

We are grateful to the Imaging Methods Core Facility at BIOCEV [supported by the MEYS CR (Large RI Project LM2018129 Czech-Bioimaging) and ERDF (project No. CZ.02.1.01/0.0/0.0/18_046/0016045)] for their support with obtaining the imaging data presented in this paper, as well to the Proteomic and Metabolomic Core Facility, BIOCEV, Faculty of Science, Charles University in Prague (supported by OP VaVpI CZ.1.05/1.1.00/02.0109) for the mass spectrometric measurements. This study was supported by the Grant Agency of the Czech Republic (19-14445S) and by the specific university research project grant-SVV by the Charles University (SVV 260568).

Author contributions

SH, BR, IS, VS, and JF contributed to conception and design of the experiments. BR, IS, SH, and VS performed the experiments. BR, SH, JF, IS, and VS analyzed the data. SH, JF, BR, and IS wrote the manuscript.

Conflict of interest

The authors declare no conflict of interest.

Peer Review

The peer review history for this article is available at https://publons.com/publon/10.1111/febs.15962.

References

1 Cook L (2016) Polyomaviruses. *Microbiol Spectr* **4**, 3–9.
2 Gheit T, Dutta S, Oliver J, Robitaille A, Hampras S, Combes J-D, McKay-Chopin S, Le Calvez-Kelm F, Fenske N, Cherpelis B *et al.* (2017) Isolation and characterization of a novel putative human polyomavirus. *Virology* **506**, 45–54.
3 Feng H, Shuda M, Chang Y & Moore PS (2008) Clonal integration of a polyomavirus in human merkel cell carcinoma. *Science* **319**, 1096–1100.
4 Gardner SD, Field AM, Coleman DV & Hulme B (1971) New human papovavirus (B.K.) isolated from urine after renal transplantation. *Lancet* **1**, 1253–1257.
5 van der Meijden E, Janssens RWA, Lauber C, Bouwes Bavinck JN, Gorbalenya AE & Feltkamp MCW (2010) Discovery of a new human polyomavirus associated with trichodysplasia spinulosa in an immunocompromized patient. *PLoS Pathog* **6**, e1001024.
6 Padgett BL, Walker DL, ZuRhein GM, Eckroade RJ & Dessel BH (1971) Cultivation of papova-like virus from human brain with progressive multifocal leucoencephalopathy. *Lancet* **1**, 1257–1260.
7 Viscidi RP, Rollison DE, Sondak VK, Silver B, Messina JL, Giuliano AR, Fulp W, Ajidahun A & Rivanera D (2011) Age-specific seroprevalence of merkel cell polyomavirus, BK Virus, and JC virus. *Clin Vaccine Immunol* **18**, 1737–1743.
8 Hampras SS, Giuliano AR, Lin H-Y, Fisher KJ, Abrahamsen ME, McKay-Chopin S, Gheit T, Tommasino M & Rollison DE (2015) Natural history of polyomaviruses in men: the HPV infection in men (HIM) Study. *J Infect Dis* **211**, 1437–1446.
9 Nicol JTJ, Robinot R, Carpentier A, Carandina G, Mazzoni E, Tognon M, Touzé A & Coursaget P (2013) Age-specific seroprevalences of merkel cell polyomavirus, human polyomaviruses 6, 7, and 9, and

trichodysplasia spinulosa-associated polyomavirus. *Clin Vaccine Immunol* **20**, 363–368.
10 Qin Q, EL Shwetank F, Maru S & Lukacher AE (2016) Type I interferons regulate the magnitude and functionality of mouse polyomavirus-specific CD8 T cells in a virus strain-dependent manner. *J Virol* **90**, 5187–5199.
11 Chen XS (1998) Interaction of polyomavirus internal protein VP2 with the major capsid protein VP1 and implications for participation of VP2 in viral entry. *EMBO J* **17**, 3233–3240.
12 Stehle T & Harrison SC (1996) Crystal structures of murine polyomavirus in complex with straight-chain and branched-chain sialyloligosaccharide receptor fragments. *Structure* **4**, 183–194.
13 Carmichael G (2016) Gene regulation and quality control in murine polyomavirus infection. *Viruses* **8**, 284.
14 Jakobovits EB, Bratosin S & Aloni Y (1980) A nucleosome-free region in SV40 minichromosomes. *Nature* **285**, 263–265.
15 Saragosti S, Moyne G & Yaniv M (1980) Absence of nucleosomes in a fraction of SV40 chromatin between the origin of replication and the region coding for the late leader RNA. *Cell* **20**, 65–73.
16 Varshavsky AJ, Sundin O & Bohn M (1979) A stretch of "late" SV40 viral DNA about 400 bp long which includes the origin of replication is specifically exposed in SV40 minichromosomes. *Cell* **16**, 453–466.
17 Liebl D, Difato F, Hornikova L, Mannova P, Stokrova J & Forstova J (2006) Mouse polyomavirus enters early endosomes, requires their acidic pH for productive infection, and meets transferrin cargo in Rab11-positive endosomes. *J Virol* **80**, 4610–4622.
18 Qian M, Cai D, Verhey KJ & Tsai B (2009) A lipid receptor sorts polyomavirus from the endolysosome to the endoplasmic reticulum to cause infection. *PLoS Pathog* **5**, e1000465.
19 Zila V, Difato F, Klimova L, Huerfano S & Forstova J (2014) Involvement of microtubular network and its motors in productive endocytic trafficking of mouse polyomavirus. *PLoS One* **9**, e96922.
20 Huérfano S, Ryabchenko B, Španielová H & Forstová J (2017) Hydrophobic domains of mouse polyomavirus minor capsid proteins promote membrane association and virus exit from the ER. *FEBS J* **284**, 883–902.
21 Inoue T & Tsai B (2011) A large and intact viral particle penetrates the endoplasmic reticulum membrane to reach the cytosol. *PLoS Pathog* **7**, e1002037.
22 Magnuson B, Rainey EK, Benjamin T, Baryshev M, Mkrtchian S & Tsai B (2005) ERp29 triggers a conformational change in polyomavirus to stimulate membrane binding. *Mol Cell* **20**, 289–300.
23 Soldatova I, Prilepskaja T, Abrahamyan L, Forstová J & Huérfano S (2018) Interaction of the mouse polyomavirus capsid proteins with importins is required for efficient import of viral DNA into the cell nucleus. *Viruses* **10**, 165.
24 Chen L & Fluck M (2001) Kinetic analysis of the steps of the polyomavirus lytic cycle. *J Virol* **75**, 8368–8379.
25 Ahmad-Nejad P, Häcker H, Rutz M, Bauer S, Vabulas RM & Wagner H (2002) Bacterial CpG-DNA and lipopolysaccharides activate Toll-like receptors at distinct cellular compartments. *Eur J Immunol* **32**, 1958.
26 Bauer S, Kirschning CJ, Hacker H, Redecke V, Hausmann S, Akira S, Wagner H & Lipford GB (2001) Human TLR9 confers responsiveness to bacterial DNA via species-specific CpG motif recognition. *Proc Natl Acad Sci USA* **98**, 9237–9242.
27 Hemmi H, Takeuchi O, Kawai T, Kaisho T, Sato S, Sanjo H, Matsumoto M, Hoshino K, Wagner H, Takeda K *et al.* (2000) A Toll-like receptor recognizes bacterial DNA. *Nature* **408**, 740–745.
28 Takaoka A, Wang Z, Choi MK, Yanai H, Negishi H, Ban T, Lu Y, Miyagishi M, Kodama T, Honda K *et al.* (2007) DAI (DLM-1/ZBP1) is a cytosolic DNA sensor and an activator of innate immune response. *Nature* **448**, 501–505.
29 Chiu Y-H, MacMillan JB & Chen ZJ (2009) RNA polymerase III detects cytosolic DNA and induces Type I interferons through the RIG-I pathway. *Cell* **138**, 576–591.
30 Hornung V, Ablasser A, Charrel-Dennis M, Bauernfeind F, Horvath G, DanielR C, Latz E & Fitzgerald KA (2009) AIM2 recognizes cytosolic dsDNA and forms a caspase-1-activating inflammasome with ASC. *Nature* **458**, 514–518.
31 Horan KA, Hansen K, Jakobsen MR, Holm CK, Soby S, Unterholzner L, Thompson M, West JA, Iversen MB, Rasmussen SB *et al.* (2013) Proteasomal degradation of herpes simplex virus capsids in macrophages releases DNA to the cytosol for recognition by DNA sensors. *J Immunol* **190**, 2311–2319.
32 Unterholzner L, Keating SE, Baran M, Horan KA, Jensen SB, Sharma S, Sirois CM, Jin T, Latz E, Xiao TS *et al.* (2010) IFI16 is an innate immune sensor for intracellular DNA. *Nat Immunol* **11**, 997–1004.
33 Zhu W, Liu P, Yu L, Chen Q, Liu Z, Yan K, Lee WM, Cheng CY & Han D (2014) p204-Initiated Innate Antiviral Response in Mouse Leydig Cells1. *Biol Reprod* **91**.
34 Yang P, An H, Liu X, Wen M, Zheng Y, Rui Y & Cao X (2010) The cytosolic nucleic acid sensor LRRFIP1 mediates the production of type I interferon via a β-catenin-dependent pathway. *Nat Immunol* **11**, 487–494.
35 Zhang X, Brann TW, Zhou M, Yang J, Oguariri RM, Lidie KB, Imamichi H, Huang D-W, Lempicki RA, Baseler MW *et al.* (2011) Cutting edge: Ku70 is a novel cytosolic DNA sensor that induces type III rather than type I IFN. *J Immunol* **186**, 4541–4545.

36 Kim T, Pazhoor S, Bao M, Zhang Z, Hanabuchi S, Facchinetti V, Bover L, Plumas J, Chaperot L, Qin J *et al.* (2010) Aspartate-glutamate-alanine-histidine box motif (DEAH)/RNA helicase A helicases sense microbial DNA in human plasmacytoid dendritic cells. *Proc Natl Acad Sci USA* **107**, 15181–15186.
37 Zhang Z, Yuan B, Bao M, Lu N, Kim T & Liu Y-J (2011) The helicase DDX41 senses intracellular DNA mediated by the adaptor STING in dendritic cells. *Nat Immunol* **12**, 959–965.
38 Sun L, Wu J, Du F, Chen X & Chen ZJ (2013) Cyclic GMP-AMP synthase is a cytosolic DNA sensor that activates the type I interferon pathway. *Science* **339**, 786–791.
39 Wu J, Sun L, Chen X, Du F, Shi H, Chen C & Chen ZJ (2013) Cyclic GMP-AMP is an endogenous second messenger in innate immune signaling by cytosolic DNA. *Science* **339**, 826–830.
40 Diner BA, Li T, Greco TM, Crow MS, Fuesler JA, Wang J & Cristea IM (2015) The functional interactome of PYHIN immune regulators reveals IFIX is a sensor of viral DNA. *Mol Syst Biol* **11**, 787.
41 Li T, Diner BA, Chen J & Cristea IM (2012) Acetylation modulates cellular distribution and DNA sensing ability of interferon-inducible protein IFI16. *Proc Natl Acad Sci USA* **109**, 10558–10563.
42 Orzalli MH, DeLuca NA & Knipe DM (2012) Nuclear IFI16 induction of IRF-3 signaling during herpesviral infection and degradation of IFI16 by the viral ICP0 protein. *Proc Natl Acad Sci USA* **109**, E3008–E3017.
43 Storek KM, Gertsvolf NA, Ohlson MB & Monack DM (2015) cGAS and Ifi204 cooperate to produce type I IFNs in response to *Francisella* Infection. *J Immunol* **194**, 3236–3245.
44 Gentili M, Lahaye X, Nadalin F, Nader GPF, Puig Lombardi E, Herve S, De Silva NS, Rookhuizen DC, Zueva E, Goudot C *et al.* (2019) The N-terminal domain of cGAS determines preferential association with centromeric DNA and innate immune activation in the nucleus. *Cell Rep* **26**, 2377–2393.e13.
45 Stratmann SA, Morrone SR, van Oijen AM & Sohn J 2015) The innate immune sensor IFI16 recognizes foreign DNA in the nucleus by scanning along the duplex. *eLife* **4**, e11721.
46 Liu H, Zhang H, Wu X, Ma D, Wu J, Wang L, Jiang Y, Fei Y, Zhu C, Tan R *et al.* (2018) Nuclear cGAS suppresses DNA repair and promotes tumorigenesis. *Nature* **563**, 131–136.
47 Seo GJ, Kim C, Shin W-J, Sklan EH, Eoh H & Jung JU (2018) TRIM56-mediated monoubiquitination of cGAS for cytosolic DNA sensing. *Nat Commun* **9**, 613.
48 Song B, Greco TM, Lum KK, Taber CE & Cristea IM (2020) The DNA sensor cGAS is decorated by acetylation and phosphorylation modifications in the context of immune signaling. *Mol Cell Proteomics* **19**, 1193–1208.
49 Volkman HE, Cambier S, Gray EE & Stetson DB (2019) Tight nuclear tethering of cGAS is essential for preventing autoreactivity. *eLife* **8**, e47491.
50 Morrone SR, Wang T, Constantoulakis LM, Hooy RM, Delannoy MJ & Sohn J (2014) Cooperative assembly of IFI16 filaments on dsDNA provides insights into host defense strategy. *Proc Natl Acad Sci USA* **111**, E62–E71.
51 Seo GJ, Yang A, Tan B, Kim S, Liang Q, Choi Y, Yuan W, Feng P, Park H-S & Jung JU (2015) Akt kinase-mediated checkpoint of cGAS DNA sensing pathway. *Cell Rep* **13**, 440–449.
52 Ni X, Ru H, Ma F, Zhao L, Shaw N, Feng Y, Ding W, Gong W, Wang Q, Ouyang S *et al.* (2016) New insights into the structural basis of DNA recognition by HINa and HINb domains of IFI16. *J Mol Cell Biol* **8**, 51–61.
53 Kujirai T, Zierhut C, Takizawa Y, Kim R, Negishi L, Uruma N, Hirai S, Funabiki H & Kurumizaka H (2020) Structural basis for the inhibition of cGAS by nucleosomes. *Science* **370**, 455–458.
54 Xia P, Ye B, Wang S, Zhu X, Du Y, Xiong Z, Tian Y & Fan Z (2016) Glutamylation of the DNA sensor cGAS regulates its binding and synthase activity in antiviral immunity. *Nat Immunol* **17**, 369–378.
55 Dai J, Huang Y-J, He X, Zhao M, Wang X, Liu Z-S, Xue W, Cai H, Zhan X-Y, Huang S-Y *et al.* (2019) Acetylation blocks cGAS activity and inhibits self-DNA-induced autoimmunity. *Cell* **176**, 1447–1460.e14.
56 Ansari MA, Dutta S, Veettil MV, Dutta D, Iqbal J, Kumar B, Roy A, Chikoti L, Singh VV & Chandran B (2015) Herpesvirus genome recognition induced acetylation of nuclear IFI16 is essential for its cytoplasmic translocation, inflammasome and IFN-β responses. *PLOS Pathog* **11**, e1005019.
57 Orzalli MH, Broekema NM, Diner BA, Hancks DC, Elde NC, Cristea IM & Knipe DM (2015) cGAS-mediated stabilization of IFI16 promotes innate signaling during herpes simplex virus infection. *Proc Natl Acad Sci USA* **112**, E1773–E1781.
58 Fan X, Jiang J, Zhao D, Chen F, Ma H, Smith P, Unterholzner L, Xiao TS & Jin T (2021) Structural mechanism of DNA recognition by the p204 HIN domain. *Nucleic Acids Res* **49**, 2959–2972.
59 Lum KK, Howard TR, Pan C & Cristea IM (2019) Charge-mediated pyrin oligomerization nucleates antiviral IFI16 sensing of herpesvirus DNA. *MBio* **10**, e01428-19.
60 Almine JF, O'Hare CAJ, Dunphy G, Haga IR, Naik RJ, Atrih A, Connolly DJ, Taylor J, Kelsall IR, Bowie AG *et al.* (2017) IFI16 and cGAS cooperate in the activation of STING during DNA sensing in human keratinocytes. *Nat Commun* **8**, 14392.

61 Liu S, Cai X, Wu J, Cong Q, Chen X, Li T, Du F, Ren J, Wu Y-T, Grishin NV *et al.* (2015) Phosphorylation of innate immune adaptor proteins MAVS, STING, and TRIF induces IRF3 activation. *Science* **347**, aaa2630.

62 Gao P, Ascano M, Wu Y, Barchet W, Gaffney BL, Zillinger T, Serganov AA, Liu Y, Jones RA, Hartmann G *et al.* (2013) Cyclic [G(2′,5′)pA(3′,5′)p] is the metazoan second messenger produced by DNA-activated cyclic GMP-AMP synthase. *Cell* **153**, 1094–1107.

63 Huerfano S, Ryabchenko B & Forstová J (2013) Nucleofection of expression vectors induces a robust interferon response and inhibition of cell proliferation. *DNA Cell Biol* **32**, 467–479.

64 Semenova N, Bosnjak M, Markelc B, Znidar K, Cemazar M & Heller L (2019) Multiple cytosolic DNA sensors bind plasmid DNA after transfection. *Nucleic Acids Res* **47**, 10235–10246.

65 Hua K & Ferland RJ (2017) Fixation methods can differentially affect ciliary protein immunolabeling. *Cilia* **6**, 5.

66 Ma Z, Ni G & Damania B (2018) Innate sensing of DNA virus genomes. *Annu Rev Virol* **5**, 341–362.

67 Carbone M, Ascione G, Chichiarelli S, Garcia M-I, Eufemi M & Amati P (2004) Chromosome-Protein interactions in polyomavirus virions . *J Virol* **78**, 513–519.

68 Jiang M, Abend JR, Tsai B & Imperiale MJ (2009) Early events during BK virus entry and disassembly. *J Virol* **83**, 1350–1358.

69 Sun C, Luecke S, Bodda C, Jønsson KL, Cai Y, Zhang B-C, Jensen SB, Nordentoft I, Jensen JM, Jakobsen MR *et al.* (2019) Cellular requirements for sensing and elimination of incoming HSV-1 DNA and capsids. *J Interferon Cytokine Res* **39**, 191–204.

70 Kumar S, Morrison JH, Dingli D & Poeschla E (2018) HIV-1 activation of innate immunity depends strongly on the intracellular level of TREX1 and sensing of incomplete reverse transcription products. *J Virol* **92**, e00001–18.

71 Herrera FJ & Triezenberg SJ (2004) VP16-dependent association of chromatin-modifying coactivators and underrepresentation of histones at immediate-early gene promoters during herpes simplex virus infection. *J Virol* **78**, 9689–9696.

72 Oh J & Fraser NW (2008) Temporal association of the herpes simplex virus genome with histone proteins during a lytic infection. *J Virol* **82**, 3530–3537.

73 Dutta D, Dutta S, Veettil MV, Roy A, Ansari MA, Iqbal J, Chikoti L, Kumar B, Johnson KE & Chandran B (2015) BRCA1 regulates IFI16 mediated nuclear innate sensing of herpes viral DNA and subsequent induction of the innate inflammasome and interferon-β responses. *PLoS Pathog* **11**, e1005030.

74 Iqbal J, Ansari MA, Kumar B, Dutta D, Roy A, Chikoti L, Pisano G, Dutta S, Vahedi S, Veettil MV *et al.* (2016) Histone H2B-IFI16 recognition of nuclear herpesviral genome induces cytoplasmic interferon-β responses. *PLoS Pathog* **12**, e1005967.

75 Diner BA, Lum KK, Toettcher JE & Cristea IM (2016) Viral DNA sensors IFI16 and cyclic GMP-AMP synthase possess distinct functions in regulating viral gene expression, immune defenses, and apoptotic responses during herpesvirus, infection. *MBio* **7**, e01553-16.

76 Dunphy G, Flannery SM, Almine JF, Connolly DJ, Paulus C, Jønsson KL, Jakobsen MR, Nevels MM, Bowie AG & Unterholzner L (2018) Non-canonical activation of the DNA sensing adaptor STING by ATM and IFI16 mediates NF-κB signaling after nuclear DNA damage. *Mol Cell* **71**, 745–760.e5.

77 Ablasser A, Goldeck M, Cavlar T, Deimling T, Witte G, Röhl I, Hopfner K-P, Ludwig J & Hornung V (2013) cGAS produces a 2′-5′-linked cyclic dinucleotide second messenger that activates STING. *Nature* **498**, 380–384.

78 Glück S, Guey B, Gulen MF, Wolter K, Kang T-W, Schmacke NA, Bridgeman A, Rehwinkel J, Zender L & Ablasser A (2017) Innate immune sensing of cytosolic chromatin fragments through cGAS promotes senescence. *Nat Cell Biol* **19**, 1061–1070.

79 Chen Q, Sun L & Chen ZJ (2016) Regulation and function of the cGAS–STING pathway of cytosolic DNA sensing. *Nat Immunol* **17**, 1142–1149.

80 Zierhut C, Yamaguchi N, Paredes M, Luo J-D, Carroll T & Funabiki H (2019) The Cytoplasmic DNA sensor cGAS promotes mitotic cell death. *Cell* **178**, 302–315.e23.

81 Jiang H, Xue X, Panda S, Kawale A, Hooy RM, Liang F, Sohn J, Sung P & Gekara NO (2019) Chromatin-bound cGAS is an inhibitor of DNA repair and hence accelerates genome destabilization and cell death. *EMBO J* **38**, e102718.

82 Mackenzie KJ, Carroll P, Martin C-A, Murina O, Fluteau A, Simpson DJ, Olova N, Sutcliffe H, Rainger JK, Leitch A *et al.* (2017) cGAS surveillance of micronuclei links genome instability to innate immunity. *Nature* **548**, 461–465.

83 Cheong HSJ, Seth I, Joiner MC & Tucker JD (2013) Relationships among micronuclei, nucleoplasmic bridges and nuclear buds within individual cells in the cytokinesis-block micronucleus assay. *Mutagenesis* **28**, 433–440.

84 Raab M, Gentili M, de Belly H, Thiam H-R, Vargas P, Jimenez AJ, Lautenschlaeger F, Voituriez R, Lennon-Dumenil A-M, Manel N *et al.* (2016) ESCRT III repairs nuclear envelope ruptures during cell migration to limit DNA damage and cell death. *Science* **352**, 359–362.

85 Liu S, Kwon M, Mannino M, Yang N, Renda F, Khodjakov A & Pellman D (2018) Nuclear envelope assembly defects link mitotic errors to chromothripsis. *Nature* **561**, 551–555.
86 Dey D, Dahl J, Cho S & Benjamin TL (2002) Induction and bypass of p53 during productive infection by polyomavirus. *J Virol* **76**, 9526–9532.
87 Justice JL, Needham JM & Thompson SR (2019) BK Polyomavirus Activates the DNA Damage Response To Prolong S Phase. *J Virol* **93**, e00130–19, /jvi/93/14/JVI.00130-19.atom.
88 Huerfano S, Žíla V, Bouřa E, Španielová H, Štokrová J & Forstová J (2010) Minor capsid proteins of mouse polyomavirus are inducers of apoptosis when produced individually but are only moderate contributors to cell death during the late phase of viral infection. *FEBS J* **277**, 1270–1283.
89 Verma S, Ziegler K, Ananthula P, Co JKG, Frisque RJ, Yanagihara R & Nerurkar VR (2006) JC virus induces altered patterns of cellular gene expression: Interferon-inducible genes as major transcriptional targets. *Virology* **345**, 457–467.
90 An P, Sáenz Robles MT, Duray AM, Cantalupo PG & Pipas JM (2019) Human polyomavirus BKV infection of endothelial cells results in interferon pathway induction and persistence. *PLoS Pathog* **15**, e1007505.
91 Horníková L, Žíla V, Španielová H & Forstová J (2015) Mouse polyomavirus: propagation, purification, quantification, and storage. *Curr Protoc Microbiol* **38**, 14F.1.1–14F.1.26.
92 Nabbi A & Riabowol K (2015) Rapid isolation of nuclei from cells *in vitro*. *Cold Spring Harb Protoc* **2015**, pdb.prot083733.
93 Solovei I & Cremer M (2010) 3D-FISH on cultured cells combined with immunostaining. In Fluorescence *in situ* Hybridization (FISH) (Bridger JM & Volpi EV, eds), pp. 117–126.Humana Press, Totowa, NJ.

cancers

MDPI

Article

TLR4-Mediated Recognition of Mouse Polyomavirus Promotes Cancer-Associated Fibroblast-Like Phenotype and Cell Invasiveness

Vaclav Janovec [1,2], Boris Ryabchenko [1], Aneta Škarková [3], Karolína Pokorná [2], Daniel Rösel [3], Jan Brábek [3], Jan Weber [2], Jitka Forstová [1,†], Ivan Hirsch [1,2,4,*,†] and Sandra Huérfano [1,†]

1 Department of Genetics and Microbiology, Faculty of Science, Charles University, BIOCEV, 25150 Vestec, Czech Republic; vaclav.janovec@natur.cuni.cz (V.J.); boris.ryabchenko@natur.cuni.cz (B.R.); jitka.forstova@natur.cuni.cz (J.F.); huerfano@natur.cuni.cz (S.H.)
2 IOCB Gilead Research Center, Institute of Organic Chemistry and Biochemistry of the Czech Academy of Sciences, 16000 Prague, Czech Republic; karolina.pokorna@uochb.cas.cz (K.P.); jan.weber@uochb.cas.cz (J.W.)
3 Department of Cell Biology, Faculty of Science, Charles University, BIOCEV, 25150 Vestec, Czech Republic; aneta.skarkova@natur.cuni.cz (A.Š.); daniel.rosel@natur.cuni.cz (D.R.); jan.brabek@natur.cuni.cz (J.B.)
4 Institute of Molecular Genetics of the Czech Academy of Sciences, 14220 Prague, Czech Republic
* Correspondence: hirschi@natur.cuni.cz; Tel.: +420-221-951-723
† These authors jointly directed this study.

Simple Summary: Mouse polyomavirus (MPyV) is widely used as a model for cancer development studies. In many preceding studies, its tumorigenic potential was attributed to a virus protein called middle T antigen (MT), which possesses a transforming ability through activation of cell-associated tyrosine kinases, resulting in increased cell growth. Here, we studied the effects of the innate immune responses triggered by MPyV in mouse fibroblasts. We found that recognition of MPyV by Toll-like receptor 4 (TLR4), a sensor of the innate immunity system, induces the production of interleukin 6 (IL-6) and other cytokines without inhibiting virus multiplication. The cytokine microenvironment changed the phenotype of adjacent noninfected fibroblasts toward the cancer-associated fibroblast (CAF)-like phenotype associated with increased chemokine production and invasiveness. Thus, our data indicate that MPyV contributes to the CAF-like phenotype in mouse fibroblasts via a TLR4-driven inflammatory response.

Abstract: The tumorigenic potential of mouse polyomavirus (MPyV) has been studied for decades in cell culture models and has been mainly attributed to nonstructural middle T antigen (MT), which acts as a scaffold signal adaptor, activates Src tyrosine kinases, and possesses transforming ability. We hypothesized that MPyV could also transform mouse cells independent of MT via a Toll-like receptor 4 (TLR4)-mediated inflammatory mechanism. To this end, we investigated the interaction of MPyV with TLR4 in mouse embryonic fibroblasts (MEFs) and 3T6 cells, resulting in secretion of interleukin 6 (IL-6), independent of active viral replication. TLR4 colocalized with MPyV capsid protein VP1 in MEFs. Neither TLR4 activation nor recombinant IL-6 inhibited MPyV replication in MEFs and 3T6 cells. MPyV induced STAT3 phosphorylation through both direct and MT-dependent and indirect and TLR4/IL-6-dependent mechanisms. We demonstrate that uninfected mouse fibroblasts exposed to the cytokine environment from MPyV-infected fibroblasts upregulated the expressions of MCP-1, CCL-5, and α-SMA. Moreover, the cytokine microenvironment increased the invasiveness of MEFs and CT26 carcinoma cells. Collectively, TLR4 recognition of MPyV induces a cytokine environment that promotes the cancer-associated fibroblast (CAF)-like phenotype in noninfected fibroblasts and increases cell invasiveness.

Keywords: mouse polyomavirus; MPyV; mouse fibroblasts; CAF; TLR4; IL-6; spheroid invasiveness

Citation: Janovec, V.; Ryabchenko, B.; Škarková, A.; Pokorná, K.; Rösel, D.; Brábek, J.; Weber, J.; Forstová, J.; Hirsch, I.; Huérfano, S. TLR4-Mediated Recognition of Mouse Polyomavirus Promotes Cancer-Associated Fibroblast-Like Phenotype and Cell Invasiveness. *Cancers* **2021**, *13*, 2076. https://doi.org/10.3390/cancers13092076

Academic Editor: Claire Pecqueur

Received: 8 March 2021
Accepted: 21 April 2021
Published: 25 April 2021

1. Introduction

Polyomaviruses are DNA tumor viruses that are widely spread in nature; they infect mammals and birds. Serological studies and DNA sequencing have shown that polyomaviruses are highly prevalent in the human population. To date, 14 human polyomaviruses have been described. Among them, BK polyomavirus (BKPyV), JC polyomavirus (JCPyV), *Trichodysplasia spinulosa* polyomavirus, and Merkel cell virus (MCPyV) cause disease in humans. The oncogenic potential of the polyomaviruses was demonstrated several decades ago for simian polyomavirus virus 40 and for mouse polyomavirus (MPyV), but among the human viruses, MCPyV was not clearly linked to the development of skin cancer only in 2007 [1–3].

Currently, MPyV continues to be the best model to study tumorigenesis since, for the human MCPyV infection of primary dermal fibroblasts, specific conditions are needed [4]. MPyV induces a variety of tumors when inoculated in newborn mice [5]. Its tumorigenic potential has been studied for many years in cell culture models and was attributed mainly to the viral nonstructural middle T antigen (MT), which possesses high transforming ability [6,7]. MT is inserted into the endoplasmic reticulum membrane through the KDEL sequence at the C-terminus; from there, it migrates to the cell periphery [8]. MT localized on both endosomal and plasma membranes act as a scaffold signal adaptor, which activates Src tyrosine kinases [9,10], PI3K [11], PLC-γ1 [12], and PKB/Akt [13], and other cellular kinases. Modulation of cellular signaling by MT creates favorable conditions for viral replication, which can, under some circumstances, be reverted to cellular transformation [14]. Besides MPyV T antigens, host genetic variations and the immune response play an important role in the susceptibility to MPyV tumorigenesis [15].

In general, activation of the innate immune responses inhibits the initial viral spread and leads to proper activation of the adaptive immune response [16,17]. Velluipallai et al. [18] showed that Toll-like receptor (TLR) 4 is the key mediator of the cytokine response, which governs susceptibility to tumor development during MPyV infection. Particularly, the authors showed that polymorphism in TLR4 drives the differences in susceptibility to tumor induction by MPyV in the resistant mouse strain C57BR/cdJ (BR) in contrast to the susceptible mouse strain PERA/Ei (PEA). Antigen-presenting cells (APCs) from the BR strain recognize MPyV through TLR4 and produce IL-12, which induces the TH1 T cell response, whereas APCs from the PEA strain produce IL-10, which favors the TH2 cell response [18,19].

Many cytokines such as IL-6 or TNF-α are produced during wound healing in mice [20], and it was shown that cytokines like TGF-β and TNF-α increase replication of human polyomaviruses in vitro [21,22]. Moreover, the triggering of chronic inflammation by persistent viral infections has been clearly demonstrated [23]. Chronic inflammation is associated with hyperproduction of cytokines that support growth, promote immunosuppression of T lymphocytes, and are commonly present in the cancer environment [24,25]. For example, IL-6 overproduction by stromal cells supports tumor growth through STAT3 activation [26], promotes cancer-associated fibroblast (CAF)-induced cancer invasion, and was recently shown to promote resistance of cancer cells to therapy, proving its broad pro-tumorigenic role [27,28].

Several lines of evidence link persistent polyomavirus infection with inflammation-associated pathologies in humans. Results obtained on the mouse model support the role of polyomaviruses in chronic inflammation. MT-transformed endothelial cells (MT-ECs) continually secrete IL-6, which serves as both an autocrine and paracrine growth factor [29,30]. Consistently, MT-EC-transplanted mice treated with anti-IL-6 antibodies showed a lower frequency of metastases [29], supporting the notion that the cytokine environment drives tumorigenesis and metastasis formation [24]. Here, using a cell culture model, we addressed the question of whether TLR4 recognition of MPyV induces cytokine secretion in mouse fibroblasts, which alters fibroblast phenotype and promotes cell invasiveness in vitro.

2. Materials and Methods

2.1. Cell Lines and Virus

We grew 3T6 (ATCC; CCL-96) mouse fibroblasts, mouse embryonic fibroblasts (MEFs) (ATCC; CCL-13), and mouse CT26 colon carcinoma cells at 37 °C in a 5% CO_2-air humidified incubator using Dulbecco's modified Eagle's medium (DMEM; Sigma-Aldrich, Saint Louis, MO, USA) supplemented with 10% fetal bovine serum (Thermo Fisher Scientific, Waltham, MA, USA) and Pen/strep (Thermo Fisher Scientific). MPyV (BG strain) was purified from infected 3T6 cells and titrated as previously described [31]. Cell-free medium from MPyV-infected cells (MPyV-CM) was prepared with 10% sucrose cushion ultracentrifugation. The absence of MPyV virions in MPyV-CM was tested by flow cytometry. Total exosome isolation from MPyV-CM was performed with Total Exosome Isolation Reagent obtained from Thermo Fisher Scientific.

2.2. Inhibitors, Antibodies, and Reagents

TLR4 inhibitor CLI-095, TLR4 agonist lipopolysaccharide (LPS), TLR4 antagonist LPS-RS, JAK1/2 inhibitor ruxolitinib, and bafilomycin A1 were obtained from InvivoGen (San Diego, CA, USA). Recombinant mouse IL-6 was purchased from PeproTech (Cranbury, NJ, USA). siRNA targeting mouse TLR4 and control siRNA were purchased GE Healthcare Dharmacon (Lafayette, CO, USA). Lipofectamine RNAiMAX Transfection Reagent was obtained from Thermo Fisher Scientific. Mouse monoclonal antibody targeting mouse α-SMA was obtained from R&D systems (Minneapolis, MN, USA). Mouse monoclonal antibody anti-MPyV T antigens, mouse monoclonal antibody targeting MPyV LT antigen and rabbit polyclonal antibody targeting VP1 were used as described previously [31–33]. Mouse monoclonal antibodies targeting mouse TLR4 were purchased from Santa Cruz (Dallas, TX, USA) and Abcam (Cambridge, UK). Rabbit polyclonal antibody targeting mouse Rab11 and mouse monoclonal antibody targeting mouse ALIX were obtained from Santa Cruz. Mouse monoclonal IgG1 antibody targeting GAPDH was obtained from Thermo Fischer Scientific. Rabbit monoclonal antibody targeting STAT3, rabbit monoclonal antibody targeting phospho-STAT3 (Tyr705), and rabbit monoclonal antibody targeting phospho-STAT-3 (Ser727) were obtained from Cell Signaling Technology (Danvers, MA, USA). Goat anti-mouse monoclonal antibody conjugated with Alexa Fluor 488, goat anti-mouse monoclonal antibody conjugated with Alexa Fluor 546, and goat-anti-mouse conjugated with APC were purchased from Thermo Fisher Scientific. Donkey anti-rabbit monoclonal antibody conjugated with PE was obtained from Biolegend (San Diego, CA, USA).

2.3. Cell Stimulation In Vitro and Viral Infection

MEF and 3T6 cells were stimulated with 1 μg/mL LPS (Invivogen, San Diego, CA, USA). To inhibit TLR4 function, cells were pretreated with 10 μg/mL LPS-RS (Invivogen) or 1 μM CLI-095 (Invivogen) 1 h before LPS or MPyV addition. The 3T6 cells or MEFs were infected with MPyV at a multiplicity of infection (MOI) = 5 plaque-forming units (PFU)/cell (when not specified otherwise), diluted in serum-free medium for 1 h at 37 °C. After virus adsorption, complete DMEM medium with 10% FBS was added.

2.4. Immunofluorescence Staining and Confocal Microscopy

Cells were washed with PBS and then fixed with 4% formaldehyde in PBS for 15 min. Cells were then permeabilized with 0.5% Triton X-100 in PBS for 5 min and washed 3× with PBS. Cells were blocked with 1% BSA for 1 hour and incubated with rabbit polyclonal antibody to VP1 [31], mouse monoclonal anti-TLR4 antibody (Abcam), and rabbit polyclonal anti-Rab11 antibody (Santa Cruz). Mouse monoclonal antibody targeting mouse α-SMA (R&D systems) was used for α-SMA staining. We used goat anti-mouse conjugated with Alexa Fluor 488 and goat anti-rabbit conjugated with Alexa Fluor 546 as secondary antibodies. Images were obtained with a TCS SP8 confocal microscope (Leica, Wetzlar, Germany). Pearson's correlation coefficient (PCC) was calculated as previously described [34] using ImageJ [35] with the JaCoP plugin [36].

2.5. Measurement of IL-6 Secretion

The amount of IL-6 produced by 3T6 or MEFs was measured in cell-free supernatants using mouse ELISA kits (Mabtech, Stockholm, Sweden). Briefly, 3T6 or MEFs were stimulated by LPS or infected with MPyV, and cell-free supernatants were collected 24 h post-stimulation or -infection. Supernatants were centrifuged and analyzed according to the manufacturer's protocol.

2.6. Determination of IL-6, CCL2 /MCP-1, SDF-1, α-SMA, and IP-10 Expression

Total cellular RNA was isolated using a High Pure RNA Isolation Kit (Roche). cDNA was synthesized using an iScript cDNA Synthesis Kit (Biorad, Hercules, CA, USA). The mRNA of interest was amplified with a LightCycler 480 SYBR Green I Masterkit (Roche, Basel, Switzerland) using the following primers: IL-6: forward: 5′-CGTGGAAATGAGAAA AGAGTTGTGC-3′ and reverse 5′-CAGGTAGCTATGGTACTCCAGAAG-3′; CCL2/MCP1: forward: 5′-AAGACTGAATGGCTGGATGGC-3′; SDF-1: forward: 5′-AACTCGCTCCTC CCTCTTCG-3′ and reverse 5′-GGGAAGAGTTTACCGTCAGGT-3′; α-SMA: forward: 5′-CTACGAACTGCCTGACGGG-3′ and reverse 5′- GCTGTTATAGGTGGTTTCGTGG-3′; IP-10: forward: 5′-TGCAGGATGATGGTCAAGCC-3′ and reverse 5′-CACTTGAGCG AGGACTCAGA-3′; and Ppia: forward: 5′-AAGACTGAATGGCTGGATGGC-3′ and reverse 5′-CATTCCTGGACCCAAAACGC-3′. Relative expression levels were calculated using the $2^{-\Delta\Delta CT}$ method. Mouse peptidylprolyl isomerase A (Ppia) was used as the endogenous control.

2.7. TLR4 Silencing Using siRNA

MEFs were plated to 70% confluency 1 day before transfection. Then, siRNA against TLR4 or control siRNA was transfected using RNAiMAX (Thermo Fisher Scientific). TLR4 expression was analyzed 48 h post-transfection by Western blot.

2.8. Determination of STAT3 Phosphorylation, Alpha-SMA, ALIX, and TLR4 by Immunoblotting

Total STAT3 and alpha-SMA in the whole cell lysate of MEFs were determined by Western blot using of rabbit monoclonal antibody targeting STAT3 (Cell Signaling using Technology) and mouse monoclonal antibody targeting mouse α-SMA (R&D systems). Phosphorylation of STAT3 in the whole cell lysate of MEF cells was analyzed by Western blot using rabbit monoclonal antibody targeting phospho-STAT3 (Tyr705) (Cell Signaling Technology) and rabbit monoclonal antibody targeting phospho-STAT-3 (Ser727) (Cell Signaling Technology). ALIX was determined in exosomes isolated from MPyV-CM by Western blot using mouse monoclonal antibody targeting ALIX (Santa Cruz). After incubation with the appropriate horseradish peroxidase-conjugated secondary antibody, the membranes were washed, and the protein bands were detected with SuperSignal West Femto Maximum Sensitivity Substrate (Thermo Fisher Scientific). Densitometric analyses were performed using an Amersham Imager 600 (GE Healthcare Life Science, Marlborough, MA, USA). Band intensities were normalized to GAPDH detected by mouse monoclonal antibody targeting GAPDH (Thermo Fisher Scientific). The whole un-cropped images of Western blots are shown in Figure S1.

2.9. Determination of STAT3 Phosphorylation and MPyV Infection of MEFs by Flow Cytometry

To determine MPyV-infected cells by flow cytometry, MEFs or 3T6 cells were trypsinized and fixed with 4% formaldehyde in PBS for 15 min. Cells were then permeabilized with 0.1% Triton X-100 in PBS for 5 minutes and washed 3× with PBS. Cells were incubated with the mouse monoclonal anti-MPyV T-antigen common region. For flow cytometry analysis of phospho-STAT3 (Tyr705), cells were fixed in 4% formaldehyde for 10 min, permeabilized by 90% methanol for 30 min, and stained by rabbit monoclonal antibody targeting phospho-STAT3 (Tyr705) (Cell Signaling Technology). We used goat anti-mouse conjugated with APC (Thermo Fisher Scientific) and donkey anti-rabbit conjugated with PE (Biolegend). Live/dead cell discrimination was performed using a Zombie Green™

Fixable Viability Kit (BioLegend). Samples were analyzed using a BD LSR FORTESSA cytometer (BD Biosciences, San Jose, CA, USA), and data were processed using FLOWJO software (Treestar, San Carlos, CA, USA).

2.10. Cell Invasiveness Assay

Cells were grown in micro-mold 3D Petri Dish Microtissues (Merck, Darmstadt, Germany) according to the manufacturer's protocol for 2 days to obtain multicellular spheroids of defined size. Then, the spheroids were transferred and embedded into a 3D collagen matrix (final composition 1 mg/mL rat tail collagen, 1 × RPMI medium, 15 mM HEPES, 1% fetal bovine serum, and 50 µg/mL gentamicin) and overlaid with either conditioned medium from MPyV-infected MEFs (MPyV-CM) or control conditioned medium from noninfected MEFs (MOCK-CM). In the case of inhibitor treatment, 1 µM ruxolitinib or an equivalent amount of DMSO was added to the overlaying conditioned medium. Images of spheroids were taken immediately after embedding into collagen (0 h) and after invasion (48 h) using a Nikon ECLIPSE TE2000-S microscope. The area of the spheroids before and after invasion was measured using FiJi software, and the relative invasion index was calculated. The data were statistically analyzed in GraphPad Prism 6 (GraphPad Software, La Jolla, CA, USA) using one-way ANOVA. The presented data are summarized from 3 independent biological replicates, and a minimum of 5 spheroids per condition and replicate were analyzed.

2.11. Statistical Analysis

Quantitative variables are expressed as the mean ± standard error of the mean (SEM). To compare the levels of cytokine production and transcription of mRNA by MEFs and 3T6 cells, we used the Mann–Whitney test and a two-tailed *t*-test. For flow cytometry analyses, we used a two-tailed *t*-test. For the cell invasiveness assay, we used one-way ANOVA. For TLR4/VP1 colocalization, we used Kolmogorov–Smirnov test. Data were analyzed with GraphPad Prism 6 (GraphPad Software). A *p*-value of ≤ 0.05 was considered significant.

3. Results

3.1. Mouse Embryonic Fibroblasts and 3T6 Cells Recognize MPyV through TLR4 and Secrete IL-6

The ability of mouse macrophages to recognize MPyV particles by TLR4 and secrete various cytokines [18] led us to investigate whether MEFs recognize MPyV infection in a similar way. We measured IL-6 secretion by MEFs infected with MPyV (MOI = 5) or, as a control, in MEFs stimulated with TLR4 agonist LPS. To further confirm the specific TLR4 activation, TLR4 was inhibited by pretreatment with LPS-RS (TLR4 antagonist) or by CLI-095 (TLR4 inhibitor) (Figure 1a). Both MPyV-infected MEFs and LPS-stimulated MEFs produced significant amounts of IL-6. Pretreatment of MEFs exposed to MPyV or LPS with TRL4 antagonist LPS-RS and TLR4 inhibitor CLI-095 led to the inhibition of IL-6 secretion (Figure 1a). Next, we investigated whether the multiplicity of infection influences IL-6 secretion and whether 3T6 fibroblast cells are able to recognize MPyV. The 3T6 cells were infected with various MOI, and IL-6 secretion was measured until 7 days post-infection (Figure 1b). IL-6 secretion by 3T6 cells was time-dependent and correlated with the level of MOI. To verify the hypothesis that TLR4 recognizes the virus but does not require the viral nuclear phase (transcription/replication), we used bafilomycin A1. Bafilomycin A1 inhibits the vacuolar H^+-ATPase preventing endosomal acidification. In MPyV infection, this drug causes viral accumulation in early endosomes, thereby preventing further viral trafficking. We previously showed that bafilomycin A1 reduces MPyV replication in 3T6 cells by 90% [32]. Here, cells were treated with bafilomycin and infected with MPyV or, as a control, with LPS. We observed that IL-6 production was inhibited (Figure 1c) neither in the MPyV infection nor in the LPS control (Figure 1c). Thus, active viral replication is not necessary for IL-6 production. Collectively, MEFs and 3T6 cells recognized MPyV infection, and the TLR4 recognition of MPyV was dose-dependent, although it was independent of active viral replication.

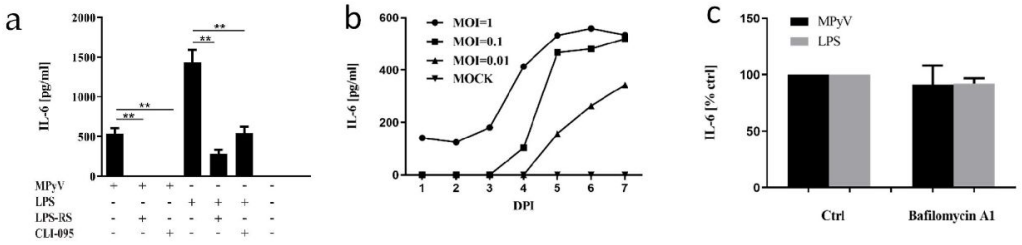

Figure 1. Toll-like receptor 4 (TL4)-mediated recognition of mouse polyomavirus (MPyV) in mouse fibroblasts. (**a**) The production of interleukin (IL)-6 by mouse embryonic fibroblast (MEFs) stimulated with lipopolysaccharide (LPS) or infected with MPyV (multiplicity of infection (MOI) = 5) in the presence of LPS-RS or CLI-095. (**b**) The kinetics of IL-6 secretion by 3T6 cells infected with MPyV with various MOI, 7 days post-infection (DPI). (**c**) The effect of bafilomycin A1 pretreatment on IL-6 secretion by 3T6 cells infected with MPyV (MOI = 5) or stimulated with LPS. ** $p < 0.01$; two-tailed Mann–Whitney test.

3.2. *TLR4 Colocalizes with MPyV Capsid Protein VP1 in MEF*

We showed earlier that MPyV particles enter cells in monopinocytic vesicles that are further sorted through the endosomal system and localized to various endosomal components including Rab5-, Rab7-, and Rab11-positive endosomes [33]. Here, we infected MEFs and analyzed whether the TLR4 receptor also colocalizes with the virus in the endosomes using confocal microscopy. We observed colocalization of MPyV (detected by VP1 capsid protein staining) and TLR4 as early as 2 h post-infection (2 hpi) at a high virus input (MOI = 10). As a result, large clusters of TL4-VP1 were detected (Figure 2a). At the same time point, we followed MEFs infected with low virus input (MOI = 1) and observed only sporadic colocalization of MPyV (VP1) and TLR4. Conversely, very strong colocalization of TLR4 and VP1 at low virus input (MOI = 1) was observed 4 days post-infection (4 dpi) (Figure 2b), as quantified using Pearson's correlation coefficient (PCC) by including pixels that co-localize between both channels. PCC values can range from +1 (perfect correlation) to −1 (perfect anti-correlation) (Figure 2c). The colocalization between VP1 and TLR4 was greater at 4 dpi than at 2 hpi. In addition, since Rab11 endosomes, which are a part of the route of sorting of MPyV, play an essential role in the trafficking of TLR4 during activation, we followed mutual colocalization of Rab11 and TLR4 in MPyV-infected MEFs and MOCK-treated MEFs. We observed colocalization between TLR4 and Rab11 in infected MEFs (Figure 2d). Thus, our data showed that the virus colocalizes with TLR4 in the endosomal compartments and that TLR4 is internalized to Rab11-positive endosomal compartments during MPyV infection of MEFs.

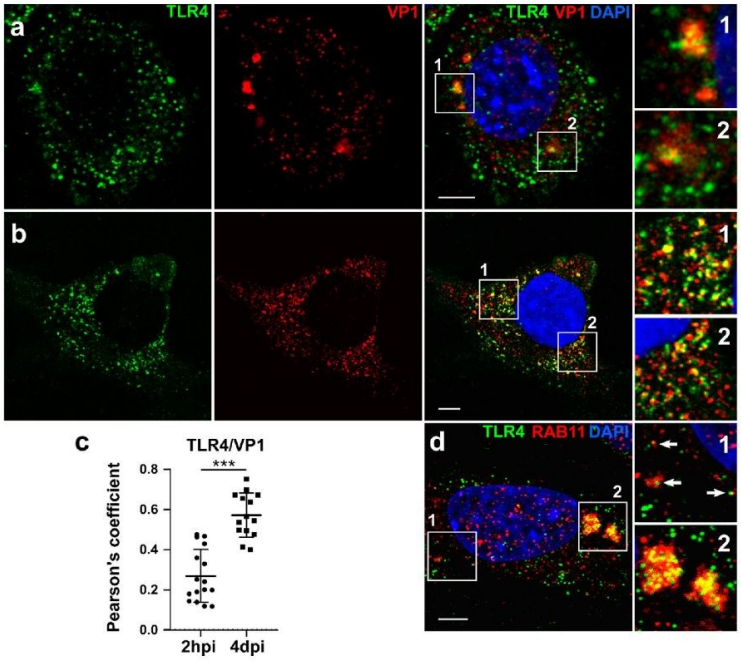

Figure 2. Colocalization of TLR4 and VP1 in MEFs. (**a**) Confocal section of MEFs infected with MPyV at a high virus input (MOI = 10). VP1 (red) and TLR4 (green) were stained by specific antibodies and DNA by DAPI. Colocalization of VP1 and TLR4 was analyzed 2 h post-infection. (**b**) Confocal section of MEFs infected with MPyV at a low virus input (MOI = 1). VP1 (red) and TLR4 (green) were stained by specific antibodies and DNA by DAPI. Colocalization of VP1 and TLR4 was analyzed 4 days post-infection. (**c**) Colocalization between intracellular virus and TLR4, expressed as Pearson′s coefficient. (**d**) Confocal section of MEFs infected with MPyV at a high virus input (MOI = 10). Rab11 (red) and TLR4 (green) were stained by specific antibodies, DNA by DAPI. Colocalization of Rab11 and TLR4 was analyzed 2 h post-infection. White squares show enlarged regions of VP1 and TLR4 or TLR4 and Rab11 colocalizations. Bars = 10 μm. *** $p < 0.001$; Kolmogorov–Smirnov test.

3.3. Neither TLR4 Activation Nor Recombinant IL-6 Inhibits MPyV Replication in MEFs and 3T6 Cells

TLR4 activation in MEFs or 3T6 cells led to the production of proinflammatory cytokine (Figure 1). In primary human hepatocytes, TLR4 stimulation inhibits HBV replication [37]. We tested whether pharmacologic targeting of TLR4 signaling with CLI-095 affects MPyV replication in MEFs determined by the expression of T antigens (Figure 3a). Inhibition of TLR4 signaling in MEFs by CLI-095 did not lead to the decrease in T-antigen-positive MEFs. The same result was obtained with 3T6 cells (Figure S2). It was previously reported that human polyomavirus BKPyV is highly resistant to proinflammatory cytokines [38]. Thus, we stimulated TLR4 in 3T6 cells with LPS or exposed the cells to recombinant IL-6 and IFN-γ 24 h prior to MPyV infection. Consistent with previously published data [39], only IFN-γ pretreatment inhibited MPyV infection in 3T6 cells (Figure 3b). Then, we confirmed our results with siRNA targeting TLR4 in MEFs (Figure 3c,d). TLR4 silencing reduced IL-6 production in MEFs induced by both MPyV and LPS (Figure 3d), while the quantity of large T-antigen (LT) was unchanged (Figure 3c). Altogether, our results demonstrated the nonprotective role of TLR4 activation against MPyV infection in MEFs and 3T6 cells.

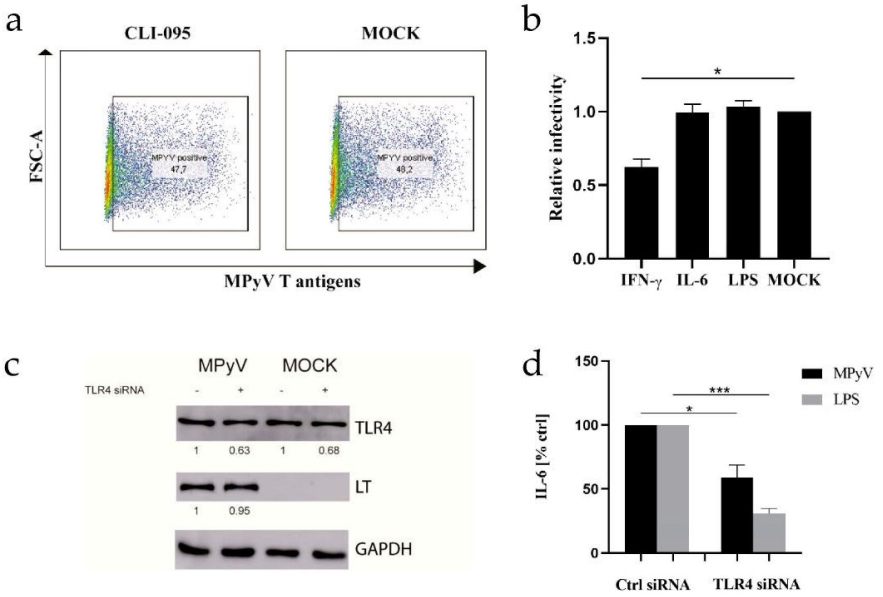

Figure 3. Effect of TLR4 signaling on MPyV lifecycle in MEFs. (**a**) Flow cytometry analysis of the percentage of MPyV-positive MEFs determined by expression of T antigens in the presence or absence (MOCK) of TRL4 inhibitor CLI-095 (10 μM) (**b**) Relative infectivity of MPyV in 3T6 cells pretreated with IFN-γ (100 IU/mL), IL-6 (10 ng/mL), LPS (10 μg/mL) or mock-treated (MOCK) determined by expression of T antigens. Relative infectivity was assessed by flow cytometry, and data were normalized to MOCK. (**c**) The effect of TLR4 silencing on TLR4 and LT levels in MPyV-infected MEFs was followed by Western blot. The values shown below each band represent the relative quantity of TLR4 or LT determined by densitometry normalized to the MOCK-infected MEFs treated with control siRNA. GAPDH was used as a loading control. (**d**) The effect of TLR4 silencing on the IL-6 production in MEFs infected with MPyV or stimulated with LPS measured by ELISA. * $p < 0.05$; *** $p < 0.001$; two-tailed *t*-test.

3.4. MPyV Induces STAT3 Phosphorylation via IL-6

Since TLR4 activation did not inhibit MPyV replication in MEFs and 3T6 cells, we decided to test whether TLR4-mediated IL-6 secretion affects cell signaling. Similar to MT, which promotes STAT3 activation [40], IL-6 also induces STAT3 phosphorylation [41]. First, we showed that T-antigen-positive MEFs contain elevated levels of phosphorylated STAT3 at Y705 compared to T-antigen-negative MEFs using PhosphoFlow cytometry (Figure 4a). Then, we analyzed the effect of the cytokine environment induced by TLR4 recognition of MPyV on STAT3 phosphorylation in noninfected MEFs. We prepared conditioned media (CM) from MPyV-infected fibroblasts (MPyV-CM) or control media from MOCK-infected fibroblasts (MOCK-CM) by ultracentrifugation in a 10% sucrose cushion to separate infectious viral particles (present in pellets) from cytokines (present in the supernatant). We confirmed the presence of IL-6 (600–800 pg/mL) in MPyV-CM by ELISA. Because IL-6 is known to be associated with and transferred by exosomes [42,43], and we detected an exosome marker ALIX in the exosomal pellet of MPyV-CM by Western blot (Figure S3a), we quantified IL-6 level in exosomes isolated from MPyV-CM. IL-6 was not detected in the isolated exosomes by ELISA (Figure S3b). No virus infectivity was detected after MPyV-CM treatment of MEFs. We assessed whether cytokines, including IL-6 present in MPyV-CM, induce STAT3 phosphorylation at Y705 and S727 by means of Western blot. MPyV-CM significantly elevated the phosphorylation of STAT3 in MEFs, whereas MOCK-CM did not (Figure 4b). To elucidate whether the cytokine environment is

responsible for the induction of STAT3 phosphorylation in MEFs, we used JAK1/2 inhibitor ruxolitinib and anti-IL-6 antibodies. Both anti-IL6 antibodies and ruxolitinib decreased the phosphorylation of STAT3 at Y705 (Figure 4c). Thus, our results disclosed a dual mechanism of STAT3 activation due to the presence of MT in MPyV-infected MEFs and IL-6 present in the supernatant.

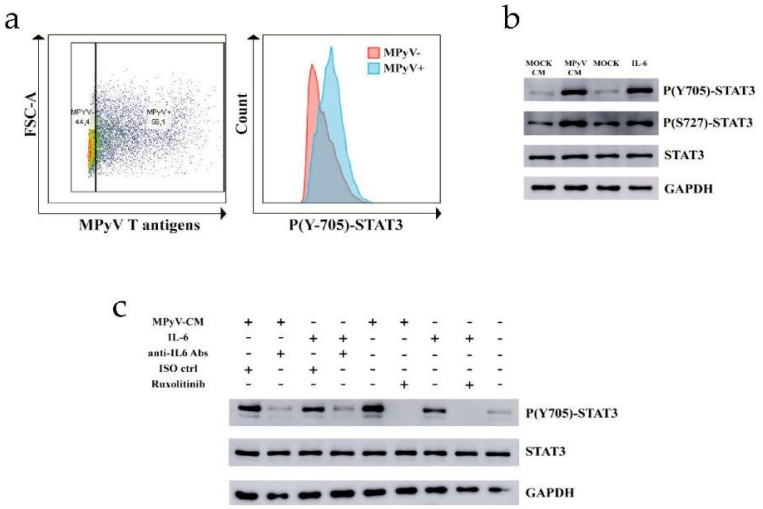

Figure 4. Induction of STAT3 phosphorylation in MEFs by MPyV-CM. (**a**) Fluorescence intensity of STAT3 phosphorylation at Y705 in T-antigen-positive or -negative MEFs. MEFs were infected with MPyV to reach approximately 50% T-antigen-positive cells to assess the distribution of STAT3 phosphorylation in one sample using PhosphoFlow. Red-colored histogram represents T-antigen-negative MEFs, whereas blue-colored histogram represents T-antigen-positive MEFs. (**b**) Western blot analysis of STAT3 phosphorylation at Y705 and S727 in MEFs treated with MPyV-CM or MOCK-CM. Recombinant IL-6 (10 ng/mL) was used as the positive control. Total STAT3 and GAPDH served as the loading control. (**c**) The effect of anti-IL-6 antibodies (Abs) and JAK1/2 inhibitor Ruxolitinib on the MPyV-CM-induced STAT3 phosphorylation at Y705. As a control for anti-IL-6 antibodies, an isotype antibody control (ISO ctrl) was included. The results are representative of three independent experiments.

3.5. MPyV Infection Induces Cytokine Environment That Changes MEF Phenotype

Quiescent fibroblasts exposed to CM from cancer organoids alter the phenotype to CAFs and support tumor growth [44]. Thus, we tested whether MPyV-CM treatment can alter the MEF phenotype. First, we analyzed the expression of alpha-smooth muscle actin (α-SMA), which serves as a marker of CAFs [45]. We found that α-SMA expression was elevated in MPyV-CM-treated MEFs compared with MOCK-CM-treated MEFs (Figure 5a). Then, we analyzed the α-SMA structure using confocal microscopy. α-SMA formed vigorous bundles in MPyV-CM-treated MEFs compared with MOCK-CM-treated MEFs. Thus, not only higher expression but also morphological changes in α-SMA were observed in MPyV-CM-treated MEFs (Figure 5b). Conversion of normal fibroblast to CAFs is associated with the secretion of various cytokines/chemokines, which support the cancer environment [46]. As such, we analyzed the mRNA levels of SDF-1, MCP-1, CCL-5, and α-SMA in MPyV-CM-treated MEFs (Figure 5c). Except for SDF-1, we detected high levels of transcription of CAF-associated cytokines in MPyV-CM-treated MEFs.

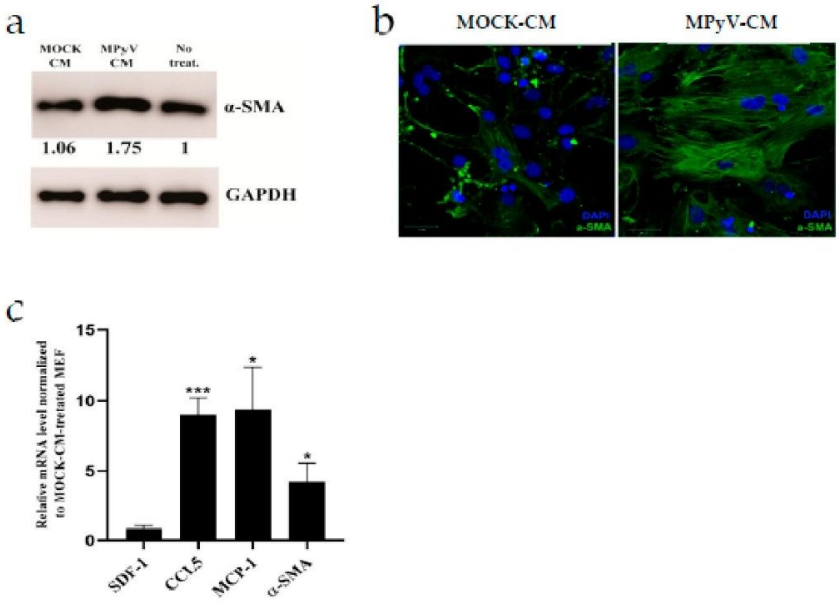

Figure 5. MPyV infection induces a cytokine environment that changes the fibroblast phenotype. (**a**) Analysis of alpha-smooth muscle actin (α-SMA) expression in MEFs treated with MPyV-CM or MOCK-CM. The values shown below each band represent the relative quantity of α-SMA determined by densitometry normalized to non-treated MEF. GAPDH was used as the loading control. The α-SMA expression was analyzed 48 h post-treatment. (**b**) Confocal images of α-SMA distribution in MEFs treated with MPyV-CM or MOCK-CM. Laser settings and acquisition conditions were constant for both samples. The α-SMA distribution was analyzed 48 hours post-treatment. (**c**) The qPCR analysis of relative mRNA levels in MEFs treated with MPyV-CM. The qPCR analysis was performed 48 h post-treatment. Relative mRNA level was normalized to MOCK-CM-treated MEFs. Mouse Ppia was used as the endogenous control. The data are the mean ± SEM of four independent experiments. * $p < 0.05$; *** $p < 0.001$; two-tailed *t*-test.

3.6. MPyV Infection in Fibroblasts Establishes Cytokine Environment That Supports Cell Invasiveness

CAFs promote the invasive behavior of cancer cells by both direct and indirect mechanisms [45]. It was also reported that MT-expressing endothelial cells produce IL-6 and induce recruitment of host endothelial cells in vivo [29]. Thus, we tested whether cytokines produced by MPyV-infected fibroblasts can also alter cell invasiveness. To this end, we employed spheroid invasion assays in 3D collagen gels, which are used to mimic in vitro cell dissemination in 3D conditions [47]. We cultured noninfected MEFs (Figure 6a) and mouse colon carcinoma cell line CT26 (Figure 6b) as spheroids and supplemented them with MPyV-CM or MOCK-CM. MPyV-CM significantly increased the spheroid invasion in both cell types. Next, we tested whether JAK1/2 inhibitor ruxolitinib is able to block spheroid invasion. Ruxolitinib pretreatment decreased spheroid invasion in MPyV-CM-treated MEFs (Figure 6c) but not in CT26 cells (Figure 6d), pointing to a difference between primary embryonic fibroblast and cancer-derived cell-line invasiveness. Collectively, MPyV-infected fibroblasts secrete cytokines that affect cellular motility. In particular, the ability of ruxolitinib to significantly inhibit cell invasion shows that IL-6 or other JAK1/2-activating cytokines contribute to the increased invasive behavior of MEFs.

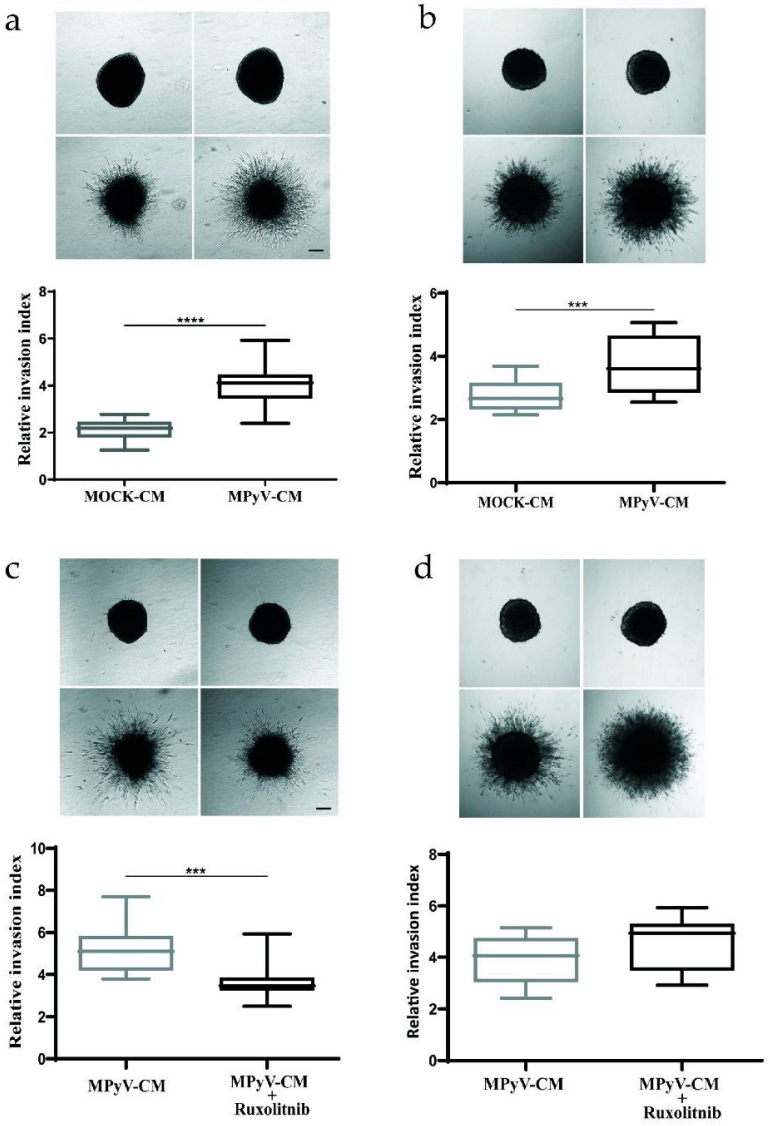

Figure 6. MPyV-induced cytokine environment promotes cell invasiveness. (**a**) Invasiveness of MEF cell-spheroid in a 3D collagen matrix in the presence of MPyV-CM or MOCK-CM. (**b**) Invasiveness of CT26 cell-spheroid in a 3D collagen matrix in the presence of MPyV-CM or MOCK-CM. (**c**) The effect of JAK1/2 inhibitor ruxolitinib on MPyV-CM-mediated MEF spheroid invasiveness a 3D collagen matrix. (**d**) The effect of JAK1/2 inhibitor ruxolitinib on MPyV-CM-mediated CT26 spheroid invasiveness in a 3D collagen matrix. The data are the mean ± SEM of three independent experiments with a minimum of five spheroids per condition. The spheroid invasiveness was analyzed 48 h post-treatment. *** $p < 0.001$; **** $p < 0.0001$; one-way ANOVA test.

4. Discussion

In this study, we found that TLR4-mediated recognition of MPyV in MEF and 3T6 cells led to the formation of a cytokine environment that did not affect MPyV replication. Our data suggest a novel mechanism, where MPyV replication promotes a CAF-like phenotype in adjacent noninfected fibroblasts and increases the cell invasiveness of primary embryonic cells and cancer-derived cells in vitro.

TLR4-mediated recognition of MPyV in MEF and 3T6 cells led to the secretion of proinflammatory cytokine IL-6 and was virus-dose-dependent. We did not observe any cytokine production 24 h post-infection from 3T6 cells when a low viral input was used. However, IL-6 production increased progressively over time, suggesting that uncontrolled viral propagation surpasses the TLR4 activation threshold [48]. When we blocked MPyV infection with bafilomycin A1, IL-6 secretion was not reduced. This is consistent with a previous report showing that MPyV virus-like particles containing only VP1 capsid protein activated the innate immune response in mice [19]. Altogether, we confirmed by TLR4 antagonist LPS-RS, TLR4 inhibitor CLI-095, and TLR4 siRNA targeting that TLR4 is a key mediator of the cytokine response in MPyV-infected MEFs. Our results are consistent with previously published data on TLR2/TLR4 double-knockout macrophages, in which the TLR4 cDNA from BR mice conferred a robust IL-12 response to MPyV [18].

Surprisingly, we did not observe any effect of TLR4 activation or inhibition on MPyV replication in MEFs and 3T6 cells. Recombinant IL-6 did not show any significant effect on MPyV replication in mouse fibroblasts. Similar to our findings, replication of BKPyV is resistant to proinflammatory cytokines [40]. Only IFN-γ was able to inhibit MPyV infection [41]. Silencing of TLR4 reduced the amount of IL-6 produced by MEFs; however, the level of LT antigen was unchanged. We observed TLR4 clusters after MPyV infection that colocalized with Rab11. We previously showed that sorting Rab11-positive recycling endosomes did not represent a productive pathway for the infection of MPyV, and viral particles in them were observed only in a low quantity (14.9 $\pm$ 0.9%) [33]. Moreover, MPyV viral particles also localize in Rab5-, Rab7-, Rab11-, LAMP-2-, and caveolin-positive endosomes [33,49]. Our results indicate that trafficking of TLR4 to Rab11 endosomes may be a part of the sorting of the receptor that occurs during TLR4 activation [50]. It has been shown that Rab11 can translocate from recycling endosomes to autophagosomes in response to autophagy induction and assist in the fusion of late endosomes with autophagosomes [51]. Crispr/Cas9 targeting of TLR4 or MEFs from TLR4-knockout mice could be used for specific localization of TLR4 and MPyV in future experiments to decipher the connection of TLR4 with MPyV trafficking.

IL-6 is a multi-functional cytokine that plays roles not only in viral defense but also in the pathogenesis of viral diseases. Exogenous recombinant IL-6 activates STAT3 transcription factor, which is also activated by MPyV MT and is associated with MPyV-induced cell transformation in vitro [42]. MPyV-CM induced strong STAT3 phosphorylation in MEF despite a lower amount of IL-6 in MPyV-CM (600–800 pg/mL) compared to recombinant IL-6 (10 ng/mL). Crosstalk between other cytokines/chemokines and IL-6/STAT3 signaling pathway could be responsible for the MPyV-CM-induced STAT3 phosphorylation. Moreover, exosomes present in MPyV-CM can potentially transfer IL-6 [43], although no IL-6 was detected in the exosome isolated from MPyV-CM by ELISA. More precise analysis of exosomes in a culture medium supplemented with exosome-depleted FBS and more sensitive detection of IL-6 are needed to exclude the role of exosomal IL-6. Altogether, our and other results have shown that MPyV activates STAT3 by phosphorylation directly through MT and indirectly via TLR4-mediated IL-6 production [42].

CAFs represent variable fibroblast populations with several specific effects such as α-SMA expression, cytokine/chemokine secretion, and extracellular matrix remodeling [45]. Soluble factors such as proinflammatory cytokines IL-1-β or IL-6 promote the pro-tumorigenic fibroblast phenotype [44,46]. We found that CM from MPyV-infected MEFs alters normal MEFs to express more α-SMA. Higher α-SMA expression in MEFs was also connected with a higher level of mRNAs encoding CCL5 and MCP-1 chemokines.

Several studies reported that CAF-mediated production of CCL5 and MCP1 modulates the cancer environment [52,53]. Our data showed that MPyV replication in MEFs induces a cytokine environment, which promotes the CAF-like phenotype in fibroblasts. MPyV resembles human papillomaviruses that also alter fibroblast phenotype through the IL-6/STAT3 pathway [54,55]. Further investigation is necessary to clarify whether persistent MPyV infection alters the fibroblast phenotype in vivo.

Injection of mice with MT-expressing mouse endothelial cells that secrete soluble factors induced rapid recruitment of host non-transformed endothelial cells into the site of injection [34,52]. Moreover, supernatants from MT-expressing mouse endothelial cells stimulated in vitro invasiveness of cancer cell lines [56]. Thus, we investigated whether the MPyV-induced cytokine environment affects the cell invasiveness of MEFs or the colon carcinoma cell line, CT26. Both MEFs and CT26 migrated more efficiently in the presence of CM from MPyV-infected MEFs, and the migratory effect was inhibited by JAK1/2 inhibitor ruxolitinib in the case of MEFs. However, the lack of ruxolitinib effect on CT26 cell invasiveness suggested that cancer cells are able to circumvent the inhibition of JAK1/2 using an alternative pathway. In addition, the conditioned medium from MPyV-infected MEFs contains several soluble factors, which may have different cellular specificities, and induces both JAK1/2-dependent and -independent increases in cellular invasiveness. This finding is consistent with that of a previous study in which several soluble factors affecting cellular motility were identified in supernatants from MT-expressing endothelial cells [56].

5. Conclusions

Here, we demonstrated that mouse fibroblasts recognize viral MPyV particles by TLR4 and created a cytokine environment that is nonprotective against MPyV, increases cellular motility, and changes the phenotype of noninfected fibroblasts toward CAF-like phenotype. Aberrant TLR4 activation in the cancer environment can support tumor growth [57,58]. Thus, active MPyV replication contributes to tumor formation also via a TLR4-driven chronic inflammatory response. Demonstration of the hijacking of the TLR4 pathway in mouse fibroblasts by infecting MPyV illustrates a subtle equilibrium between the antiviral and proviral tumorigenic roles of innate immunity in different cell contexts.

Supplementary Materials: The following are available online at https://www.mdpi.com/article/10.3390/cancers13092076/s1, Figure S1: Western blots, Figure S2: Effect of TLR4 signaling on MPyV lifecycle in 3T6 cells. Flow cytometry analysis of the percentage of MPyV positive MEFs determined by expression of T antigens in the presence or absence (MOCK) of TRL4 inhibitor CLI-095 (10 μM).

Author Contributions: All authors contributed to this work. Conceptualization, V.J., B.R., and I.H.; methodology, V.J., B.R., A.Š., D.R., J.B., and I.H.; validation, V.J., B.R., and A.Š.; formal analysis, V.J., B.R., A.Š., K.P., D.R., J.B., J.F., I.H., and S.H.; investigation, V.J., B.R., A.Š., and K.P.; data curation, D.R., J.B., and S.H.; writing—original draft preparation, V.J.; writing—review and editing, V.J., B.R., A.Š., S.H., D.R., K.P., J.B., J.W., J.F., and I.H.; visualization, V.J., B.R., and A.Š.; supervision, J.F., I.H., and S.H.; project administration, V.J. and I.H.; funding acquisition, J.W., J.F., I.H., and S.H. All authors have read and agreed to the published version of the manuscript.

Funding: This research was funded by institutional grants from Charles University, GAUK-644217 (Vaclav Janovec), GAČR 19-14445S (B.R., J.F., S.H.), and SVV 260568.

Data Availability Statement: The data presented in this study are available in supplementary material here.

Acknowledgments: We are grateful to the Imaging Methods Core Facility (IMCF) at BIOCEV (supported by the MEYS CR [Large RI Project LM2018129 Czech-Bioimaging] and ERDF [project No. CZ.02.1.01/0.0/0.0/18_046/0016045]) for their expert assistance.

Conflicts of Interest: The authors declare no conflict of interest.

References

1. Lee, W.; Langhoff, E. Polyomavirus in human cancer development. *Adv. Exp. Med. Biol.* **2006**, *577*, 310–318. [CrossRef] [PubMed]
2. Gheit, T.; Dutta, S.; Oliver, J.; Robitaille, A.; Hampras, S.; Combes, J.D.; McKay-Chopin, S.; Le Calvez-Kelm, F.; Fenske, N.; Cherpelis, B.; et al. Isolation and characterization of a novel putative human polyomavirus. *Virology* **2017**, *506*, 45–54. [CrossRef] [PubMed]
3. Cook, L. Polyomaviruses. *Microbiol. Spectr.* **2016**, *4*. [CrossRef] [PubMed]
4. Liu, W.; Yang, R.; Payne, A.S.; Schowalter, R.M.; Spurgeon, M.E.; Lambert, P.F.; Xu, X.; Buck, C.B.; You, J. Identifying the Target Cells and Mechanisms of Merkel Cell Polyomavirus Infection. *Cell Host. Microbe* **2016**, *19*, 775–787. [CrossRef] [PubMed]
5. Benjamin, T.L. Polyoma virus: Old findings and new challenges. *Virology* **2001**, *289*, 167–173. [CrossRef]
6. Fluck, M.M.; Schaffhausen, B.S. Lessons in Signaling and Tumorigenesis from Polyomavirus Middle T Antigen. *Microbiol. Mol. Biol. Rev.* **2009**, *73*, 542–563. [CrossRef] [PubMed]
7. Gottlieb, K.A.; Villarreal, L.P. Natural Biology of Polyomavirus Middle T Antigen. *Microbiol. Mol. Biol. Rev.* **2001**, *65*, 288–318. [CrossRef]
8. Zhou, A.Y.; Ichaso, N.; Adamarek, A.; Zila, V.; Forstova, J.; Dibb, N.J.; Dilworth, S.M. Polyomavirus Middle T-Antigen Is a Transmembrane Protein That Binds Signaling Proteins in Discrete Subcellular Membrane Sites. *J. Virol.* **2011**, *85*, 3046–3054. [CrossRef]
9. Courtneidge, S.A. Activation of the pp60c-src kinase by middle T antigen binding or by dephosphorylation. *EMBO J.* **1985**, *4*, 1471–1477. [CrossRef]
10. Dunant, N.M.; Senften, M.; Ballmer-Hofer, K. Polyomavirus middle-T antigen associates with the kinase domain of Src-related tyrosine kinases. *J. Virol.* **1996**, *70*, 1323–1330. [CrossRef]
11. Utermark, T.; Schaffhausen, B.S.; Roberts, T.M.; Zhao, J.J. The p110α Isoform of Phosphatidylinositol 3-Kinase Is Essential for Polyomavirus Middle T Antigen-Mediated Transformation. *J. Virol.* **2007**, *81*, 7069–7076. [CrossRef]
12. Su, W.; Liu, W.; Schaffhausen, B.S.; Roberts, T.M. Association of Polyomavirus Middle Tumor Antigen with Phospholipase C-γ1. *J. Biol. Chem.* **1995**, *270*, 12331–12334. [CrossRef]
13. Meili, R.; Cron, P.; Hemmings, B.A.; Ballmer-Hofer, K. Protein kinase B/Akt is activated by polyomavirus middle-T antigen via a phosphatidylinositol 3-kinase-dependent mechanism. *Oncogene* **1998**, *16*, 903–907. [CrossRef]
14. Freund, R.; Sotnikov, A.; Bronson, R.T.; Benjamin, T.L. Polyoma virus middle T is essential for virus replication and persistence as well as for tumor induction in mice. *Virology* **1992**, *191*, 716–723. [CrossRef]
15. Swanson, P.A.; Lukacher, A.E.; Szomolanyi-Tsuda, E. Immunity to polyomavirus infection: The polyomavirus-mouse model. *Semin. Cancer Biol.* **2009**, *19*, 244–251. [CrossRef]
16. Palm, N.W.; Medzhitov, R. Pattern recognition receptors and control of adaptive immunity. *Immunol. Rev.* **2009**, *227*, 221–233. [CrossRef] [PubMed]
17. Takeuchi, O.; Akira, S. Pattern Recognition Receptors and Inflammation. *Cell* **2010**, *140*, 805–820. [CrossRef] [PubMed]
18. Velupillai, P.; Sung, C.K.; Andrews, E.; Moran, J.; Beier, D.; Kagan, J.; Benjamin, T. Polymorphisms in Toll-Like Receptor 4 Underlie Susceptibility to Tumor Induction by the Mouse Polyomavirus. *J. Virol.* **2012**, *86*, 11541–11547. [CrossRef] [PubMed]
19. Velupillai, P.; Garcea, R.L.; Benjamin, T.L. Polyoma virus-like particles elicit polarized cytokine responses in APCs from tumor-susceptible and -resistant mice. *J. Immunol.* **2006**, *176*, 1148–1153. [CrossRef]
20. Kondo, T.; Ohshima, T. The dynamics of inflammatory cytokines in the healing process of mouse skin wound: A preliminary study for possible wound age determination. *Int. J. Leg. Med.* **1996**, *108*, 231–236. [CrossRef]
21. Abend, J.R.; Imperiale, M.J. Transforming growth factor-beta-mediated regulation of BK virus gene expression. *Virology* **2008**, *378*, 6–12. [CrossRef] [PubMed]
22. Wollebo, H.S.; Safak, M.; del Valle, L.; Khalili, K.; White, M.K. Role for tumor necrosis factor-α in JC virus reactivation and progressive multifocal leukoencephalopathy. *J. Neuroimmunol.* **2011**, *233*, 46–53. [CrossRef] [PubMed]
23. Rosa, F.D.; Barnaba, V. Persisting viruses and chronic inflammation: Understanding their relation to autoimmunity. *Immunol. Rev.* **1998**, *164*, 17–27. [CrossRef] [PubMed]
24. Yao, M.; Brummer, G.; Acevedo, D.; Cheng, N. Cytokine Regulation of Metastasis and Tumorigenicity. *Adv. Cancer Res.* **2016**, *132*, 265–367. [CrossRef]
25. Multhoff, G.; Molls, M.; Radons, J. Chronic Inflammation in Cancer Development. *Front. Immunol.* **2012**, *2*, 98. [CrossRef]
26. Bromberg, J.; Wang, T.C. Inflammation and Cancer: IL-6 and STAT3 Complete the Link. *Cancer Cell* **2009**, *15*, 79–80. [CrossRef]
27. Jobe, N.P.; Rösel, D.; Dvořánková, B.; Kodet, O.; Lacina, L.; Mateu, R.; Smetana, K.; Brábek, J. Simultaneous blocking of IL-6 and IL-8 is sufficient to fully inhibit CAF-induced human melanoma cell invasiveness. *Histochem. Cell Biol.* **2016**, *146*, 205–217. [CrossRef]
28. Cheteh, E.H.; Sarne, V.; Ceder, S.; Bianchi, J.; Augsten, M.; Rundqvist, H.; Egevad, L.; Östman, A.; Wiman, K.G. Interleukin-6 derived from cancer-associated fibroblasts attenuates the p53 response to doxorubicin in prostate cancer cells. *Cell Death Discov.* **2020**, *6*, 1–14. [CrossRef]
29. Giraudo, E.; Arese, M.; Toniatti, C.; Strasly, M.; Primo, L.; Mantovani, A.; Ciliberto, G.; Bussolini, F. IL-6 is an in vitro and in vivo autocrine growth factor for middle T antigen-transformed endothelial cells. *J. Immunol.* **1996**, *157*, 2618–2623.

30. Bussolino, F.; De Rossi, M.; Sica, A.; Colotta, F.; Wang, J.M.; Bocchietto, E.; Padura, I.M.; Bosia, A.; Dejana, E.; Mantovani, A. Murine endothelioma cell lines transformed by polyoma middle T oncogene as target for and producers of cytokines. *J. Immunol.* **1991**, *147*, 2122–2129.
31. Horníková, L.; Fraiberk, M.; Man, P.; Janovec, V.; Forstová, J. VP1, the major capsid protein of the mouse polyomavirus, binds microtubules, promotes their acetylation and blocks the host cell cycle. *FEBS J.* **2017**, *284*, 301–323. [CrossRef] [PubMed]
32. Liebl, D.; Difato, F.; Horníková, L.; Mannová, P.; Stokrová, J.; Forstová, J. Mouse polyomavirus enters early endosomes, requires their acidic pH for productive infection, and meets transferrin cargo in Rab11-positive endosomes. *J. Virol.* **2006**, *80*, 4610–4622. [CrossRef] [PubMed]
33. Zila, V.; Difato, F.; Klimova, L.; Huerfano, S.; Forstova, J. Involvement of microtubular network and its motors in productive endocytic trafficking of mouse polyomavirus. *PLoS ONE* **2014**, *9*, e96922. [CrossRef] [PubMed]
34. Manders, E.M.; Stap, J.; Brakenhoff, G.J.; van Driel, R.; Aten, J.A. Dynamics of three-dimensional replication patterns during the S-phase, analysed by double labelling of DNA and confocal microscopy. *J. Cell Sci.* **1992**, *103 Pt 3*, 857–862. [CrossRef]
35. Schneider, C.A.; Rasband, W.S.; Eliceiri, K.W. NIH Image to ImageJ: 25 years of image analysis. *Nat. Methods* **2012**, *9*, 671–675. [CrossRef]
36. Bolte, S.; Cordelières, F.P. A guided tour into subcellular colocalization analysis in light microscopy. *J. Microsc.* **2006**, *224*, 213–232. [CrossRef]
37. Lucifora, J.; Bonnin, M.; Aillot, L.; Fusil, F.; Maadadi, S.; Dimier, L.; Michelet, M.; Floriot, O.; Ollivier, A.; Rivoire, M.; et al. Direct antiviral properties of TLR ligands against HBV replication in immune-competent hepatocytes. *Sci. Rep.* **2018**, *8*, 1–11. [CrossRef] [PubMed]
38. Abend, J.R.; Low, J.A.; Imperiale, M.J. Inhibitory Effect of Gamma Interferon on BK Virus Gene Expression and Replication. *J. Virol.* **2007**, *81*, 272–279. [CrossRef]
39. Wilson, J.J.; Lin, E.; Pack, C.D.; Frost, E.L.; Hadley, A.; Swimm, A.I.; Wang, J.; Dong, Y.; Breeden, C.P.; Kalman, D.; et al. Gamma interferon controls mouse polyomavirus infection in vivo. *J. Virol.* **2011**, *85*, 10126–10134. [CrossRef]
40. Yang, Y.; Jiang, B.; Huo, Y.; Primo, L.; Dahl, J.S.; Benjamin, T.L.; Luo, J. Shp2 suppresses PyMT-induced transformation in mouse fibroblasts by inhibiting Stat3 activity. *Virology* **2011**, *409*, 204–210. [CrossRef]
41. Wang, Y.; van Boxel-Dezaire, A.H.H.; Cheon, H.; Yang, J.; Stark, G.R. STAT3 activation in response to IL-6 is prolonged by the binding of IL-6 receptor to EGF receptor. *Proc. Natl. Acad. Sci. USA* **2013**, *110*, 16975–16980. [CrossRef]
42. Im, K.; Baek, J.; Kwon, W.S.; Rha, S.Y.; Hwang, K.W.; Kim, U.; Min, H. The Comparison of Exosome and Exosomal Cytokines between Young and Old Individuals with or without Gastric Cancer. *Int. J. Gerontol.* **2018**, *12*, 233–238. [CrossRef]
43. Gao, K.; Jin, J.; Huang, C.; Li, J.; Luo, H.; Li, L.; Huang, Y.; Jiang, Y. Exosomes Derived From Septic Mouse Serum Modulate Immune Responses via Exosome-Associated Cytokines. *Front. Immunol.* **2019**, *10*, 1560. [CrossRef]
44. Öhlund, D.; Handly-Santana, A.; Biffi, G.; Elyada, E.; Almeida, A.S.; Ponz-Sarvise, M.; Corbo, V.; Oni, T.E.; Hearn, S.A.; Lee, E.J.; et al. Distinct populations of inflammatory fibroblasts and myofibroblasts in pancreatic cancer. *J. Exp. Med.* **2017**, *214*, 579–596. [CrossRef]
45. Sahai, E.; Astsaturov, I.; Cukierman, E.; DeNardo, D.G.; Egeblad, M.; Evans, R.M.; Fearon, D.; Greten, F.R.; Hingorani, S.R.; Hunter, T.; et al. A framework for advancing our understanding of cancer-associated fibroblasts. *Nat. Rev. Cancer* **2020**, *20*, 174–186. [CrossRef] [PubMed]
46. Erez, N.; Truitt, M.; Olson, P.; Hanahan, D. Cancer-Associated Fibroblasts Are Activated in Incipient Neoplasia to Orchestrate Tumor-Promoting Inflammation in an NF-κB-Dependent Manner. *Cancer Cell* **2010**, *17*, 135–147. [CrossRef] [PubMed]
47. Pinto, B.; Henriques, A.C.; Silva, P.M.A.; Bousbaa, H. Three-Dimensional Spheroids as In Vitro Preclinical Models for Cancer Research. *Pharmaceutics* **2020**, *12*, 1186. [CrossRef] [PubMed]
48. Vaure, C.; Liu, Y. A Comparative Review of Toll-Like Receptor 4 Expression and Functionality in Different Animal Species. *Front. Immunol.* **2014**, *5*, 316. [CrossRef]
49. Bouřa, E.; Liebl, D.; Špíšek, R.; Frič, J.; Marek, M.; Štokrová, J.; Holáň, V.; Forstova, J. Polyomavirus EGFP-pseudocapsids: Analysis of model particles for introduction of proteins and peptides into mammalian cells. *FEBS Lett.* **2005**, *579*, 6549–6558. [CrossRef]
50. Husebye, H.; Aune, M.H.; Stenvik, J.; Samstad, E.; Skjeldal, F.; Halaas, Ø.; Nilsen, N.J.; Stenmark, H.; Latz, E.; Lien, E.; et al. The Rab11a GTPase Controls Toll-like Receptor 4-Induced Activation of Interferon Regulatory Factor-3 on Phagosomes. *Immunity* **2010**, *33*, 583–596. [CrossRef]
51. Szatmári, Z.; Kis, V.; Lippai, M.; Hegedűs, K.; Faragó, T.; Lőrincz, P.; Tanaka, T.; Juhász, G.; Sass, M. Rab11 facilitates cross-talk between autophagy and endosomal pathway through regulation of Hook localization. *Mol. Biol Cell* **2014**, *25*, 522–531. [CrossRef] [PubMed]
52. Yavuz, B.G.; Gunaydin, G.; Gedik, M.E.; Kosemehmetoglu, K.; Karakoc, D.; Ozgur, F.; Guc, D. Cancer associated fibroblasts sculpt tumour microenvironment by recruiting monocytes and inducing immunosuppressive PD-1 + TAMs. *Sci. Rep.* **2019**, *9*, 1–15. [CrossRef]
53. Aldinucci, D.; Colombatti, A. The inflammatory chemokine CCL5 and cancer progression. *Mediat. Inflamm* **2014**, *2014*, 292376. [CrossRef] [PubMed]
54. Ren, C.; Cheng, X.; Lu, B.; Yang, G. Activation of interleukin-6/signal transducer and activator of transcription 3 by human papillomavirus early proteins 6 induces fibroblast senescence to promote cervical tumourigenesis through autocrine and paracrine pathways in tumour microenvironment. *Eur. J. Cancer* **2013**, *49*, 3889–3899. [CrossRef] [PubMed]

55. Morgan, E.L.; Macdonald, A. Autocrine STAT3 activation in HPV positive cervical cancer through a virus-driven Rac1—NFκB—IL-6 signalling axis. *PLoS Pathog.* **2019**, *15*, e1007835. [CrossRef]
56. Taraboletti, G.; Belotti, D.; Dejana, E.; Mantovani, A.; Giavazzi, R. Endothelial cell migration and invasiveness are induced by a soluble factor produced by murine endothelioma cells transformed by polyoma virus middle T oncogene. *Cancer Res.* **1993**, *53*, 3812–3816.
57. Yang, H.; Wang, B.; Wang, T.; Xu, L.; He, C.; Wen, H.; Yan, J.; Su, H.; Zhu, X. Toll-like receptor 4 prompts human breast cancer cells invasiveness via lipopolysaccharide stimulation and is overexpressed in patients with lymph node metastasis. *PLoS ONE* **2014**, *9*, e109980. [CrossRef]
58. Ou, T.; Lilly, M.; Jiang, W. The Pathologic Role of Toll-Like Receptor 4 in Prostate Cancer. *Front. Immunol.* **2018**, *9*, 1188. [CrossRef]

Appendix II: another publications of author